A SYSTEM LEVEL MODELING AND PERFORMANCE EVALUATION OF CONCENTRATED SOLAR POWER PLANT

A THESIS SUBMITTED TO
THE BOARD OF CAMPUS GRADUATE PROGRAMS
OF MIDDLE EAST TECHNICAL UNIVERSITY
NORTHERN CYPRUS CAMPUS

BY

SYED ZAID HASANY

IN PARTIAL FULLFILLMENT OF THE REQUIREMENTS
FOR
THE DEGREE OF MASTER OF SCIENCE
IN
SUSTAINABLE ENVIRONMENT AND ENERGY SYSTEMS

DECEMBER 2013

Approval of the Board of Graduate Programs

_____
Prof. Dr. Erol Taymaz
Chairperson

I certify that this thesis satisfies all the requirements as a thesis for the degree of Master of Science.

_____
Asst. Prof. Dr. Ali Muhtaroğlu
Program Coordinator

This is to certify that we have read this thesis and that in our opinion it is fully adequate, in scope and quality, as a thesis for the degree of Master of Science.

_____
Asst. Prof. Dr. Eray Uzgören
Supervisor

Examining Committee Members

Assoc. Prof. Dr. Derek Baker (Committee chair)	Mechanical Engineering Dept. METU NCC	_____
Asst. Prof. Dr. Eray Uzgören	Mechanical Engineering Dept. METU NCC	_____
Asst. Prof. Dr. Ali Muhtaroğlu	Electrical and Electronic Engineering Dept. METU NCC	_____

I hereby declare that all information in this document has been obtained and presented in accordance with academic rules and ethical conduct. I also declare that, as required by these rules and conduct, I have fully cited and referenced all material and results that are not original to this work.

Name, Last name : Syed Zaid, Hasany

Signature :

ABSTRACT

A SYSTEM LEVEL MODELING AND PERFORMANCE EVALUATION OF CONCENTRATED SOLAR POWER PLANT

Hasany, Syed Zaid

M.S., Sustainable Environment and Energy Systems Program

Supervisor: Asst. Prof. Dr. Eray Uzgören

December 2013, 104 Pages

This thesis presents a system level study for a solar thermal power plant comprising of parabolic trough collectors (PTC), an organic Rankine cycle (ORC) and a wet cooling tower. A transient numerical model is developed for the PTC accounting the thermal losses and coping up with the intermittent and inherent variable solar input. The transient PTC model is validated with the experimental and numerical results and extended to the double pass counter flow PTC configuration. It is found that there is no significant difference in efficiency for different cases for double pass and single pass but double pass manages to heat the water at high temperature due to premixing under constant conditions of inlet temperature. The numerical model of single pass PTC is integrated with the modified numerical model of ORC in which evaporator/condenser are modeled with transients effects while pump/expander are modeled with acceptable steady state assumptions, and cooling tower. Several different conditions are simulated on the verified ORC model with a range of constant hot water temperatures to the ORC and refrigerant mass flow rates. The power output has a direct relation with the hot water temperature and refrigerant mass flow rate. A full day simulation taking into account the temporal solar and ambient variations for the course of the day during the sun light hours is carried out. Three representative days of the year are selected for the simulations and found out that average power output is 14.5 kW, 14.88 kW and 15.16 kW for summer solstice, fall equinox and winter solstice respectively.

Keywords: Parabolic Trough Collectors, ORC, system integration, transient modeling

ÖZ

A SYSTEM LEVEL MODELING AND PERFORMANCE EVALUATION OF CONCENTRATED SOLAR POWER PLANT

Hasany, Syed Zaid

Yüksek Lisans, Sürdürülebilir Çevre ve Enerji Sistemleri Programı

Tez Yöneticisi: Yrd. Doç. Dr. Eray Uzgören

Aralık 2013, 104 sayfa

Bu tez, ısı girişi için parabolik kollektörler (PTC) ve ısı atımı için ıslak soğutma kulesi kullanan organik Rankin çevrimi (ORC) içeren bütünleşik bir sistemi incelemektedir.. Kollektörlerden elde edilen ısı enerjisi hesaplanırken güneş ışınımlarının değişimi ve hava sıcaklığına bağlı ısı kayıpları düşünülerek zamana bağlı bir sayısal yöntem geliştirilmiştir. Bu yöntem, literatürde bulunan deneysel ve sayısal sonuçlar ile doğrulanmış; ve çift geçişli ters akış parabolik kollektörlerin verimini incelemek için kullanılmıştır. Çift geçişli parabolik kollektör veriminin geleneksel tek geçişli kollektörlere göre önemli bir fark göstermediği bulunmasına karşın, giriş sıcaklıkları aynı olduğu koşullarda önkarışma sayesinde çift geçişin daha yüksek sıcaklıkta su çıkışı verebildiği bulunmuştur. Tek geçişli kollektör için geliştirilen sayısal yöntem varolan bir ORC sayısal yöntemi ile birleştirilmiştir. ORC yöntemi; evaporatör ve kondenser için zamana bağlı olarak düşünülmüş ancak tepki zamanı çok hızlı olan pompa/genişletici için kararlı durum varsayımları kullanılmıştır. Aynı zamanda kondenser için ortam sıcaklığının hızlı değişmeyeceği düşünülerek soğutma kulesi de kararlı durum üzerinden basitleştirilmiş bir yöntem kullanılarak hesaplamalara dahil edilmiştir. Geliştirilen yöntem değişen dış koşullara bağlı olarak simüle edilmiş; ORC güç çıkışının evaporatöre giren suyun sıcaklığı ve kütle akışı ile doğru orantılı olduğu beklendiği üzere gözlemlenmiştir. Zamansal güneş konumu ve ortam değişiklikleri göz önünde bulundurarak bir tam gün simülasyonları güneş ışığı saatleri dikkate alınarak gerçekleştirilmiştir. Yılın üç temsili günleri (yaz gündönümü, ekinoks ve kış gündönümü) için ortalama güç çıkışları sırasıyla 14.5 kW , 14.88 kW ve 15.16 kW olarak bulunmuştur .

DEDICATION

A humble dedication to

"THE MOST PRAISED ONE" (S.A.W)

ACKNOWLEDGEMENTS

I begin with the glorified name of ALLAH Almighty by praising and thanking him for whatever He has bestowed upon me so far in my life. I would thank Him for the opportunity He had given me and the courage, patience and determination to accomplish that.

"Be grateful to Allah. And whoever is grateful is grateful for [the benefit of] himself. And whoever denies [His favor] - then indeed, Allah is Free of need and Praiseworthy"

(Al-Quran)

I would like to express my deepest gratitude to my adviser Dr. Eray Uzgören for his continuous support, advice and guidance throughout my work. I would also like to thank him for supporting me through the difficult phases of my master's degree. I would also like to thank him for tolerating the delays from my side during the course of this work.

I would like to express my sincere gratitude to my friends and colleagues who helped me in my work. I like to thank Musbaudeen Bamgbopa for his distant help in understanding a lot of things regarding his work. I would also like to thank Abdullah Mohiuddin and Eray Timur for their fruitful inputs and discussions regarding the research. Beside the technical help and support, I am really grateful to Muhammad Azhar Ali Khan, Arsalan Tariq, Jibran Shahzad, Abdullah Mohiuddin, Eray Timur and many others who helped me in having a good time on the campus.

I would also like to thanks METU-NCC and Mechanical engineering department for providing me with an assistantship which helped me immensely in funding my masters and stay in Cyprus. I would also like to express my kindest regards to all the faculty members of Mechanical engineering department for their kind support.

At last but definitely not the least, I would like to express my love, affection and kindest regards to my mother in particular and relatives in general for their continuous prayers and support.

Syed Zaid Hasany

TABLE OF CONTENTS

ETHICAL DECLARATION ii
ABSTRACT iv
ÖZ v
DEDICATION vi
ACKNOWLEDGEMENTS vii
LIST OF TABLES x
LIST OF FIGURES xi
NOMENCLATURE xiv
CHAPTER
1. INTRODUCTION 1
1.1. Solar Resource Assessment and Parabolic Trough Collectors 5
1.2. Organic Rankine Cycle 7
1.3. Scope and Objective 8
1.4. Thesis Overview 9
2. THERMAL MODELING OF PARABOLIC TROUGH COLLECTOR 10
2.1. Problem description of parabolic trough collector 11
2.2. Solar Resource Model 16
2.3. Fluid flow analysis 17
2.4. Receiver wall analysis 19
2.5. Glass cover wall analysis 22
2.6. Validation of the Parabolic Trough Collector Model (Single pass) 24
2.7. Parabolic Trough Collector Model Double Pass 30
2.7.1. Numerical modeling 31
2.7.2. Numerical Simulations and Results of Double Pass PTC 33
3. SYSTEM LEVEL MODELLING 37
3.1. Organic Rankine Cycle Model 37
3.1.1. Evaporator 38
3.1.2. Condenser 41
3.1.3. Numerical Algorithm for Evaporator and Condenser 45
3.1.4. Pump 49
3.1.5. Expander 50
3.2. Cooling Tower Model 51

3.3. System Integration 52
4. RESULTS AND DISCUSSION 54
4.1. ORC analysis 54
4.2. PTC, ORC and cooling tower 60
4.2.1. Solar resources and area of the PTC 60
4.2.2. Pressure drop 62
4.2.3. PTC, ORC and cooling tower system analysis 63
5. CONCLUSION 72
REFERENCES 75
APPENDICES 78

LIST OF TABLES

Table 1: Comparison of different solar thermal technologies[10],[11]. 3

Table 2 Correction factor for Climatic types 17

Table 3: Summary of the coefficients for receiver temperature profile. 21

Table 4: Summary of the coefficients for glass cover temperature profile. 24

Table 5: Single Pass Parabolic Trough Collector specifications for model validation. 25

Table 6: Summary of the validation cases for Single Pass Parabolic Trough Collector Model with O. Garcia-Valladares et al and Experimental. 29

Table 7: Geometrical, optical and material specifications of double pass PTC. 34

Table 8: Mass flow rates for double pass PTC. 34

Table 9: Summary of the coefficients for glass cover temperature profile. 41

Table 10: Summary of the coefficients for evaporator pipe temperature profile 41

Table 11: Summary of the coefficients for condenser pipe temperature profile 43

Table 12: Summary of the design parameters for steady state analysis [39]. 46

Table 13: Steady state analysis for evaporator/condenser models. 46

Table 14: Regression constants for pump. 50

Table 15: Design parameters for ORC [40]. 54

Table 16: Areas and mass flow rates for design conditions. 55

Table 17: Net power output of ORC at various refrigerant mass flow rates and hot water inlet temperatures. 58

Table 18: PTC design parameters. 61

LIST OF FIGURES

Figure 1: Global Energy mix by resources[1] 1

Figure 2: Projection of Emissions for developed and developing Countries [3]..... 2

Figure 3: Schematic of the solar thermal electric system..... 5

Figure 4: (Left) Schematic of PTC rows. (Right) End view of the PTC representing the reflection towards the focus.[32]..... 10

Figure 5: Schematic of PTC showing width, length and receiver's diameter..... 12

Figure 6: Front and side view of single pass PTC, showing modes of heat transfer and numerical nodes..... 13

Figure 7: Flow Chart of the PTC numerical algorithm 15

Figure 8. Control volume for the fluid flow inside the receiver tube..... 17

Figure 9. Computational scheme for the receiver tube..... 20

Figure 10. Computational scheme for the glass cover. 22

Figure 11: Error (Outlet Temperature at steady state) vs. number of nodes. 27

Figure 12: Error (Average energy gain at steady state) vs. number of nodes. 27

Figure 13: Temperature profiles at different locations in the computational domain for case 1..... 28

Figure 14: Trend of thermal efficiency with the inlet working fluid temperatures. 30

Figure 15: Schematic for the double pass PTC (Counter flow heat exchanger). 31

Figure 16: Front and side view of single pass PTC, showing modes of heat transfer and numerical nodes..... 32

Figure 17: Average receiver temperatures at steady state at different mass flow rates..... 35

Figure 18: Efficiency of the double/single pass PTC at different mass flow rates. 35

Figure 19: Outlet temperatures of double pass (Internal tube and annulus) and single pass at different mas flow rates at steady state condition. 36

Figure 20: Useful rate of energy absorbed for double/single pass PTC at different mass flow rates 36

Figure 21: Schematic of the Organic Rankine Cycle (ORC). 37

Figure 22: Numerical domain for evaporator and condenser 44

Figure 23: (Right) Condenser design conditions (Temperature), (Left) Evaporator design conditions (Temperature). 47

Figure 24: Transients of refrigerant temperature and enthalpies at the exit nodes (Evaporator (E)/Condenser(C)) 48

Figure 25: Transients of hot/cold water temperatures at the exit nodes 48

Figure 26: Graphical summary of the results at steady state (Evaporator (E)/Condenser(C)) 49

Figure 27: Black box representation of the pump. 50

Figure 28: Black box representation of the expander. 51

Figure 29: Black box representation of the wet cooling tower. 51

Figure 30: Schematic of integrated sub-systems (PTC, ORC and cooling tower) 52

Figure 31: Transients of temperature of water at the outlet of evaporator and condenser. 56

Figure 32: Temperature-entropy diagram of the ORC for the design case simulation at steady state. 56

Figure 33: Trend of rate of thermal energy to the ORC with the hot water inlet temperatures and refrigerant mass flow rates. 57

Figure 34: Trend of net power output from ORC with the hot water inlet temperatures and refrigerant mass flow rates. 58

Figure 35: Variation of condenser pressure with hot water inlet temperatures and refrigerant mass flow rates. 59

Figure 36: Variation of evaporator pressure with hot water inlet temperatures and refrigerant mass flow rates. 59

Figure 37: Daily solar irradiance for representative days of a year. 60

Figure 38: (Left) PTC single pass parallel configuration (Right) PTC single pass series configuration 62

Figure 39: Pressure drop in single pass PTC at different mass flow rates. 63

Figure 40: Ambient temperature profile at each hour of representative days of the year. 64

Figure 41: Temperature profile at the outlet of PTC, evaporator, condenser and cooling tower for summer solstice. 65

Figure 42: Temperature profile at the outlet of PTC, evaporator, condenser and cooling tower for equinox (Sep)..... 66

Figure 43: Temperature profile at the outlet of PTC, evaporator, condenser and cooling tower for winter solstice. 66

Figure 44: Pressure and saturation temperature variation at condenser for summer solstice. 67

Figure 45: Pressure and saturation temperature variation at evaporator for summer solstice. 67

Figure 46: Available solar power and useful power to the PTC for summer solstice. 68

Figure 47: Available solar power and useful power to the PTC for equinox (Sep). 69

Figure 48: Available solar power and useful power to the PTC for winter solstice..... 69

Figure 49: Net power output through the course of representative days. 70

Figure 50: ORC efficiency through the course of representative days..... 70

NOMENCLATURE

α	Absorptance of the glass cover in Parabolic Trough Collector (PTC)
γ	Shape factor in PTC
ρ_o	Reflectivity of the PTC
ρ	Density of the material (water, refrigerant and pipe/tube) (kg/m^3)
τ	Transmittance of the glass cover in PTC
μ	Viscosity (Pa sec)
A	Area (m^2)
Cp	Specific heat (J/kg K)
D	Diameter (m)
M	Fraction of mass flow rate in double pass PTC
T	Temperature
W	Width of Parabolic Trough Collector (m)
dx	Length of the control volume (m)
h	Enthalpy of the fluids (water and refrigerant) (kJ/kg)
k	Thermal conductivity (W/mK)
$\dot{m}$	Mass flow rate (kg/sec)
q_u	Useful energy gain (W/m^2)
Δt	Time interval (sec)

Subscripts

a	Ambient air
AM	Angle modifier in PTC
SR	Solar radiation
b	Beam radiation (Solar)
r	Receiver of PTC
c	Glass cover of PTC (Chapter 2)
t	Internal tube of the double pass PTC
fl (*f*)	Fluid in PTC (water/oil)
ann	Annulus flow
con,rc	Convective heat transfer coefficient between receiver and glass cover
rad,rc	Radiative heat transfer coefficient between receiver and glass cover
con,camb	Convective heat transfer coefficient between glass cover and ambient environment

rad,camb	Radiative heat transfer coefficient between glass cover and ambient environment
ci	Inside of glass cover
co	Outside of glass cover
ri	Inside of receiver
ro	Outside of receiver
ti	Inside of internal tube in double pass PTC
to	Outside of internal tube in double pass PTC
i, *i*-1 and *i*+1	computational nodes of control volumes
$i \mp 1/2$	face representation of control volumes
ref	refrigerant
e	Evaporator
c	Condenser (Chapter 3)
hw	Hot water in evaporator
cw	Cold water in evaporator
p	Evaporator/condenser tube/pipe
liq(*l*)	Liquid phase, in the calculation of heat transfer coefficient
vap(*v*)	Vapor phase, in the calculation of heat transfer coefficient
db	Dry bulb
wb	Wet bulb
Superscripts	
t and t+1	Old and new time step respectively

Chapter 1

INTRODUCTION

Energy is one of the most vital inputs for the development of a society and in this growing world its demand has escalated to an alarming level which is primarily met by the conventional fossil fuels. Figure 1 summarizes the study conducted by International Energy Agency (IEA) in 2008 highlighting 33.5% of the total power production was from oil followed by coal 26.8%, gas 20.8%, nuclear 5.8% and 12.9% from renewable energy resources (combined hydro, wind, solar, bio-mass and geo-thermal). Only oil and coal provide 60% of the total energy supply[1].

Due to the rapid economic growth, consumption of fossil fuels with the ongoing trend is devastating. The combustion of fossil fuels is the main contributor of the global pollution. Emissions in the form of CO_2, sulphur, NO_x and ozone are disturbing the natural balance of ecology and causing grave global environmental issues in the form of ozone depletion, air-water contamination, sea level rise and loss of bio diversity in many habitats around the globe. In addition to the environmental problems, it raises political and socio-economic issues. According to United States Energy Information Administration (EIA), the oil consumption of the World will increase to 98.3 mbd (millions barrels per day) in 2015 and 118 mbd in 2030 from 84.4 mbd in 2009. If this predicted trend goes on, the global energy-economic-environment nexus will become more complex and challenging to address[2].

Uncontrolled and unregulated consumption of fossil fuels in the developing World is a

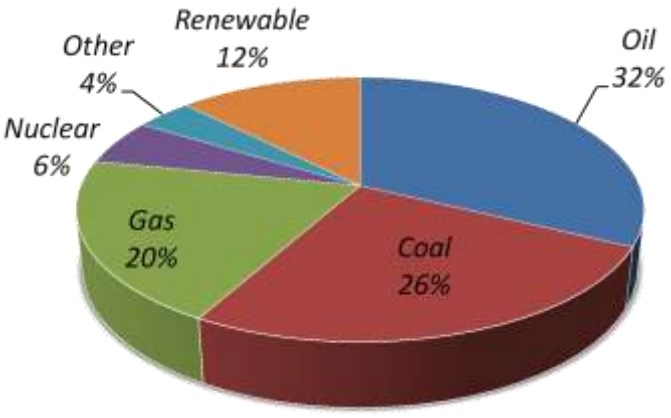

Figure 1: Global Energy mix by resources[1]

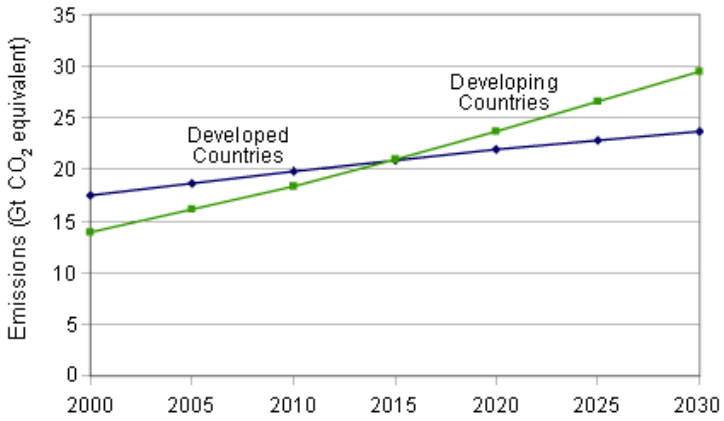

Figure 2: Projection of Emissions for developed and developing Countries [3]
1 Gt = 10^9 metric tons = 1 billion metric tons = 1 petagram (Pg)

serious threat to the environmental degradation. As given in Figure 2, greenhouse gas emissions are likely to rise in the developing World due to the ongoing economic and population growth.

In order to address the aforementioned problems, renewable energy resources have gained tremendous attention globally. Examples of renewable energy utilization include direct conversion of solar radiation, wind currents due to the variations of temperatures, bio-mass resulting in biological changes in the form of photosynthesis, gravitational forces through tidal waves and heat of earth's core (geo-thermal energy). Renewable energy has massive potential to meet the global energy demands but acceptability of these sources as primary energy sources varies due to technical and economic constraints, which are addressable. Currently, various researchers focus on enhancing the energy conversion efficiency, economic viability and adoptability all over the world. Renewable energy resources can help reduce the pollution, eliminate the dependency of the high cost fuels and provide socio-economic development in the remote and off-the-grid areas. It is estimated that the global energy demand would rise roughly to 800-1000 EJ (2.22-2.77 $\times 10^{11}$ MWh) in 2050 [4]. To meet this demand, energy mix should be revised taking into consideration the massive global renewable energy potential. Currently, total energy coming from renewable sources consists of 10% traditional bio-mass for heating, 3% hydro-electricity while solar, wind, geo-thermal etc contribute to a total of only 3%. [5]. According to Johanson TB et al, adaptation of an intensive and comprehensive renewable energy policy on a global scale would elevate the renewable energy contribution to 318 EJ until 2050 [6].

Among renewable energy resources, energy from direct solar radiation has the largest potential available on the planet. Approximately 3,850,000 EJ per annum of solar energy is absorbed by the Earth's atmosphere, oceans and land masses [7]. After deducting all losses

in the form of absorption, reflection, and others, the potential for the convertible solar energy is 1600 EJ per annum which is still very promising [8].

Major solar energy related applications utilize two leading technologies namely (1) photo-voltaic cells (PV) and (2) collectors to capture solar thermal energy linked to a power cycle. For large scale power plants, solar thermal power systems are advantageous over the PV technology by having higher conversion efficiencies, low investment cost, inherent thermal storage to work during the off hours. They can also be coupled with other systems for desalination or refrigeration [9].

Table 1: Comparison of different solar thermal technologies[10],[11].

Types of technology	Temperature Range	Advantages	Disadvantages
Flat plate Collector	Relatively low temperature. ~50°C-~100°C	• Utilizes direct and diffuse solar radiations.	• Low output temperatures. • Large surface area more thermal losses. • Low thermal efficiency. • More material for manufacturing.
Parabolic trough collector (PTC)	~100°C-~300°C (depending upon the HTF)	• High temperatures can be achieved. • High thermal efficiency.	• Low output temperatures compared to other concentrating technologies.
Fresnel collector	> 250°C	• Easy to manufacture compared to PTC. • Low cost.	• Low optical efficiency compared to PTC. • Thermal storage integration challenges.
Solar tower	250°C-300°C (water) < 350°C (oil) < 500°C (molten salt) <750°C (gases)	• Direst steam generation (DSG) can be achieved. • Highly efficient. • Large power plants (Capacity<10 MW).	• Commercial experience is needed for its adaptation.
Dish collector	Around 750°C	• Highest conversion efficiency (25-30%) • Cooling water is not required.	• Very expensive. • Still in the demonstration phase.

One promising technology in solar thermal systems is concentrated solar power (CSP) systems. The fundamental principle is the concentration of solar radiation to a point (or line) to heat the working fluid which can then be used as heat source in conventional power systems. There are different methods to concentrate the solar radiations depending upon the applications and desired temperatures. Parabolic trough collectors (PTC) offer advantages over flat plate solar collector as flat plate collectors require large surface area arising concerns for high thermal losses.

PTC also shows least development risk as compared to other concentrating technologies like Fresnel collector, solar tower and dish sterling. PTCs consist of linear parabolic mirrors which reflect the solar rays to a tube placed along the focal line of the collectors, where fluid absorbs the solar energy and gets heated to be used as a heat source for the energy conversion to electrical energy. To compensate the sun's movement, collectors can optionally track the sun using 1-axis or 2-axis movements throughout the day or season. Other technologies offering various ranges of output temperatures are compared in Table 1, for conversion efficiency and cost.

In the solar thermal power system, one of the most important components is the conversion of the renewable energy to useful mechanical and electrical energy. Conventional Rankine cycle may not be suitable for applications with low temperatures provided by PTCs (100-250 °C) while Organic Rankine Cycle (ORC) emerges as a viable and efficient alternative. The most attractive feature of ORC is its capability to convert low grade/temperature energy to useful energy. Low grade energy resources include many renewable resources such as solar, bio and geothermal as well as from low enthalpy waste heat. The working principle of the ORC is the same as the conventional Rankine cycle with different working fluids. The boiling point of the selected fluid in ORCs is typically less than that of water thus low temperature sources can be utilized.

Figure 3 shows a schematic of solar thermal power plant with different components running on ORC. The refrigerant is pumped into the evaporator where heat is absorbed by the solar thermal system. Vapor is then expanded by an expander for the power generation followed by condensation.

Solar thermal power systems have multiple subsystems including solar resource assessment, efficiency analysis of the parabolic trough collectors, unsteady organic Rankine cycle, and cooling loop of the global power cycle. In the solar thermal power systems, all the above mentioned subsystems are coupled and directly affect the performance of each other. A

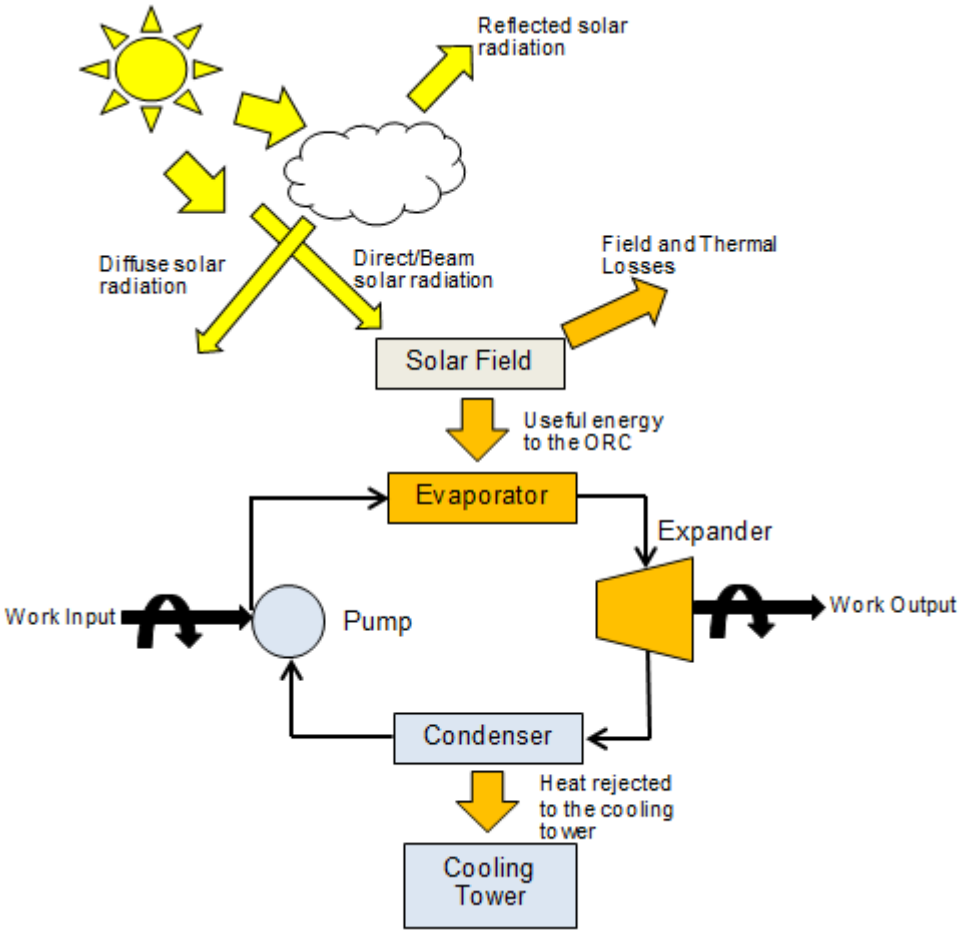

Figure 3: Schematic of the solar thermal electric system

global system level study is needed for a global perspective of the solar electric generation system incorporating all the sub systems. Such a study would be helpful in determining the critical parameters which affect the overall performance and efficiency of the solar electric generation system. Moreover, different configurations and arrangements of parabolic trough collectors can be studied to identify the system's overall performance.

1.1. Solar Resource Assessment and Parabolic Trough Collectors

Detailed solar resource information for a particular location is an important input in designing the solar thermal systems. Most of the weather stations provide global solar data (total of diffuse and beam) on horizontal surfaces. Concentrated solar systems rely on beam irradiation. Several models have been developed for the solar resource assessment for a given location, whose detailed meteorological data decamped into beam and diffuse may not be available. Ibrahim et al. [12] estimated the solar resources, beam and diffused on inclined surfaces. The calculated values were compared with the measured ones and found in good

agreement. Similar kind of study is done by Naing et al., they proposed a mathematical model for the solar resource quantification in Singapore, and the computed and measured data were 90% in agreement [13].

Detailed modeling of parabolic trough collectors (PTC) comprising of convective, radiative and other effects enables to quantify the useful heat transfer to the working fluid. Due to the varying nature of solar energy input to the parabolic trough collectors, these models help to analyze the parameters which significantly alter the performance of the system. Qu et al. [14] modeled parabolic collector with solar tracking capabilities using fundamental convective and radiative heat transfer concepts for steady state conditions. Saad et al. [15] modeled the parabolic trough collectors to analyze the thermal performance of the collectors, efficiency of installed (oil in the tubes) and the proposed systems (direct steam generation in the tube for power production) are compared with the help of developed model based on the absorber wall temperature, with different tube diameters. They also developed an unsteady model to simulate the performance of process heating system using parabolic trough collectors [16]. Optimal size of the collectors and storage tank are recommended to tackle the challenges due to transient solar energy input to the system.

Several studies have been carried out for the extension and improvement of the solar electric generation systems (SEGS). A study on SEGS was carried out by Azizian et al. of 250 kW pilot solar power plant to extend it to 500 kW [17]. They expanded the installed system with large collectors, auxiliary superheater and additional heat exchangers. Detailed thermal and structural design was carried out to analyze the benefits and shortcomings of both the systems. Robert. W. B [18] performed an optimization study for the performance enhancement of PTCs by introducing low cost air filled receivers in low temperature regions and evacuated tubes in the high temperature regions of the solar loops. Even though evacuated tubes give better thermal performance by reducing the thermal convective losses, they require high initial and maintenance cost due to manufacturing and mechanical challenges.

O. Garcia-V et al. [19] performed an unsteady numerical study for the thermal, optical and fluidic behavior of the PTCs solving the governing equation for single pass collectors. The results were validated with the experimental data obtained from Sandia National Laboratory with air and vacuum inside the collector tubes. Their numerical model was extended to simulate PTC with counter flow concentric circular heat exchangers (double pass). In double pass configuration the heat transfer fluid is pre-mixed with the heated fluid from the

annulus or the internal tube. They concluded that the thermal efficiency compared to the single pass increased.

1.2. Organic Rankine Cycle

Organic Rankine Cycle (ORC) has been adapted as the premier technology to convert low temperature energy sources (solar, geo-thermal etc.) to useful mechanical and electrical power. Extensive research is being carried on this subject focusing on various energy resources and final mechanical and electrical outputs. For a technology status review, readers can refer to articles of Velez et al. [20] and Tchanche et al. [21]

Dai et al. [22] performed a parametric optimization study for waste heat recovery application. Similar study was also carried out by Saleh et al. [23], who studied the thermodynamic performance of 31 different fluids for ORC. Solar energy, being intermittent in nature, poses similar challenges to the ORC system analysis. Auxiliary boilers are used to overcome this problem of intermittency [17]. Bamgbopa et al. [24] analyzed the performance of an ORC system with R245fa as the working fluid with solar energy as the heating source to the water. Component level modeling is performed in order to identify the critical parameters in the cycle. Mass flow rates of refrigerant/hot water and hot water inlet temperature were identified as the critical parameters for the optimized performance. Different scenarios of fluctuating heat transfer inputs are studied with the application of control measures. Wei et al. [25] also performed dynamic modeling of ORC for controlling and monitoring under transient conditions. Two different approaches, moving boundary and discretization technique, were adopted to correctly represent the dynamics of evaporator and condenser.

Several system level and hybrid studies were also carried out. Guo et al. [26] proposed a novel cogeneration ORC system consisting of low temperature geo-thermal source powering ORC, an intermediate heat exchanger and a heat pump sub-system. The screening criteria included net power output per unit mass flow rate of heat source, total heat transfer area to power output and electricity cost. Lior et al. [27] analyzed a hybrid solar power/cooling system (ORC and chiller), with an auxiliary boiler to super heat the nominally (100 °C) heated water. A transient sensitivity analysis was carried out to find the optimum energy performance configuration. Kane et al. [28] integrated the solar collectors, ORC with a diesel engine. The exhaust and the block cooling of the diesel engines were also used as the heat input to the ORC during cloudy and night times. It was confirmed from the preliminary

site experimentations that solar power plant coupled with the diesel engine substantiates the proposed integration concept.

Patnode [29] modeled the Solar Electric Generation System (SEGS) in southern California which comprises of the Parabolic Trough Collectors and steam Rankine cycle for power production (approx. 354 MW peak power). TRNSYS simulation software was used for the solar field modeling while Rankine cycle was modeled separately with steady state assumptions. The model was experimentally validated using on ground data for flow rates and temperatures. Thermal losses in the collector, due to the temporal degradation (solar field), were modeled with simplification of 50% of the total solar field degradation. Due to the significant consumption of the water in the cooling tower (the installed system), air cooled condenser (dry cooling) was modeled, evaluated and compared with the installed cooling tower. Wang et al. [30] studied the thermodynamic behavior and the optimization of a solar driven ORC. A steady state model was developed for the flat plate solar collectors and ORC. A parametric study was carried out to investigate the performance by changing working fluids.

1.3. Scope and Objective

It is observed from the literature review that a significant amount of research has been done on the solar energy systems in general, on the solar resource assessment, on PTC modeling and performance enhancement, on ORC optimizations. However, the main deficiency of the literature is the system integration studies of parabolic trough collectors, ORC and the cooling system all together. Most of the studies related to solar power systems are standalone and do not integrate subcomponents of the system, i.e. solar resource, PTC, ORC and cooling. The limited amount of system level studies , i.e.[26] and [27], considered an integrated system with the ORC for cogeneration using heat pump and chiller respectively. On the other hand, [28] used small flat reflecting plates as concentrator to provide heat to the ORC for preliminary level experimentations. Patnode [29] studied the solar power system in detail including all sub systems, using TRNSYS software with steady state assumptions. Wang et al [30] modeled flat plate collectors and ORC with steady state assumptions ignoring the dynamic behavior of the heat input.

This thesis is an extension of the ORC study by Bamgbopa et al. [24], which focuses only on the ORC modeling and investigation of the performance at varying conditions. This study focuses on the development of a transient numerical model for solar field parabolic trough collectors. Moreover, the transient numerical model for PTC is coupled with the

adapted model of Bamgbopa et al. [24] along with the steady state model of wet cooling tower. The contribution of this study can be summarized as follows:

- Develop a transient model for solar panels to quantify available and useful thermal source for an ORC based power plant.
- Compare double pass and single pass low temperature PTCs for their performance.
- Develop a full model at system level which includes transient collector model, transient Organic Rankine Cycle model and the steady state cooling tower model to enable optimization studies at system level. Such a model would also help identifying the best control strategy as the solar energy input is subjected to weather variations during the day time.

1.4. Thesis Overview

This thesis includes 5 chapters. Chapter 1 presented a general background discussing current global energy scenario and the motivation of consuming renewable energy in general and solar energy in particular which is followed by a brief discussion of concentrating solar thermal electric generation systems. It also presents a detailed literature review on solar energy technology in general, with the emphasis on reviewing concentrating solar thermal research. It covers a wide range of literature encompassing the solar resource assessment studies, parabolic trough collectors, performance enhancement opportunities, Organic Rankine Cycle and their systems level studies. Furthermore, also highlights the scope and objective of the current research. Chapter 2 deals with the detailed numerical modeling of solar resources and parabolic trough collectors with different configurations. Moreover the validation of the developed model is also presented in this chapter. Chapter 3 presents the numerical modeling of different components of the ORC (pump, evaporator, turbine and condenser), description of the cooling tower model and integration of the ORC and cooling tower with the parabolic trough collectors. Chapter 4 discusses the results and findings of the analysis based on the models developed in chapter 2 and 3 in detail, followed by the concluding chapter 5 which summarizes the results, key findings and future work.

Chapter 2

THERMAL MODELING OF PARABOLIC TROUGH COLLECTOR

Parabolic trough collectors (PTCs) are one of the most common types of concentrated solar collectors used for power production in solar electric (power) generation systems. Several solar thermal power plants are operating around the globe with a total capacity of approximately 2500 MW, with "SEGS" (Solar Electric Generation System), California leading with 354 MW and Spain being the world leader with a total production of approximately 1900 MW [31]. PTCs comprise of a parabolic shiny surface to reflect solar beams on a single pipe, known as receiver. Receiver carries heat transfer fluid and is usually wrapped with a glass enclosure to minimize heat losses to the surroundings. Heat transfer fluid is usually water or oil for their heat capacity as well as their economical availability. Figure 4 shows the schematic of the PTC with receiver and reflectors; and reflection of the solar beam to the focus (receiver).

In general, useful energy absorbed by the heat transfer fluid characterizes collectors' efficiency, which strongly depends on ambient conditions and the system temperatures. Performance of PTCs is highly dependent on many physical, geometrical and temporal

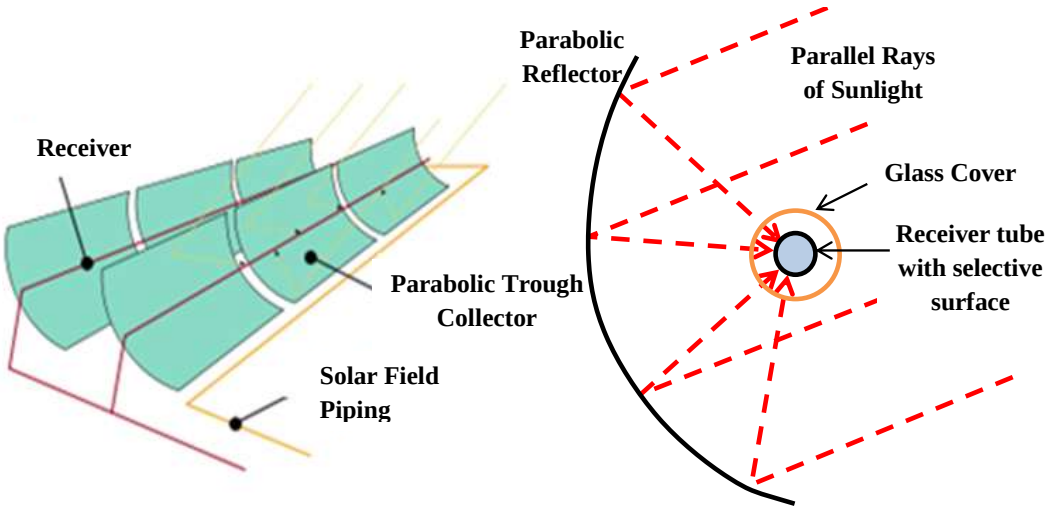

Figure 4: (Left) Schematic of PTC rows. (Right) End view of the PTC representing the reflection towards the focus.[32]

factors. This is mainly because PTC systems utilize the beam component of the global radiation.

In PTCs, the modes of heat transfer in radial direction are primarily convection between all relevant layers (i.e. heat transfer fluid, receiver tube, the glass cover, and the environment). Radiation between the glass cover and the receiver tube can be significant as a result of the temperature difference. In axial direction, conductive heat transfer through the receiver tube can influence the system's thermal inertia contributing to the thermal performance of the system.

This chapter discusses the methodology of the solar resource estimation and transient numerical modeling for the optical, thermal and fluidic behavior of the parabolic trough collectors for single and double pass configurations. Relevant assumptions, modes of heat transfer, and heat transfer coefficients, numerical discretization, solution of the discretized equations, double pass configuration and validation of the developed model will be discussed in the subsequent sections of the chapter.

2.1. Problem description of parabolic trough collector

The solar radiation absorbed by PTC depends on the optical properties of the materials (glass cover and receiver) such as transmittance of the cover (τ), surface reflectivity of the collectors (ρ_o), and absorptance of the receiver (α). In addition, it is also characterized by the temporal, spatial and atmospheric factors. Furthermore, shape factor (γ) and incident angle modifier (I_{AM}) affect the energy absorbed by the receiver of the PTC. Where shape factor can be defined as the fraction of solar radiation intercepted by the receiver. Energy absorbed per unit collector area by the receiver tube, q_{SR} (W/m^2), can be represented as:

$$q_{SR} = G_n \rho_o \tau \alpha \gamma I_{AM} \tag{1}$$

where G_n (W/m^2) represents the reflected beam component of the global solar radiation from the parabolic mirrors. Beam radiation reflected by the collectors to the receiver tube defines the concentration ratio of the PTC as:

$$CR = \frac{W - D_{ro}}{\pi D_{ro}} \tag{2}$$

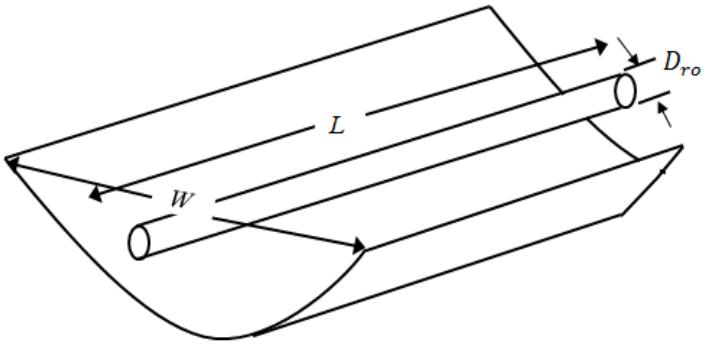

Figure 5: Schematic of PTC showing width, length and receiver's diameter.

Figure 5 represents the schematic description of the PTC, where W is the width of the collector and D_{ro} is the outside diameter of the receiver tube. Useful energy gained by the working fluid in the receiver depends on receiver and glass cover temperatures as they determine thermal losses through convection and radiation. Useful energy gain (defined at steady state), q_u (W/m^2), to the working fluid accounting all the above factors and losses is given by:

$$q_u = q_{SR}CR - \left(H_{con,rc} + H_{rad,rc}\right)(T_r - T_c) \tag{3}$$

where $H_{con,rc}$ and $H_{rad,rc}$ are the convective and radiative heat transfer coefficients between the receiver and glass cover and T_r and T_c are the receiver and cover temperatures, respectively.

Temperatures of the receiver, glass cover and heat transfer fluid are highly coupled and depend upon different modes of heat transfer of the system. Figure 6 shows the detail description of the modes of heat transfer for single pass PTC as well as showing the side view to demonstrate the numerical control volume detail. In Figure 6, q_{wall} is the heat transfer between the receiver and the working fluid which depends on receiver and fluid temperatures and the heat transfer coefficient between receiver and fluid, $q_{r,c}$ is the heat loss from the receiver which depends upon the temperatures and convective/radiative heat transfer coefficients between the receiver and glass cover, whereas $q_{c,amb}$ is the heat loss from the glass cover to the environment.

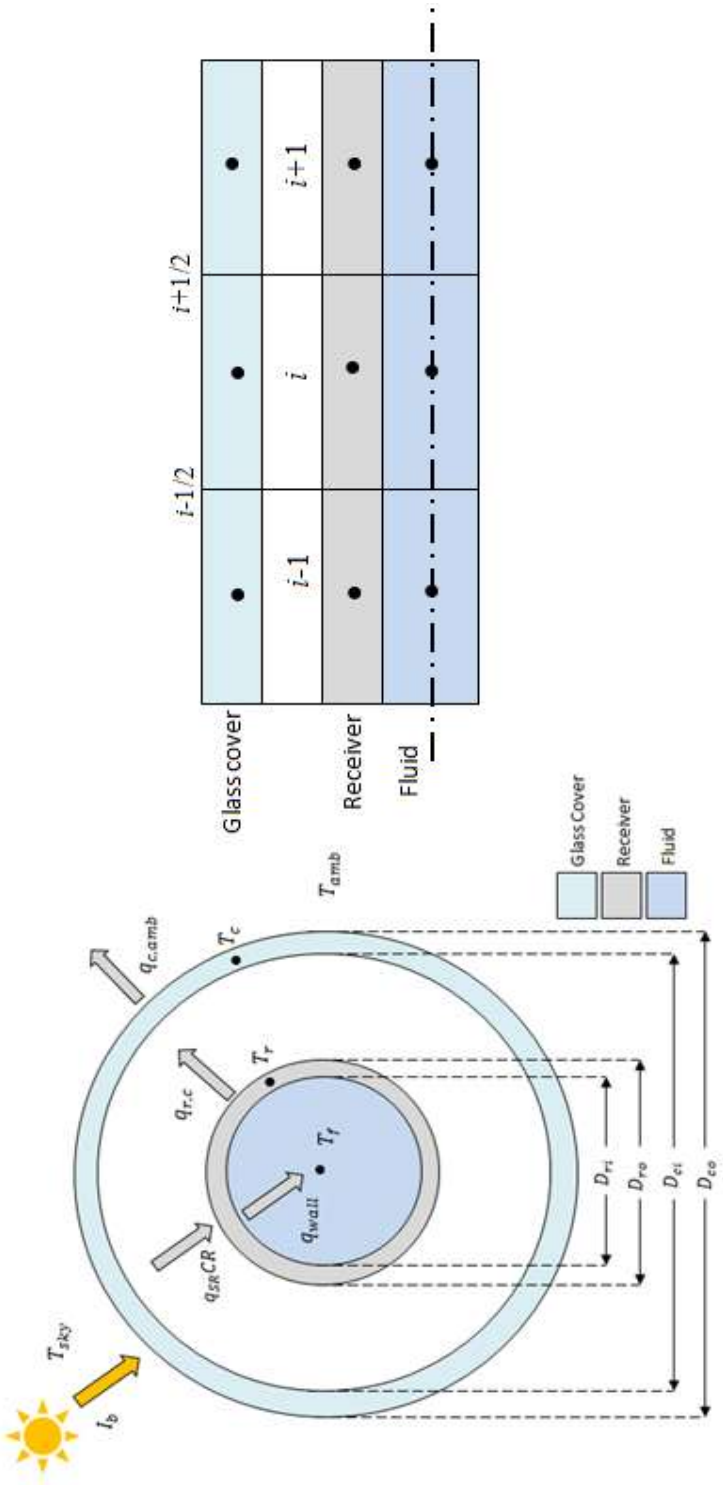

Figure 6: Front and side view of single pass PTC, showing modes of heat transfer and numerical nodes

For the current PTC analysis, following assumptions are considered:

1. Uniform and incompressible fluid flow neglecting any change of phase of the fluid with in the working temperature range.
2. Material properties of air, receiver and glass cover are considered as constant with in the working temperature range.
3. Constant wind velocity for the convective heat loss between glass cover and surroundings.
4. Constant diameters of receiver and glass cover.

Transient energy balance equations are solved separately using finite volume method in a segregated manner to obtain the temperature distributions of fluid flow, annulus (for double pass), internal tube (for double pass), receiver and glass cover . Figure 7 represents the flow of the numerical algorithm. The solution starts with the initial assignment of geometry and optical parameters for the PTCs. An initial temperature distribution for all components is assigned to start the solution. First, temperature profile at a new time step of the fluid is calculated using temperature values of the receiver at the previous time step (${T_{r_i}}^{t}$). The receiver temperature profile serves as the boundary condition for the fluid accounting the convective heat transfer between the receiver and fluid. All the material properties for the evaluation of heat transfer coefficient are calculated at each time step using the previous known temperature distribution.

In the receiver analysis, the calculated temperature profile of fluid at new time step (${T_{f_i}}^{t+1}$) is used for the computation of receiver's temperature profile at new time step along with the previous temperature distributions of the receiver and glass cover. The convective heat transfer coefficient is recalculated at new temperature profile of the fluid along with the useful energy (q_u) as the boundary condition. The matrix inversion is carried out for each time step.

The new temperature profile of the glass cover is obtained with the aid of the updated receiver's temperature profile. Convective and radiative heat transfer coefficients between the receiver and environment are calculated using the most updated version of temperatures (${T_{r_i}}^{t+1}$ and ${T_{c_i}}^{t}$) and given ambient conditions. Similar to the receiver analysis matrix inversion is carried out for every time step to get the new temperature profile of the glass cover.

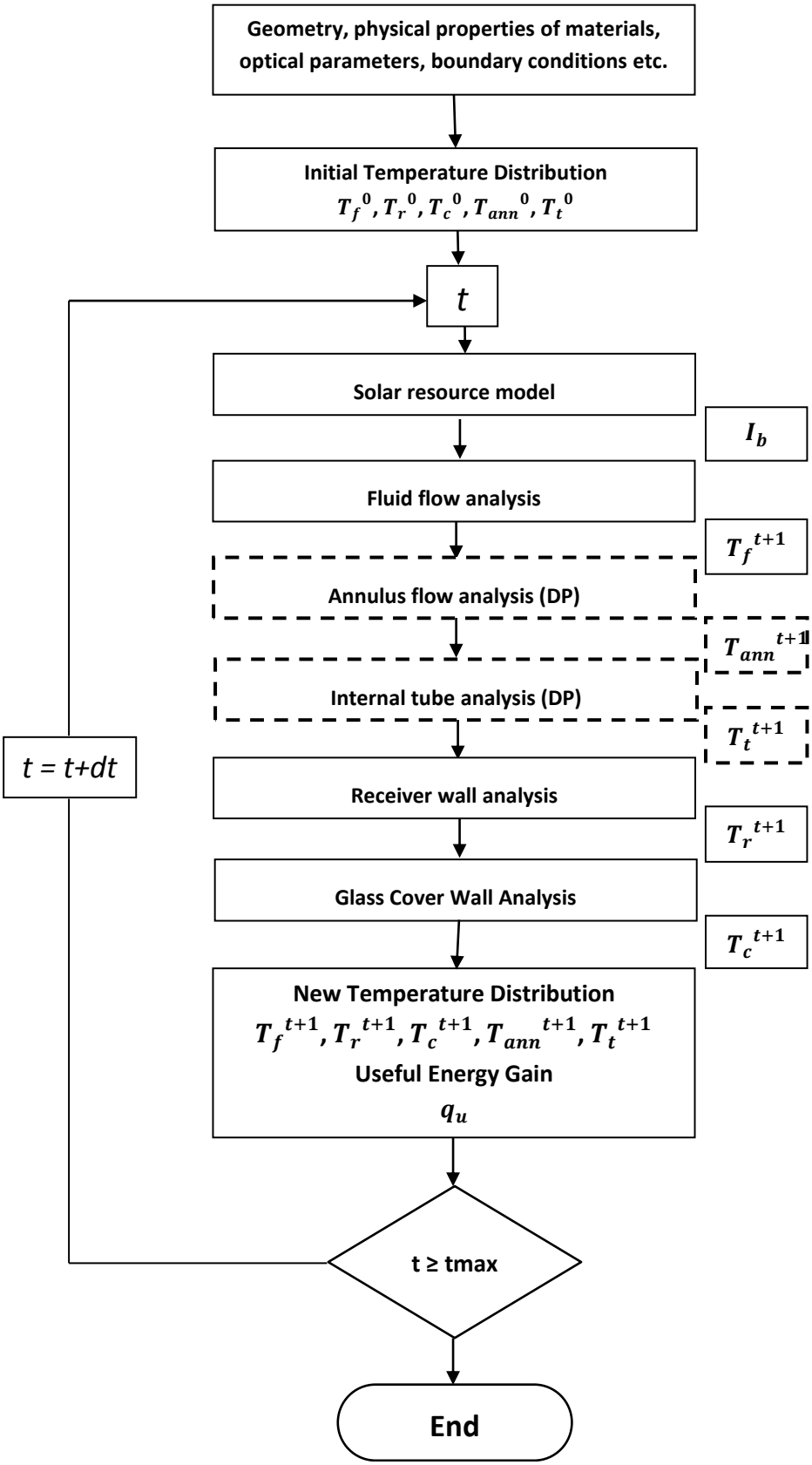

Figure 7: Flow Chart of the PTC numerical algorithm

The useful energy gained by the system at every time step is calculated by using Equation (3) with the corresponding temperature differences. To converge the solution, the simulation is run for an adequate time to reach the steady state for all the system temperatures of fluid, receiver, annulus (for double pass) and glass cover.

2.2. Solar Resource Model

Concentrated solar power technologies utilize only the beam component of the solar radiations and beam radiation reaches the earth surface without any hindrances (absorption and reflection) from the atmosphere. On the other hand, the diffuse part of the solar radiations reaches the earth surface after being scattered from the water molecules, dusts etc. in the atmosphere.

The atmospheric effects are highly variable with time as the atmospheric conditions and air mass change. In order to resolve the unpredictability of the solar resources, it is necessary to define a standard "*clear*" sky model which does not take into account the atmospheric effects to calculate the solar radiation across the course of the day.

Hottel [33] proposed a method to calculate the beam solar resources through the clear sky taking into account the zenith angle and altitude for the four climatic types by defining the atmospheric transmittance for beam radiation as;

$$\tau_b = \frac{G_n}{G_{on}} = a_0 + a_1 exp\left(\frac{-k}{\cos\theta_z}\right) \tag{4}$$

Where G_n is clear sky beam normal radiation, G_{on} is the extraterrestrial radiation incident on the plane normal to the radiation and θ_z is the zenith angle (the angle between the vertical line and the line of the sun).

$$G_{on} = G_{sc}\left(1 + 0.033\cos\frac{360n}{365}\right) \tag{5}$$

$$cos\,\theta_z = cos\,\phi\,cos\,\delta\,cos\,\omega + sin\,\phi\,sin\,\delta \tag{6}$$

Where G_{sc} is the solar constant taken as 1367 W/m^2, n is the day number of the year, ϕ is the latitude of the location, δ is the declination (the angular position of the sun at solar noon) and ω is the hour angle (the angular displacement of the sun by 15° per hour east or west in a day). Declination angle and hour angle can be calculated as;

Table 2 Correction factor for Climatic types

Climate Type	r_0	r_1	r_k
Tropical	0.95	0.98	1.02
Midlatitude summer	0.97	0.99	1.02
Subarctic summer	0.99	0.99	1.01
Midlatitude winter	1.03	1.01	1

$$\delta = 23.45\, sin\left(360\frac{284+n}{365}\right) \tag{7}$$

$$\omega = (solar\ time - 12) \times 15^{\circ} \tag{8}$$

In Equation (4) a_0, a_1 and k are the constants for the standard atmosphere with 23 km visibility and altitudes less than 2.5 km, and can be found from the following relations of a_0^*, a_1^* and k^*.

$$a_0^* = 0.4237 - 0.00821(6 - A)^2 \tag{9}$$

$$a_1^* = 0.5055 - 0.00595(6.5 - A)^2 \tag{10}$$

$$k^* = 0.2711 - 0.01858(2.5 - A)^2 \tag{11}$$

$r_0 = a_0/a_0^*$, $r_1 = a_1/a_1^*$ and $r_k = k/k^*$ are the correction factors for different type of climate types summarized in Table 2 and '*A*' represents the altitude of the location.

2.3. Fluid flow analysis

Finite volume representation of the fluid flow inside receiver tube is given in Figure 8. As the fluid flow is considered without phase change, only the transient energy equation is solved for the evaluation of the fluid temperature. Transient governing energy equation for *i*th control volume is given in Equation (12).

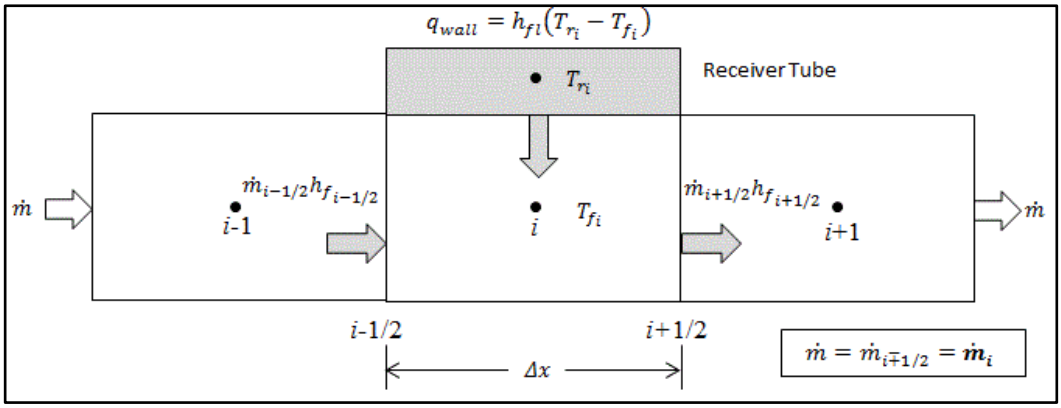

Figure 8. Control volume for the fluid flow inside the receiver tube.

$$\frac{dE_i}{dt} = q_{wall} + \dot{m}_{i-1/2} h_{f\,i-1/2} - \dot{m}_{i+1/2} h_{f\,i+1/2} \tag{12}$$

In Equation (12), E_i represent the total energy for the *i*th control volume. The heat transfer from the receiver to fluid (q_{wall}) depends upon the temperature difference of fluid and receiver and the convective heat transfer coefficient.

$$q_{wall} = H_{fl}(T_r - T_f) \tag{13}$$

Convective heat transfer coefficient H_{fl} for the fluid flow inside the receiver is calculated with the aid of Gnielinski correlation for turbulent flows (Re_f > 2300), with constant heat flux assumption given by [34]:

$$\begin{gathered} Nu_f = \frac{(f/8)(Re_f - 1000)Pr_f}{1 + 12.7\sqrt{(f/8)}\left(Pr_f{}^{2/3} - 1\right)} \\ h_{fl} = \frac{Nu_f k_f}{D_{ri}} \end{gathered} \tag{14}$$

where friction factor, f, and Reynolds number, Re_f are given by

$$f = \left(1.82 log_{10} Re_f - 1.64\right)^{-2} \tag{15}$$

$$Re_f = \frac{\dot{m}_i D_{ri}}{A_r \mu_f} \tag{16}$$

In Equation (15) Re_f is calculated with the aid of hydraulic diameter of the receiver tube, which is calculated as the cross-sectional area divided by quarter of the wetted perimeter of the cross-section.

For laminar flows, i.e. Reynolds number less than 2300, convective heat transfer coefficient, H_{fl}, can be calculated using Equation (17).

$$H_{fl} = \frac{4.36\ k_f}{D_{ri}} \tag{17}$$

Continuity for incompressible flows suggests that mass flow rate throughout the pipe is constant, i.e. $\dot{m}_{i+1/2} = \dot{m}_{i-1/2} = \dot{m}$. Using incompressible substance model with constant mass flow rate, Equation (12) becomes:

$$\rho_f \Delta V_f \frac{c_{pf} T_{f_i}^{t+1} - c_{pf} T_{f_i}^{t}}{\Delta t} = H_{fl}\left(T_{r_i}^{t} - T_{f_i}^{t+1}\right) A_{fl} + \dot{m}\left(c_{pf} T_{f_{i-1/2}}^{t+1} - c_{pf} T_{f_{i+1/2}}^{t+1}\right) \tag{18}$$

After applying 1st order upwind scheme on Equation (18), the fluid temperature at node i, $T_{f_i}^{t}$, is advanced to the new time level, $t + \Delta t$, using the following relation:

$$T_{f_i}{}^{t+1} = \frac{(a) T_{f_{i-1}}{}^{t+1} + c_{p_f} T_{f_i}{}^{t} + (b) T_{r_i}{}^{t} - (b) T_{f_i}{}^{t}}{c_{p_f} + a} \tag{19}$$

$$a = \frac{\dot{m}_i c_{p_f} \Delta t}{\rho_f \Delta V_f}, b = \frac{A_{fl} h_{fl} \Delta t}{\rho_f \Delta V_f}$$

Equation (19) produces temperature distribution of the working fluid at a new time step using a semi implicit approach which solves by taking old and new time step values. Above equation is modified for the inlet boundary node (node 1). It is assumed that the fluid enters the receiver at a constant temperature. Hence for node 1 the temperature at new time step is:

$$T_{f_1}{}^{t+1} = T_{f_i}{}^{t} \tag{20}$$

2.4. Receiver wall analysis

Energy balance equation for the receiver wall is developed using the scheme presented in Figure 9 as given in Equation (21).

$$m_r \frac{du_r}{dt} = (q_u \pi D_{ro} - q_{wall} \pi D_{ri}) \Delta x + \left(k_r \left.\frac{dT_r}{dx}\right|_{i+1/2} - k_r \left.\frac{dT_r}{dx}\right|_{i-1/2} \right) A_{cr} \tag{21}$$

In Equation (21), q_{wall} is calculated using Equation (13) with the fluid temperature at the new time step ($T_{f_i}{}^{t+1}$) while q_u is calculated using Equation (3) with the previous time step's glass cover temperature (T_{ci}^{t}).

In Equation (3), $H_{con,rc}$and $H_{rad,rc}$ are the convective and radiative heat transfer coefficients between the receiver and glass cover and are calculated by:

$$H_{con,rc} = \frac{2 k_{eff}}{D_{ro} ln\left(\frac{D_{ci}}{D_{ro}}\right)} \tag{22}$$

where k_{eff} is the effective thermal conductivity of the air, trapped in between the receiver and glass cover envelope and D_{ci} is the internal diameter of the glass cover. Effective

thermal conductivity of the air depends upon the Rayleigh number (Ra) based on the temperature difference and the characteristic length between the receiver and glass cover.

$$k_{eff} = \left(0.317 Ra^{*1/4}\right) k_a \tag{23}$$

$$Ra^{*1/4} = \left[\frac{ln\left\{\frac{D_{ci}}{D_{ro}}\right\}}{b^{3/4}\left\{\frac{1}{{D_{ro}}^{3/5}} + \frac{1}{{D_{ci}}^{3/5}}\right\}^{5/4}} \right] Ra^{1/4} \tag{24}$$

In the above relation, b is the characteristic length and Ra is the Rayleigh number which is calculated using the following relations.

$$b = \frac{D_{ci} - D_{ro}}{2} \tag{25}$$

$$Ra = \frac{g\beta \Delta T b^3}{\nu_a \alpha_a} \tag{26}$$

Radiative heat transfer coefficient between the receiver and glass cover is given by;

$$H_{rad,rc} = \frac{\sigma\left({T_r}^2 + {T_c}^2\right)(T_r + T_c)}{\frac{1-\varepsilon_r}{\varepsilon_r} + \frac{1}{F_{rc}} + \frac{(1-\varepsilon_c)D_{ro}}{\varepsilon_c D_{ci}}} \tag{27}$$

Integrating Equation (21) with respect to time and space using implicit approach for the middle nodes yields Equation (28).

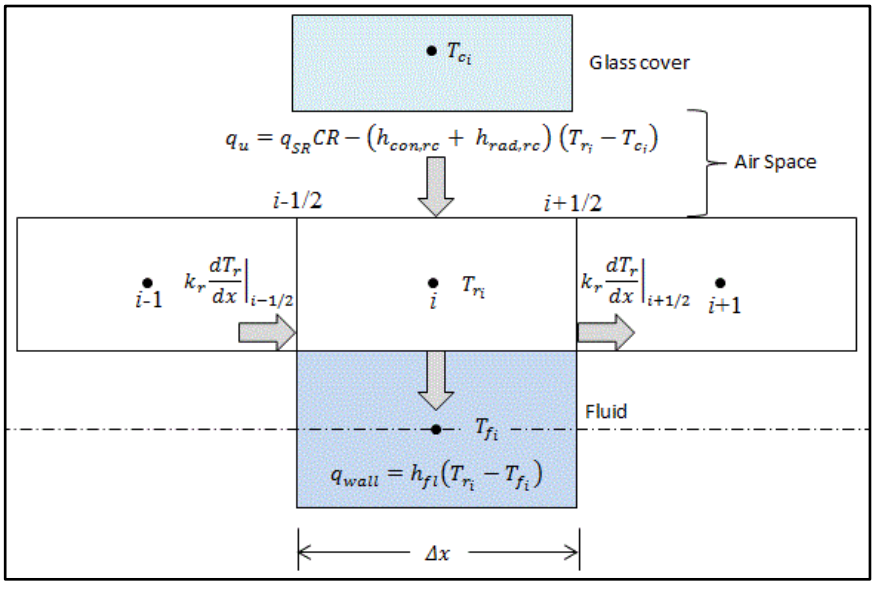

Figure 9. Computational scheme for the receiver tube.

Table 3: Summary of the coefficients for receiver temperature profile.

Nodes	$a_{r,i-1}$	$a_{r,i+1}$	$a_{r,i}$	$b_{r,c}$
$i = 1$	0	$\frac{k_r A_{cr}}{\Delta x}$		
$1 < i < n$	$\frac{k_r A_{cr}}{\Delta x}$	$\frac{k_r A_{cr}}{\Delta x}$	$\alpha + \beta + a_{r,i+1} + a_{r,i-1}$	$\alpha {T_{r,i}}^{t} + \beta {T_{f,i}}^{t+1} + \gamma$
$i = n$	$\frac{k_r A_{cr}}{\Delta x}$	0		

$$\alpha = \frac{\rho_r \Delta V_r C_{p_r}}{\Delta t} \qquad \beta = H_{fl} \pi D_{ri} dx \qquad \gamma = q_u \pi D_{ro} \Delta x$$

$$\rho_r \Delta V_r \frac{{u_{r_i}}^{t+1} - {u_{r_i}}^{t}}{\Delta t} = \{q_u \pi D_{ro} - H_{fl}({T_{f_i}}^{t+1} - {T_{r_i}}^{t+1})\pi D_{ri}\}\Delta x + \left[k_r \left(\frac{{T_{r_{i+1}}}^{t+1} - {T_{r_i}}^{t+1}}{\Delta x}\right) - k_r \left(\frac{{T_{r_i}}^{t+1} - {T_{r_{i-1}}}^{t+1}}{\Delta x}\right)\right] A_{cr} \tag{28}$$

Specific internal energy is represented via specific heats, i.e. $u_r = c_{p_r} T_r$, to obtain Equation (29) as:

$$\rho_r \Delta V_r c_{p_r} \frac{{T_{r_i}}^{t+1} - {T_{r_i}}^{t}}{\Delta t} = \{q_u \pi D_{ro} - H_{fl}({T_{r_i}}^{t+1} - {T_{f_i}}^{t+1})\pi D_{ri}\}\Delta x + \left[k_r \left(\frac{{T_{r_{i+1}}}^{t+1} - {T_{r_i}}^{t+1}}{\Delta x}\right) - k_r \left(\frac{{T_{r_i}}^{t+1} - {T_{r_{i-1}}}^{t+1}}{\Delta x}\right)\right] A_{cr} \tag{29}$$

Receiver tubes' temperatures of Equation (29) can be combined together as shown in Equation (30) so that a linear system can be formed. The coefficients are summarized in Table 3 when adiabatic boundary conditions are applied on the boundary nodes (1st and the last).

$$(a_{r,i}){T_{r,i}}^{t+1} - (a_{r,i-1}){T_{r,i-1}}^{t+1} - (a_{r,i+1}){T_{r,i+1}}^{t+1} = b_{r,c} \tag{30}$$

Temperature profile of the receiver at new time steps can be found by the solving *n* number of equations for middle nodes, 1st node and nth node simultaneously with the help of matrix inversion. The coefficients in Table 3 form the diagonally dominant matrix presented below.

2.5. Glass cover wall analysis

The glass cover analysis is similar to the numerical method described for the receiver tube. Using Figure 10, energy balance across the control volume of the cover is given by Equation (31).

$$m\frac{du_c}{dt} = \left(q_{r,c}\pi D_{ro} - q_{c,amb}\pi D_{co}\right)dx + (\dot{q}_e - \dot{q}_w)A_{cc} \tag{31}$$

where $q_{r,c}$ represents the convective and radiative heat transfer between the cover and the receiver, as given by:

$$q_{r,c} = \left(H_{con,rc} + H_{rad,rc}\right)(T_r - T_c) \tag{32}$$

where convective and radiative heat transfer coefficients can be computed using Equations (22) and (27) using most recent temperature values for the receiver and the glass cover.

The second term in Equation (31) represents energy loss from the glass cover to the atmosphere, and given by:

$$q_{c,amb} = H_{con,c\,amb}(T_c - T_{amb}) + H_{rad,c\,amb}\left(T_c - T_{sky}\right) \tag{33}$$

where, $H_{con,c\,amb}$ and $H_{rad,c\,amb}$ are convective and radiative heat transfer coefficients between the glass cover surface and environment respectively. Correlations for the

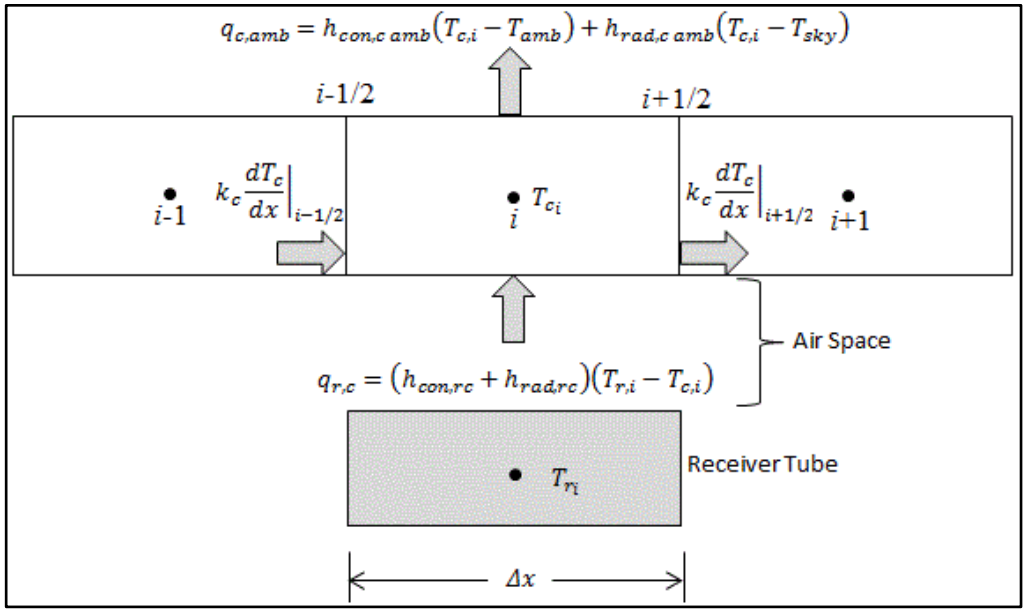

Figure 10. Computational scheme for the glass cover.

convective heat transfer coefficient are available with for a wide range of Re number in the literature.

$$H_{con,camb} = \begin{cases} 0.989 Re^{0.33} {Pr_a}^{0.33} \dfrac{k_a}{D_{co}} & for\ \ 0.4 < Re \leq 40 \\ 0.683 Re^{0.486} {Pr_a}^{0.33} \dfrac{k_a}{D_{co}} & for\ \ 40 < Re \leq 4000 \\ 0.193 Re^{0.618} {Pr_a}^{0.33} \dfrac{k_a}{D_{co}} & for\ \ 4000 < Re \leq 40{,}000 \\ 0.0266 Re^{0.805} {Pr_a}^{0.33} \dfrac{k_a}{D_{co}} & for\ \ 40{,}000 < Re \leq 400{,}000 \end{cases} \tag{34}$$

For very low air velocities or stagnant air, the natural convective heat transfer correlation around the cylinder is proposed by Churchill and Chu [19].

$$H_{con,camb} = \left[0.6 + 0.387 \left\{ \frac{Ra}{\left(1 + \left(\frac{0.559}{Pr_a} \right)^{9/16} \right)^{16/9}} \right\}^{1/6} \right]^2 \frac{k_a}{D_{co}} \tag{35}$$

where the Ra number depends upon glass cover outside diameter (D_{co}), the characteristic length and the temperature difference between the glass cover surface and the ambient environment. The radiative heat transfer coefficient $H_{rad,c\ amb}$ is given by;

$$H_{rad,c\ amb} = \varepsilon_c \sigma \left({T_{sky}}^2 + {T_c}^2 \right) \left(T_{sky} + T_c \right) \tag{36}$$

Similar to the receiver analysis, integrating the Equation (31) with respect to time and space using implicit approach for the middle nodes and substituting the above equations leads to the following simplified and discretized equations.

$$\begin{aligned} \rho_c \Delta V_c \frac{{u_{c_i}}^{t+1} - {u_{c_i}}^{t}}{\Delta t} &= \left[\left(H_{con,rc} + H_{rad,rc} \right) \left(T_{r,i} - T_{c,i} \right) \pi D_{ro} \right. \\ &\quad - \left\{ H_{con,c\ amb} \left(T_{c,i} - T_{amb} \right) + H_{rad,c\ amb} \left(T_{c,i} - T_{sky} \right) \right\} \pi D_{co} \left. \right] \Delta x \\ &\quad + \left(k_c \left. \frac{dT_c}{dx} \right|_{i+1/2} - k_c \left. \frac{dT_c}{dx} \right|_{i-1/2} \right) A_{cc} \end{aligned} \tag{37}$$

Specific internal energy is represented via specific heats, i.e. $u_c = c_{p_c} T_c$, to obtain Equation (38) as:

$$\rho_c \Delta V_c c_{p_c} \frac{{T_{c_i}}^{t+1} - {T_{c_i}}^{t}}{\Delta t} = \left[\left(H_{con,rc} + H_{rad,rc}\right)\left({T_{r,i}}^{t+1} - {T_{c,i}}^{t+1}\right)\pi D_{ro} - \left\{H_{con,c\,amb}\left({T_{c,i}}^{t+1} - T_{amb}\right) + H_{rad,c\,amb}\left({T_{c,i}}^{t+1} - T_{sky}\right)\right\}\pi D_{co}\right]\Delta x + \left[k_c\left(\frac{{T_{c_{i+1}}}^{t+1} - {T_{c_i}}^{t+1}}{\Delta x}\right) - k_c\left(\frac{{T_{c_i}}^{t+1} - {T_{c_{i-1}}}^{t+1}}{\Delta x}\right)\right]A_{cc} \quad (38)$$

After simplifications Equation (38) and the two discretized equations for the boundary nodes, the equations take the following discretized form.

$$\left(a_{c,i}\right){T_{c,i}}^{t+1} - \left(a_{c,i-1}\right){T_{c,i-1}}^{t+1} - \left(a_{c,i+1}\right){T_{c,i+1}}^{t+1} = b_{c,c} \quad (39)$$

where the coefficients of the variables at different spatial nodes are summarized in Table 4 for adiabatic conditions applied at the 1st and the last control volumes. Temperature profile of the glass cover at new time steps can be found by the solving *n* number of equations for middle nodes, 1st node and nth node simultaneously with the help of matrix inversion.

Table 4: Summary of the coefficients for glass cover temperature profile.

Nodes	$a_{c,i-1}$	$a_{c,i+1}$	$a_{c,i}$	$b_{c,c}$
$i = 1$	0	$\frac{k_r A_{cr}}{\Delta x}$	$\beta_{rc} + \beta_{con} + \beta_{rad} + \alpha + a_{c,i+1} + a_{c,i-1}$	$\alpha {T_{c,i}}^{t} + \beta_{rc} {T_{r,i}}^{t+1} + \beta_{con} T_{amb} + \beta_{rad} T_{sky}$
$1 < i < n$	$\frac{k_r A_{cr}}{\Delta x}$	$\frac{k_r A_{cr}}{\Delta x}$		
$i = n$	$\frac{k_r A_{cr}}{\Delta x}$	0		

$\alpha = \frac{\rho_c \Delta V_c C p_c}{\Delta t}$ $\quad \beta_{rc} = \left(H_{con,rc} + H_{rad,rc}\right)\pi D_{ro}\Delta x$ $\quad \beta_{con,amb} = H_{con,camb}\pi D_{co}\Delta x$

$\beta_{rad,amb} = H_{rad,camb}\pi D_{co}\Delta x$

2.6. Validation of the Parabolic Trough Collector Model (Single pass)

It is essential to validate the numerical model before proceeding forward for further analysis. In order to validate the numerical model, experimental as well as numerical data is found from the literature and compared with the developed model. Sandia National Laboratory has carried out several experiments on single pass parabolic trough collector with air and vacuum between the receiver and glass cover. They used single phased water for low, and syltherm800 oil for high temperature ranges respectively in their experiments. Tests were carried out on different conditions of solar energy input and mass flow rates.

Table 5: Single Pass Parabolic Trough Collector specifications for model validation.

Geometrical Specifications	
Receiver length (L)	7.8 m
Collector width (w)	5 m
Receiver internal diameter ($\boldsymbol{D_{ri}}$)	0.066 m
Receiver outside diameter ($\boldsymbol{D_{ro}}$)	0.070 m
Cover internal diameter ($\boldsymbol{D_{ci}}$)	0.109 m
Cover outside diameter ($\boldsymbol{D_{co}}$)	0.115 m
Concentration ratio ($\boldsymbol{CR}$)	22.42
Optical Specifications	
Receiver absorptance ($\boldsymbol{\alpha}$)	0.906
Receiver emittance ($\boldsymbol{\varepsilon_r}$)	0.14
Glass cover transmittance ($\boldsymbol{\tau_c}$)	0.95
Surface reflectivity ($\boldsymbol{\rho_o}$)	0.93
Shape factor (γ)	0.92
Incident angle ($\boldsymbol{\theta}$)	0°
Incidence angle modifier ($\boldsymbol{I_{AM}}$)	1
Material Specifications	
Working fluids	Water and
Receiver material	Stainless steel cermet
Glass cover material	Low iron glass

With almost perfect tracking, zero degree incident angle is achieved (radiation perfectly normal to the surface) with the aid of AZTRAK rotating platform at Sandia National Laboratory, at every hour of the day. The developed model is compared with 10 different physical conditions of solar energy input at zero degree incident angle (perfect tracking), water and syltherm800 oil as the working fluids, fluid inlet temperatures and ambient conditions from Sandia's experimental data. Beside the experimental data, the developed numerical model is also validated with the numerical model of O. Garcia-Valladares et al [19] with similar conditions.

The numerical approach for single pass PTC model is validated for non-evacuated tubes which contain air between the receiver and glass cover. Table 5 represents the specifications of the parabolic trough collector for the single pass validation comprising of geometrical, optical and material details.

Validation study assumes constant physical properties of receiver and glass cover material, whereas the thermo-physical properties of the fluid are evaluated at every time step at different temperatures. Property evaluation for water is straight forward whereas the properties of syltherm 800 oil are found from [35] at different temperatures. Best fitted functions are used for the evaluation of thermo-physical properties for the oil, from the

available data. Thermo-physical properties of the air trapped between the receiver/glass cover gap and ambient air are also taken as constant at 20 °C. The details are given in the Appendix.

In order to find the effect of the computational size (Number of nodes *n*) on the error and to achieve grid independency, the model is checked by simulating one single case at various grid sizes (200, 150, 100, 50 and 25 nodes). Results of 200 nodes are considered as the benchmark values to compare with the lesser grid sizes. The error is calculated for both the outlet temperature and useful energy gain at steady state. To check the grid independency, water is taken as the working fluid entering the receiver at 29.5 °C with the flow rate of 20.7 *l*/min (~0.345 kg/sec at constant water density), perfect tracking (0° angle of incident) with incident beam of 925.1 W/m^2 as the solar energy input, 38.4 °C and 3.4 m/s as the ambient temperature and wind speed respectively, are fed into the model as the inputs.

$$Error_T = (T_{200})_o - (T_n)_o \tag{40}$$

Equation (40) represents the error for the outlet temperature (T_n), where the $(T_{200})_o$ and $(T_n)_o$ show the outlet temperature at 200 and lesser nodes (*n*) respectively.

$$Error_{q_u} = \overline{q_u}_{200} - \overline{q_u}_n \tag{41}$$

Similarly, Equation (41) shows the error for the average useful energy gain at the steady state conditions, where $\overline{q_u}_{200}$ and $\overline{q_u}_n$ show the average useful energy gain at steady state conditions at 200 and lesser nodes.

An obvious trend can be observed in Figure 11 and Figure 12, with an increase of number of nodes the error is decreasing. It can be seen from the figures as well that the magnitude of the error is quite insignificant at different number of nodes.

In Figure 11 errors at 150 nodes and 25 nodes are 5.58×10^{-5} and 1.1×10^{-3} respectively. Although there is a difference in the order of the magnitude between these two values but with the temperature ranges and the margin of error in these type of systems, these two nodes almost give the same outlet temperatures. Similarly, for the useful energy absorbed to the system at steady state, different nodes also show insignificant errors. The main reason of this behavior is the adoption of implicit scheme while solving the discretized equations which does not impose strict limits of grid size and time interval between two steps. Hence, in order to save the computational resources, the model is validated with 50 control volumes. The summary of the cases for validation and results are tabulated in Table 6.

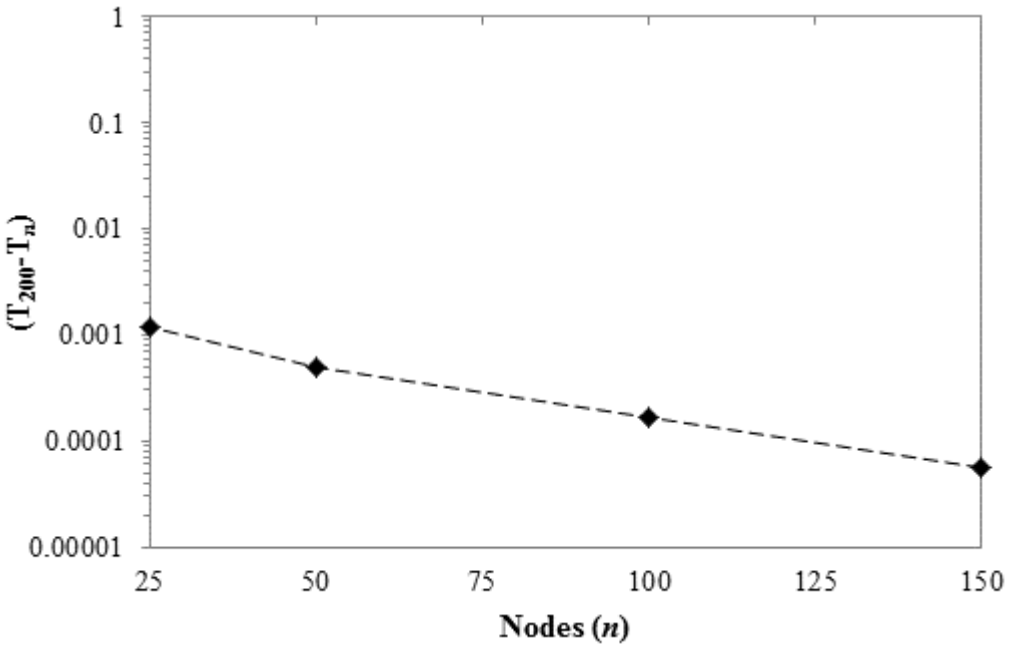

Figure 11: Error (Outlet Temperature at steady state) vs. number of nodes.

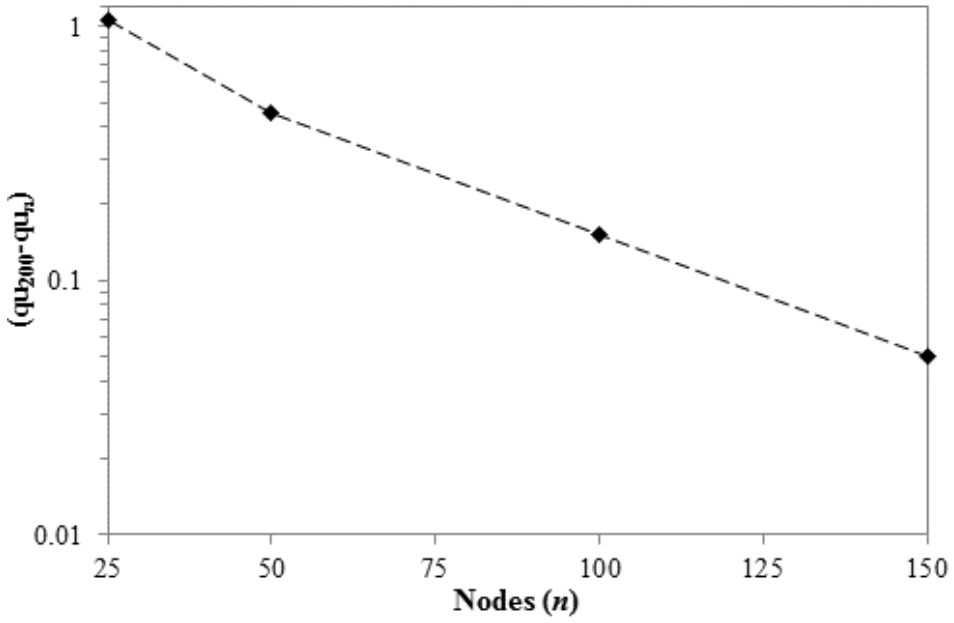

Figure 12: Error (Average energy gain at steady state) vs. number of nodes.

Figure 13 shows the temperature profiles of the inlet, outlet and middle nodes of the computational domain for case 1 (Table 6) for the simulation showing steadiness in the solution. Table 6 shows a wide range of different cases simulated for the validation, with water and oil as the working fluid. Cases with different solar energy inputs and mass flow

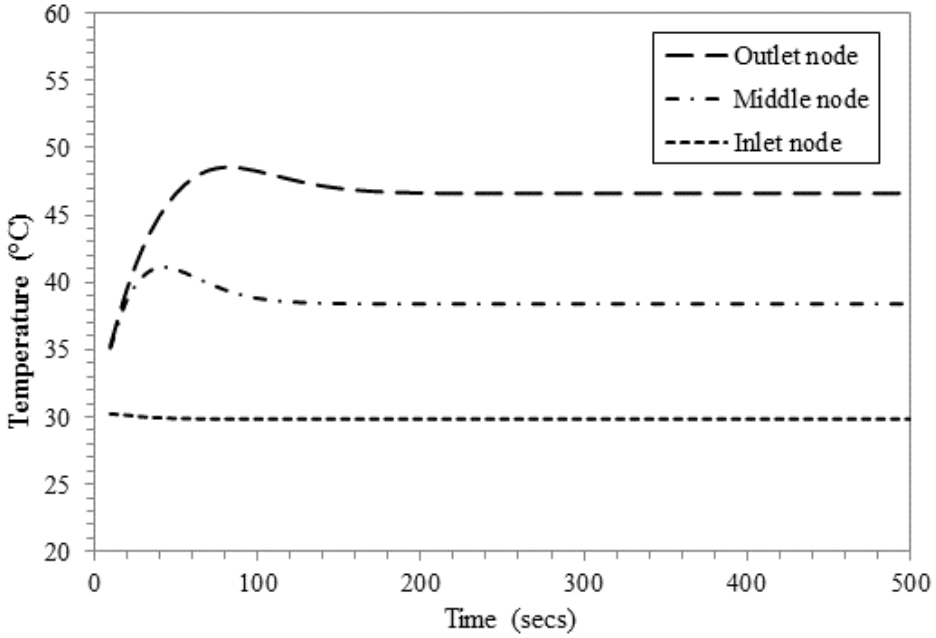

Figure 13: Temperature profiles at different locations in the computational domain for case 1.

rates are validated with increasing inlet temperatures of the working fluid ranging from 29.5 °C for water to very high temperatures up to 376.6 °C for oil. The cases are run for adequate time to achieve the steady state with 50 control volumes. It can be seen from the table that there is a strong agreement of the thermal efficiencies of different cases with that of the O. Garcia-Valladares et al model with an average and maximum error of 0.95% and 1.83% respectively. Beside this it can be observed that the thermal efficiency of the Parabolic Trough Collector is also deceasing with the increase of the working fluid temperatures, evidently due to high thermal (convective and radiative losses) from the receiver and cover surfaces at high surface temperatures. Equation (42) represents the percent thermal efficiency of the Parabolic Trough Collector.

$$\eta_{th} = \left[\frac{q_u \pi D_{ro} L}{I_b (w - D_{ro}) L}\right] \times 100 \tag{42}$$

Figure 14 shows the described decreasing trend of the thermal efficiencies at various inlet working fluid temperatures tabulated in Table 6. Error bars are drawn with an error of 5% along the single pass PTC thermal efficiencies. A good degree of correlation is also found between the temperature difference between the inlet and outlet of the PTC for experiments, O. Garcia-Valladares et al model, and the developed Parabolic Trough Collector model, with an average and maximum error of 3.94% and 6.56%.

Table 6: Summary of the validation cases for Single Pass Parabolic Trough Collector Model with O. Garcia-Valladares et al and Experimental.

Cases	Fluid	I_b (W/m^2)	Flow rate (l/min)	Mass flow rate (kg/s)	Wind speed (m/s)	T_{amb} (°C)	T_{inlet} (°C)	Exp ΔT (°C)	Garcia et.al model ΔT (°C)	PTC model T_{outlet} (°C)	PTC model ΔT (°C)	% Error Garcia et.al vs PTC (ΔT)	q_{useful} (W/m^2)	Garcia et.al η_{th} (%)	PTC η_{th}(%)	% Error Garcia et.al vs PTC (η_{th})	Exp η_{th} (%)
1	Water	925.1	20.7	0.345	3.4	38.4	29.5	17.8	18.04	47.53	18.03	0.03	15158.8	72.11	73.06	1.31	73.7
2	Oil	813.1	50.3	0.72	3.6	25.8	101.2	17.8	16.73	118.46	17.26	3.19	12039.6	67.25	66.02	1.83	71.6
3	Oil	858.4	52.9	0.71	3.1	27.6	154.3	17.4	16.64	171.82	17.52	5.30	12670.7	66.21	65.81	0.60	69.2
4	Oil	878.7	54.6	0.69	3.1	28.6	202.4	17	16.31	219.78	17.38	6.56	12755.0	64.60	64.72	0.18	67.1
5	Oil	889.7	55.3	0.66	2.8	28.6	251.1	17.2	16.23	268.32	17.22	6.13	12610.4	62.89	63.19	0.48	66.6
6	Oil	906.7	55.4	0.61	0	31.7	299.5	17	16.94	317.19	17.69	4.45	12469.6	62.39	61.32	1.72	62.6
7	Oil	874.1	56.2	0.58	4	28.7	344.9	16.2	15.82	361.31	16.41	3.70	11388.4	58.56	58.09	0.81	59.6
8	Oil	870.4	56.2	0.58	0.6	29.1	345.5	16.1	16.11	361.97	16.47	2.26	11876.7	59.74	60.84	1.83	59.4
9	Oil	879.5	55.4	0.57	1.8	27.4	348.9	16.3	16.35	365.93	17.03	4.14	11655.2	58.99	59.08	0.16	58.5
10	Oil	898.6	56.2	0.55	2.8	29.7	376.6	16.5	16.47	393.67	17.07	3.65	11520.5	56.83	57.16	0.58	56.5

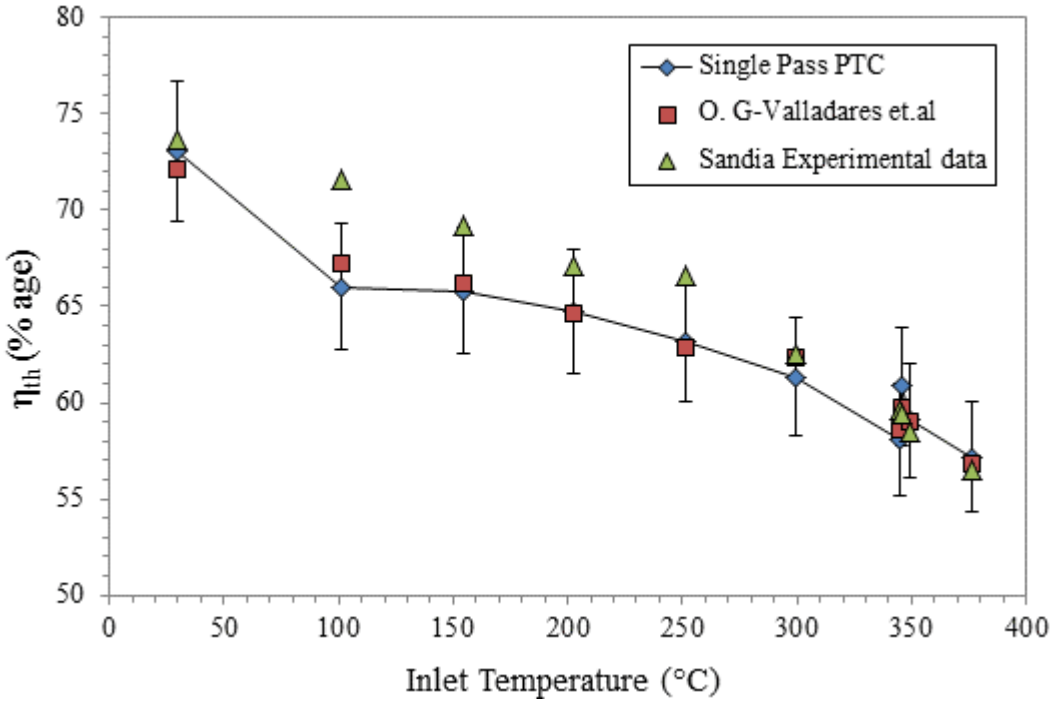

Figure 14: Trend of thermal efficiency with the inlet working fluid temperatures.

The difference between the results of developed model of single pass PTC and model of Valladares et al is due to the numerical approach they adopted. They discretized the momentum equation along with the energy equations, whereas the developed PTC model solved for the energy balance. It can be said that by solving only the energy equation, the results are in a very good agreement with the Valladares et al model and this analytic approach significantly reduces the computational time and resources.

2.7. Parabolic Trough Collector Model Double Pass

The developed numerical model of single pass PTC is extended to model a double pass PTC. A double pass PTC is modeled as a concentric counter flow heat exchanger. The incoming fluid to the PTC pre mixes with the fluid from the annulus before entering the internal tube of the double pass configuration. This pre mixing increases the inlet temperature of the incoming fluid. This concept is broadly used in other thermal applications as well and can be observed in absorption, fermentation and polymerization industries [19]. The details of the numerical modeling is presented in the subsequent section.

2.7.1. Numerical modeling

The double pass PTC has one additional tube with fluid flow enveloped inside the receiver. Hence, internal tube fluid flow and annulus flow in the opposite direction are integrated into the PTC model. All the energy equations are coupled with each other through surface boundary conditions. Figure 15 shows the schematic of the double pass PTC, with mixing of the incoming fluid at a constant mass flow rate ($\dot{m}$) with the exiting fluid at $M\dot{m}$.

Similar numerical discretization is carried out as of the single pass PTC except a few differences in fluid flow equations in the annulus, as given in Equation (43).

$$\frac{dE_i}{dt} = q_{wall_r} - q_{wall_t} + \dot{m}_{i-1/2} h_{f_{i-1/2}} - \dot{m}_{i+1/2} h_{f_{i+1/2}} \tag{43}$$

where q_{wall_r} and q_{wall_t} are the heat transfer from the receiver to the annulus fluid and heat transfer from the fluid to the internal tube.

$$q_{wall_r} = h_{ann} A_{ann} (T_r - T_{ann}) \tag{44}$$

$$q_{wall_t} = h_{ann} A_{ann} (T_{ann} - T_t) \tag{45}$$

Where subscript *ann* represents annulus and *t* represents internal tube.

Following Figure 15 and Figure 16, Equation (46) is developed for the discretized energy equation, where subscript *f* represents the fluid flow inside the internal tube.

$$\begin{aligned} \rho_t \Delta V_t C_{p_t} \frac{{T_{t_i}}^{t+1} - {T_{t_i}}^{t}}{\Delta t} &= \left[H_{ann}\left({T_{ann_i}}^{t} - {T_t}^{t+1}\right) A_{ann} - H_f\left({T_t}^{t+1} - {T_f}^{t+1}\right) A_f\right] \\ &+ \left[k_t \left(\frac{{T_{t_{i+1}}}^{t+1} - {T_{t_i}}^{t+1}}{\Delta x}\right) - k_t \left(\frac{{T_{t_i}}^{t+1} - {T_{t_{i-1}}}^{t+1}}{\Delta x}\right)\right] A_t \end{aligned} \tag{46}$$

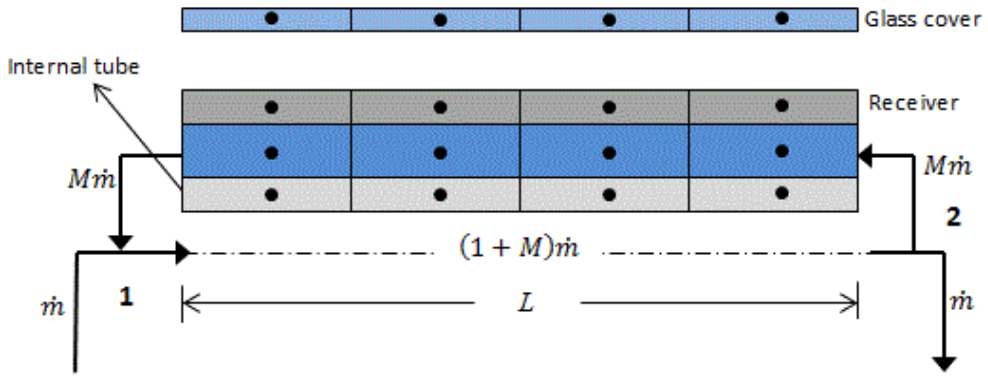

Figure 15: Schematic for the double pass PTC (Counter flow heat exchanger).

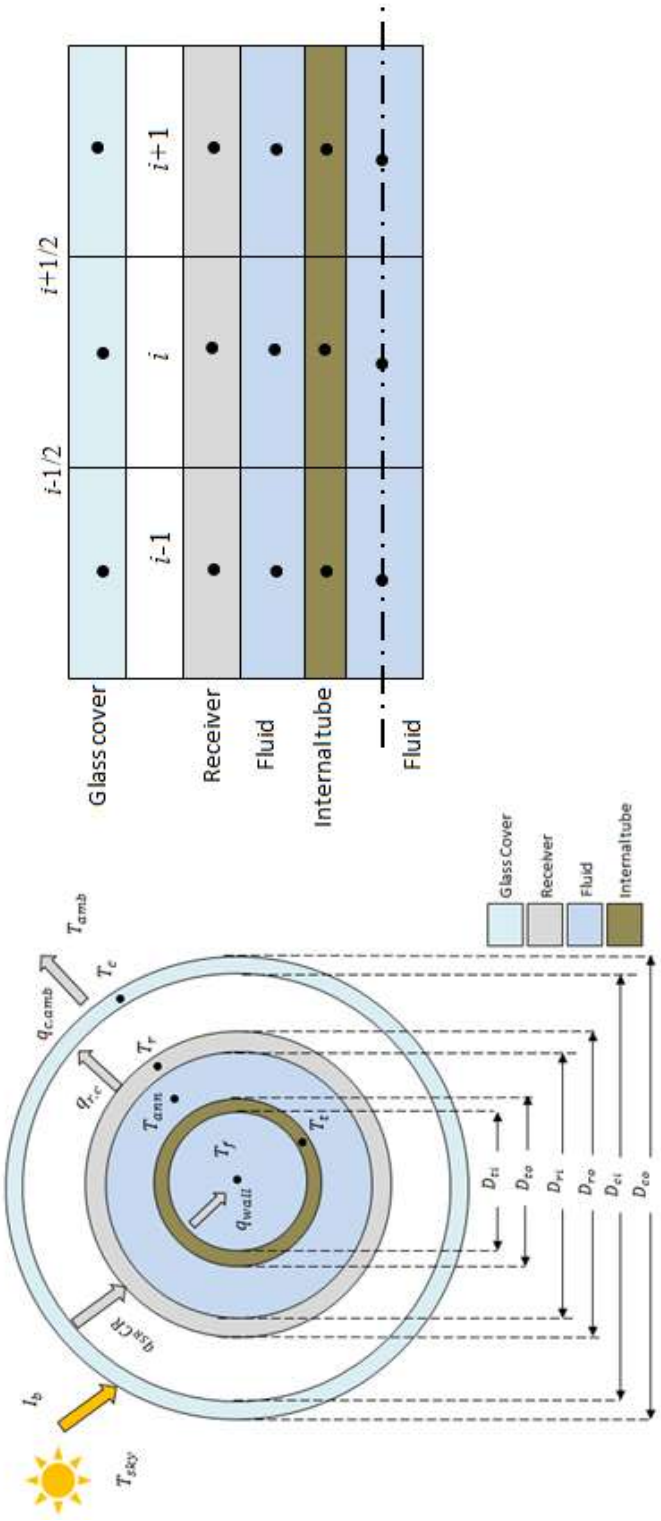

Figure 16: Front and side view of single pass PTC, showing modes of heat transfer and numerical nodes.

In the Figure 15 point '1' refers to the mixing of the two streams, which serves as the boundary condition for the internal tube fluid flow. At the first node the temperature of the fluid is calculated by;

$$T_{f_1} = \frac{\dot{m}T_{f_C} + (M\dot{m})T_{ann_N}}{\dot{m} + M\dot{m}} \tag{47}$$

In the above equation, it is assumed that the incoming water at $\dot{m}$ is at constant temperature T_{f_C}, and *M* represents the fraction of internal mass flow rate recycled back to the annulus. At point '2' in Figure 15 the outlet temperature of the internal flow is fed as the boundary condition to the annulus flow.

$$T_{ann_1} = T_{f_N} \tag{48}$$

Similar to the single pass PTC numerical algorithm, all the double pass PTC equations are solved in a segregated manner, solving first the internal flow followed by annulus flow, internal tube, receiver and lastly glass cover. Respective temperature profiles serve as the boundary condition for the solution of the following energy equation.

2.7.2. Numerical Simulations and Results of Double Pass PTC

Various cases are considered for double pass configuration to investigate the pre-mixing effect on the PTC performance. Simulations are executed at different mass flow rates of water, which enters the PTC at 29.5 ^{o}C for all the cases. All simulations are executed until steady state conditions are achieved. Table 7 summarizes the geometrical, optical and material specifications of the double pass collector. Table 8 shows different mass flow rates ($\dot{m}$) and the fractions (*M*) of the recycled fluid to annulus.

Figure 18 shows the variation of the thermal efficiency with mass flow rates. It can be seen from the graph that the increase in the efficiency is not significant with the increase in mass flow rates. Single pass PTC seems efficient in comparison to the above described double pass configuration for all mass flow rates with the used heat transfer coefficients. In the Equation (3), the useful energy q_u is a function of receiver temperature (T_r).The higher the receiver temperature, the higher will be the thermal loss.

Table 7: Geometrical, optical and material specifications of double pass PTC.

Geometrical Specifications	
Receiver length (L)	7.8 m
Collector width (w)	5 m
Tube internal diameter ($\boldsymbol{D_{ti}}$)	0.02245m
Tube external diameter ($\boldsymbol{D_{to}}$)	0.02667m
Receiver internal diameter ($\boldsymbol{D_{ri}}$)	0.066 m
Receiver outside diameter ($\boldsymbol{D_{ro}}$)	0.070 m
Cover internal diameter ($\boldsymbol{D_{ci}}$)	0.109 m
Cover outside diameter ($\boldsymbol{D_{co}}$)	0.115 m
Optical Specifications	
Receiver absorptance ($\boldsymbol{\alpha}$)	0.906
Receiver emittance ($\boldsymbol{\varepsilon_r}$)	0.14
Glass cover transmittance ($\boldsymbol{\tau_c}$)	0.95
Surface reflectivity ($\boldsymbol{\rho_o}$)	0.93
Shape factor (γ)	0.92
Incident angle ($\boldsymbol{\theta}$)	0°
Incidence angle modifier ($\boldsymbol{I_{AM}}$)	1
Material Specifications	
Working fluids	Water
Receiver material	Stainless steel
Glass cover material	Low iron glass

It can be seen from Figure 17 that the average receiver temperature is highest for all the mass flow rates for M = 1, which contributes to the low thermal efficiency. On the other hand, it can also be observed that the average temperature of the receiver decreases with the increase of mass flow rates for all cases (M = 0.5, 1 and single pass).

$$\eta_{th} = \left[\frac{q_u \pi D_{ro} L}{G_n (w - D_{ro}) L}\right] \times 100 \tag{49}$$

Figure 19 shows the outlet temperatures at different mass flow rates of the internal tube and the annulus at steady state condition. The trend of the temperature at the outlet of the internal tube is quite logical since with the increase in the mass flow rates temperature decreases, providing

Table 8: Mass flow rates for double pass PTC.

	***M* = 0.5, 1**
S. No	**Mass flow rates '$\dot{m}$' (kg/s)**
1	0.289
2	0.579
3	0.86
4	1.15
5	1.45

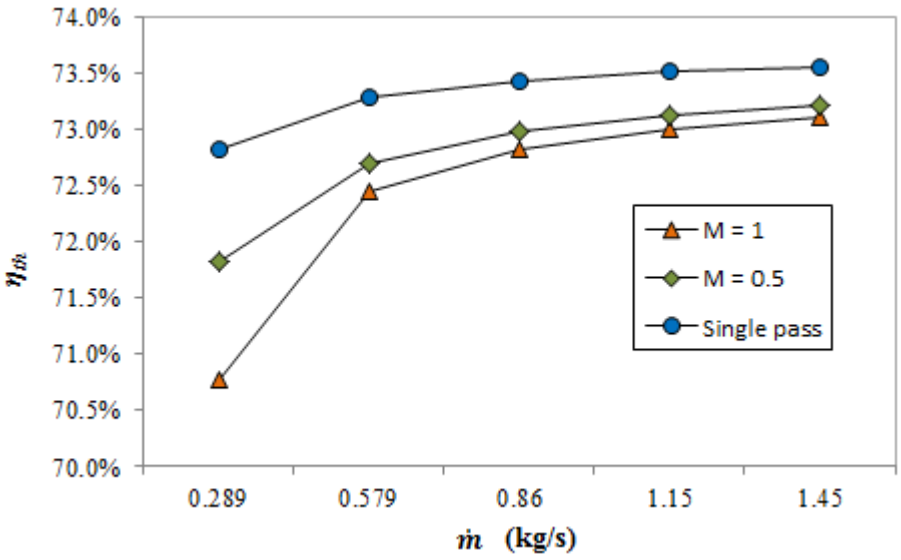

Figure 18: Efficiency of the double/single pass PTC at different mass flow rates.

less time to transfer heat within the PTC (system). It can also be observed that the temperature at the exit of internal tube and annulus increases at higher fraction of mass flow rate in the annulus. There is a significant increase in the temperature at the exit of the internal tube in the double pass configuration as compare to the single pass with similar conditions. Even though the efficiency of double pass is low as compared to the single pass, but the outlet temperature is significantly high as compared to that of single pass PTC.

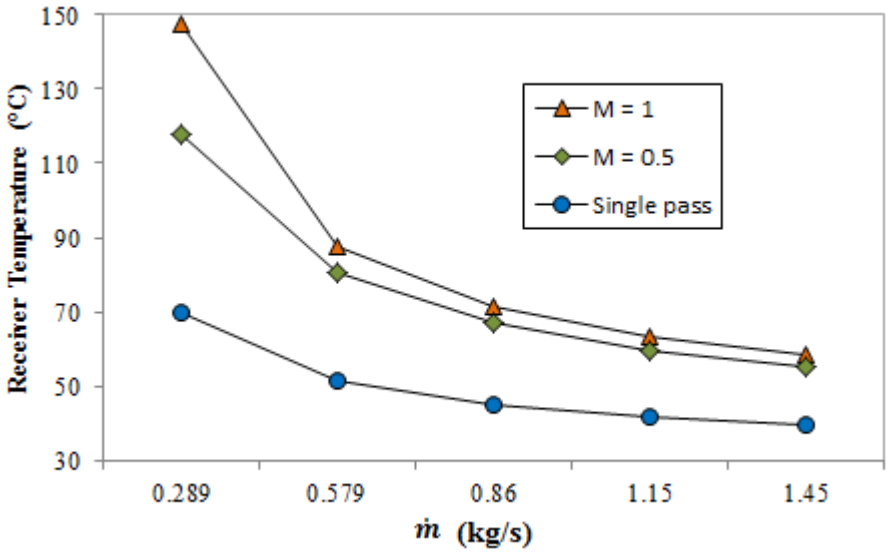

Figure 17: Average receiver temperatures at steady state at different mass flow rates.

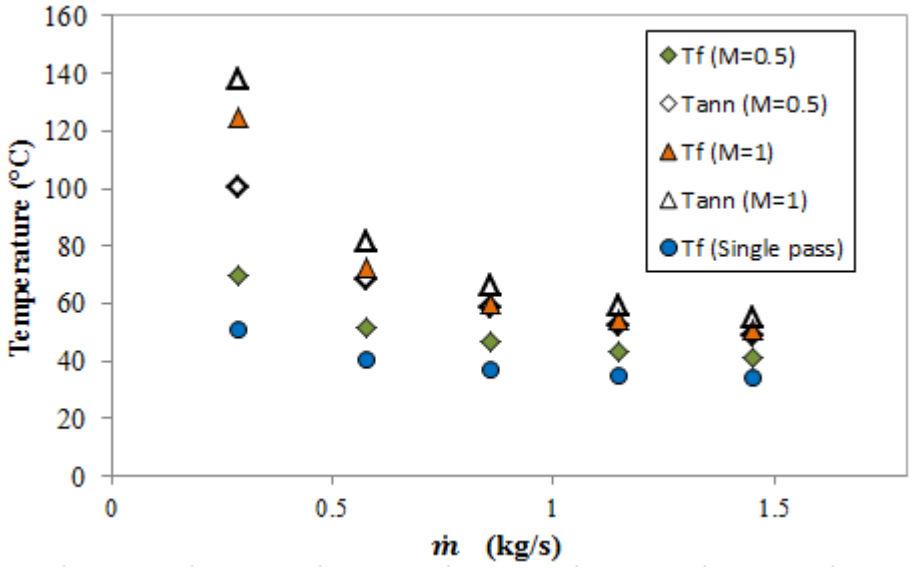

Figure 19: Outlet temperatures of double pass (Internal tube and annulus) and single pass at different mas flow rates at steady state condition.

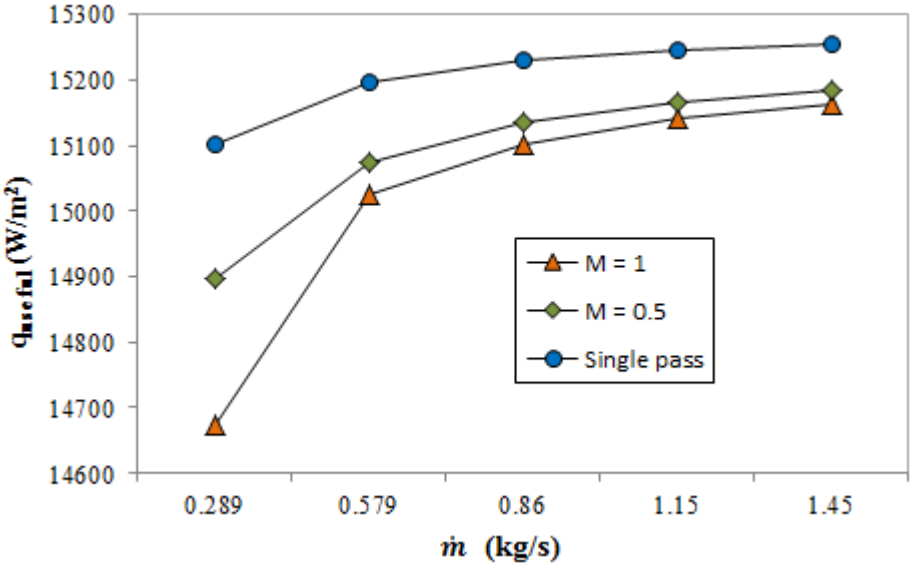

Figure 20: Useful rate of energy absorbed for double/single pass PTC at different mass flow rates

Although there is not a significant difference between the thermal efficiency for different configurations of PTC, but significantly high temperatures can be achieved without sacrificing a significant amount of useful energy. This configuration can reduce the maintenance cost required in the case of vacuumed tube in high temperature PTC applications.

Chapter 3

SYSTEM LEVEL MODELLING

This chapter discusses the modeling of organic Rankine cycle, cooling tower and the integration of the PTC model developed in the previous chapter with ORC and cooling tower models.

3.1. Organic Rankine Cycle Model

ORC is the power generating unit of the solar thermal system which comprises of four major components similar to a conventional Rankine cycle power plant. Evaporator serves as the heat exchanger to transfer the heat from the PTCs to the working fluid (refrigerant), followed by either a turbine or an expander to convert the thermal energy to mechanical work output. Condenser rejects heat followed by a pump to induce refrigerant to flow. Figure 21 shows the schematic of ORC showing different components.

This study follows the transient model of ORC developed by Bamgbopa. M. O et.al [24] which is made compatible for the integration with PTCs and cooling tower models.

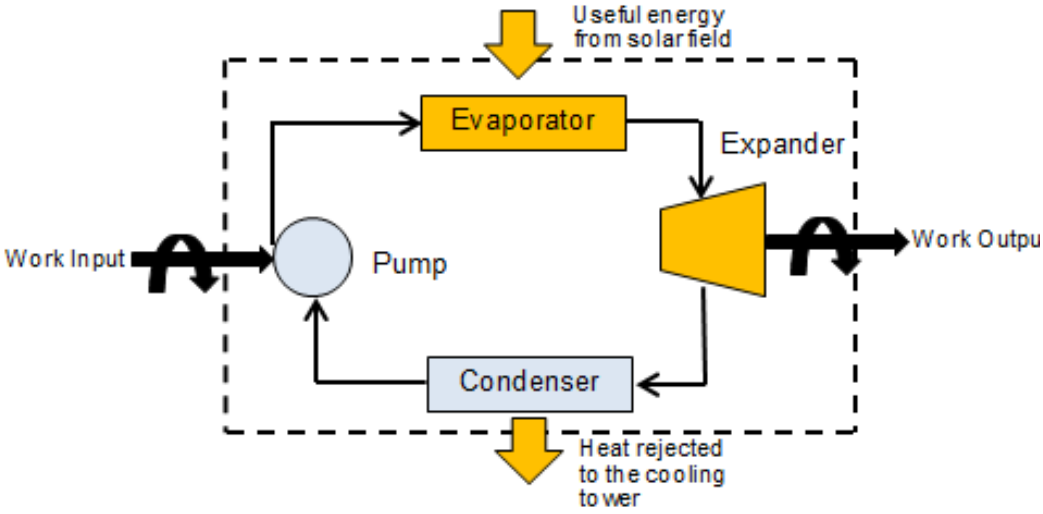

Figure 21: Schematic of the Organic Rankine Cycle (ORC).

3.1.1. Evaporator

Evaporator is numerically modeled as a concentric tube heat exchanger with counter flow. The concentric tube geometric description presented for double pass configuration can be applied to similar counter flow heat exchangers with modifications related to the geometrical parameters and heat transfer coefficients. Evaporator is modeled with transient effects because it is connected to a variable heat source (PTCs).

The evaporator is numerically discretized similar to the PTC to solve the fundamental energy equations across the hot water, refrigerant and evaporator pipe. In this study pressure drop across the evaporator is neglected, the outer tube of the heat exchanger is assumed to be insulated hence no heat transfer from the surroundings is taken into account and the hot water is considered to be in single phase.

Equation (50) represents the energy balance across the control volumes for the refrigerant in the tube;

$$\frac{dE_{ref_i}}{dt} = q_{t,ref} + \dot{m}_{ref_{i-1/2}} h_{ref_{i-1/2}} - \dot{m}_{ref_{i+1/2}} h_{ref_{i+1/2}} \tag{50}$$

where q_t is the convective heat transfer between the evaporator tube and the refrigerant. Unlike the PTC analysis, the equation will be used to solve the enthalpy instead of temperature for handling phase change intrinsically.

$$\frac{dE_{ref_i}}{dt} = \frac{d\left(\rho_{ref} \Delta V_{ref_i} h_{ref_i} - P_{ref_i}/\rho_{ref}\right)}{dt} = \rho_{ref} \Delta V_{ref_i} \frac{dh_{ref_i}}{dt} - \frac{1}{\rho_{ref}} \frac{dP_{ref_i}}{dt} \tag{51}$$

In Equation (51), the pressure term can be neglected for the evaporator. In addition, mass conservation suggests a single mass flow rate, $\dot{m}_{ref}$.

Equation (50) with application of 1st order upwind scheme for the convective terms for a constant mass flow rate takes the following form.

$$h_{ref_i}{}^{t+1} = h_{ref_i}{}^{t} + \frac{\Delta t}{\rho_{ref} \Delta V_{ref}} \left[q_t + \dot{m}_{ref_i} \left(h_{ref_{i-1}}{}^{t+1} - h_{ref_i}{}^{t+1} \right) \right] \tag{52}$$

Rearranging Equation (55) yields:

$$h_{ref_i}{}^{t+1} = \frac{h_{ref_i}{}^{t} + \frac{\Delta t}{\rho_{ref}\Delta V_{ref}}\left[q_{t,ref} + \dot{m}_{ref_i} h_{ref_{i-1}}{}^{t+1}\right]}{1 + \frac{\dot{m}_{ref_i}\Delta t}{\rho_{ref}\Delta V_{ref}}} \tag{53}$$

where $q_{t,ref}$ is the heat exchanged with the heating fluid and characterized by the following expression:

$$q_{t,ref} = H_{c,ref} A_{ref}\left(T_{p,e} - T_{ref}\right) \tag{54}$$

Similarly, the energy balance across the hot water side in the annulus is represented by.

$$\frac{dE_{hw_i}}{dt} = q_{t,hw} + \dot{m}_{hw_{i-1/2}} h_{hw_{i-1/2}} - \dot{m}_{hw_{i+1/2}} h_{hw_{i+1/2}} \tag{55}$$

where h_{hw} is the enthalpy of the hot water, which can be approximated using specific heats as $c_{p_{hw}} T_{hw}$.Using Equation (54), Equation (55) in terms of temperatures is obtained as follows:

$$T_{hw_i}{}^{t+1} = \frac{T_{hw_i}{}^{t} - \frac{\Delta t}{\rho_{hw}\Delta V_{hw} c_{p_{hw}}}\left[q_{t,hw} + \dot{m}_{hw_i} c_{p_{hw}} T_{hw_{i+1}}{}^{t+1}\right]}{1 + \frac{\dot{m}_{hw_i}\Delta t}{\rho_{hw}\Delta V_{hw}}} \tag{56}$$

Convective heat transfer coefficients for refrigerant and hot water (single phase) inside the tube and annulus are calculated with the aid of Gnielinski correlation [34] for turbulent flow ($Re_{ref,hw}$ > 2300). With constant heat flux assumption the heat transfer coefficient and is given by:

$$H_{ref,hw} = \frac{Nu_{ref,hw} k_{ref,hw}}{D_{ch}} \tag{57}$$

$$Nu_{ref,hw} = \frac{(f/8)\left(Re_{ref,hw} - 1000\right) Pr_{ref,hw}}{1 + 12.7\sqrt{(f/8)}\left(Pr_{ref,hw}{}^{2/3} - 1\right)} \tag{58}$$

In the above relations, the subscript *ref* refers to the refrigerant, *hw* refers to the hot water and *ch* represents characteristic dimension. Friction factor f and is evaluated by the following relation.

$$f = \left(1.82 log_{10} Re_{ref,hw} - 1.64\right)^{-2} \tag{59}$$

The $Re_{ref,hw}$ is evaluated with the internal diameter of the evaporator tube as the characteristic length for the refrigerant flow, whereas for hot water hydraulic diameter is used as the characteristic length.

$$Re_{ref,hw} = \frac{\dot{m}_{ref,hw} D_{ch}}{A_{ref,hw} \mu_{ref,hw}} \tag{60}$$

For laminar flow i.e. $Re_{ref,hw} < 2300$, Equation (57) can be modified to yield the following relation:

$$H_{ref,hw} = \frac{4.36\, k_{ref,hw}}{D_{ch}} \tag{61}$$

During the multiphase flow regime of refrigerant Wang-Touber's correlations are used for the evaluation of heat transfer coefficient [36].

$$\alpha_{ref} = 3.4 \left(\frac{1}{X_{tt}}\right)^{0.45} \left(H_{ref}\right)_{liq} \tag{62}$$

$$H_{ref} = \begin{cases} \alpha_{ref}, & 0 \le x \le 0.85 \\ \alpha_{ref}\big|_{x=0.85} - \left(\dfrac{x-0.85}{0.15}\right)^2 \left(\alpha_{ref}\big|_{x=0.85} - \left(H_{ref}\right)_{vap}\right), & 0.85 \le x \le 1 \end{cases} \tag{63}$$

where X_{tt} is the Martinelli factor and convective heat transfer coefficient at single phase $\left(H_{ref}\right)_{liq,vap}$ can be calculated from Equations (57) and (61).

$$X_{tt} = \left(\frac{1-x}{x}\right)^{0.9} \left(\frac{\rho_v}{\rho_l}\right)^{0.5} \left(\frac{\mu_l}{\mu_v}\right)^{0.1} \tag{64}$$

Energy equation is applied across the control volume for the evaporator pipe temperature with constant physical properties.

$$m \frac{du_{p,e}}{dt} = \left(q_{t,hw} - q_{t,ref}\right) + (\dot{q}_e - \dot{q}_w) A_{p,e} \tag{65}$$

$$\begin{aligned} \rho_p \Delta V_p C_{p_p} \frac{{T_{p,e}}_i^{\,t+1} - {T_{p,e}}_i^{\,t}}{\Delta t} &= \left[H_{c,hw}\left({T_{hw}}_i^{\,t} - {T_{p,e}}^{t+1}\right) A_{hw} - H_{c,ref}\left({T_{p,e}}^{t+1} - {T_{ref}}^{t+1}\right) A_{ref}\right] \\ &+ \left[k_p \left(\frac{{T_{p,e_{i+1}}}^{t+1} - {T_{p,e_i}}^{t+1}}{\Delta x}\right) - k_p \left(\frac{{T_{p,e_i}}^{t+1} - {T_{p,e_{i-1}}}^{t+1}}{\Delta x}\right)\right] A_{p,e} \end{aligned} \tag{66}$$

Table 10: Summary of the coefficients for evaporator pipe temperature profile

Nodes	$a_{p,i-1_e}$	$a_{p,i+1_e}$	a_{p,i_e}	b_{p,c_e}
$i = 1$	0	$\frac{k_p A_{p,e}}{\Delta x}$		
$1 < i < n$	$\frac{k_p A_{p,e}}{\Delta x}$	$\frac{k_p A_{p,e}}{\Delta x}$	$\beta_{c,ref} + \beta_{c,hw} + \alpha + a_{p,i+1} + a_{p,i-1}$	$\alpha {T_{p,e}}_i^{\,t} + \beta_{c,ref} {T_{ref,i}}^{t+1} + \beta_{c,hw} {T_{hw}}^{t}$
$i = n$	$\frac{k_p A_{p,e}}{\Delta x}$	0		
$\alpha = \frac{\rho_p \Delta V_p C_{p_p}}{\Delta t}$		$\beta_{c,ref} = H_{c,ref} A_{ref}$		$\beta_{c,hw} = H_{c,hw} A_{hw}$

Equation (67) shows the condensed form of Equation (66), the boundary nodes are dealt with adiabatic condition similar to the PTC's receiver and glass cover.

$$\left(a_{p,i_e}\right) {T_{p,e}}_i^{\,t+1} - \left(a_{p,i-1_e}\right) {T_{p,e_{i-1}}}^{t+1} - \left(a_{p,i+1_e}\right) {T_{p,e_{i+1}}}^{t+1} = b_{p,c} \tag{67}$$

where the coefficients of the variables at different spatial nodes are summarized in Table 10.

Temperature profile of the evaporator pipe at new time steps can be found by the solving *n* number of equations for middle nodes, 1st node and *n*th node simultaneously with the help of matrix inversion. The coefficients in Table 10 form the diagonally dominant matrix presented below.

3.1.2.Condenser

Similar to the evaporator model, condenser is also modeled as a concentric tube heat exchanger with refrigerant flowing in the internal tube and cold water coming from the cooling tower in the annulus. Similar numerical scheme and discretization is carried out to solve the fundamental equations for the refrigerant flow, cold water and condenser pipe temperature. Equations (68), (70) and (71) represent the numerically discretized principle equations for refrigerant, cold water and condenser pipe respectively with the change of direction of heat transfer, i.e. from refrigerant to condenser pipe and condenser pipe to the cold water.

$$h_{ref_i}^{t+1} = \frac{h_{ref_i}^{t} - \frac{\Delta t}{\rho_{ref}\Delta V_{ref}}\left[q_{t,ref} + \dot{m}_{ref_i} h_{ref_{i-1}}^{t+1}\right]}{1 + \frac{\dot{m}_{ref_i}\Delta t}{\rho_{ref}\Delta V_{ref}}} \tag{68}$$

where $q_{t,ref}$ is the convective heat transfer between the refrigerant and condenser pipe, which is represented by:

$$q_{t,ref} = H_{c,ref} A_{ref}\left(T_{ref} - T_{p,c}\right) \tag{69}$$

$$T_{cw_i}^{t+1} = \frac{T_{cw_i}^{t} + \frac{\Delta t}{\rho_{cw}\Delta V_{cw} C_{p_{cw}}}\left[q_{t,cw} + \dot{m}_{cw_i} C_{p_{cw}} T_{hc_{i+1}}^{t+1}\right]}{1 + \frac{\dot{m}_{cw_i}\Delta t}{\rho_{cw}\Delta V_{cw}}} \tag{70}$$

$$\begin{aligned} \rho_p \Delta V_p C_{p_p} \frac{T_{p,c_i}^{t+1} - T_{p,c_i}^{t}}{\Delta t} \\ = \left[H_{c,ref}\left(T_{ref}^{t+1} - T_{p,c}^{t+1}\right) A_{ref} - H_{c,cw}\left(T_{p,c}^{t+1} - T_{cw_i}^{t}\right) A_{cw}\right] \\ + \left[k_p\left(\frac{T_{p,c_{i+1}}^{t+1} - T_{p,c_i}^{t+1}}{\Delta x}\right) - k_c\left(\frac{T_{p,c_i}^{t+1} - T_{p,c_{i-1}}^{t+1}}{\Delta x}\right)\right] A_{p,c} \end{aligned} \tag{71}$$

Single phase heat transfer coefficients are calculated from the same correlation used in the evaporator whereas Chato's correlation [34] is used for the multi-phase regime for *Re* less than 35000, given by:

$$H_{ref} = 0.555\left[\frac{g\rho_l(\rho_l - \rho_v) k_l^{\,3} h_{lv}'}{\mu_l\left(T_{sat} - T_{p,c}\right) D_{p,i}}\right]^{1/4} \tag{72}$$

In the above relation h_{lv}' is the modified latent heat given by [34] ;

$$h_{lv}' = h_v - h_l + 0.375\left(C_{p_l}\right)_{ref}\left(T_{sat} - T_{p,c}\right) \tag{73}$$

The above correlation can be modified for better accuracy by replacing the constant '0.555' in Equation (72)by the following relation [37].

$$\Omega = 0.728\left[\frac{1}{1 + \{(1-x)/x\}(\rho_v/\rho_l)^{2/3}}\right]^{3/4} \tag{74}$$

For *Re* > 35000, Boyko and Kruzhilin correlation is used given by[38];

$$H_{ref} = \left(\frac{k_l}{D_{p,i}}\right) 0.021 {Re_l}^{0.8} {Pr_l}^{0.43} \left[1 + x\left(\frac{\rho_l}{\rho_v} - 1\right)\right]^{1/2} \tag{75}$$

Equation (71) can be condensed as;

$$\left(a_{p,i_c}\right) {T_{p,c_i}}^{t+1} - \left(a_{p,i-1_c}\right) {T_{p,c_{i-1}}}^{t+1} - \left(a_{p,i+1_c}\right) {T_{p,c_{i+1}}}^{t+1} = b_{p,c} \tag{76}$$

Table 11 summarizes the coefficients in the Equation (76).

Table 11: Summary of the coefficients for condenser pipe temperature profile

Nodes	$a_{p,i-1_c}$	$a_{p,i+1_c}$	a_{p,i_c}	b_{p,c_c}
$i = 1$	0	$\frac{k_p A_{p,c}}{\Delta x}$		
$1 < i < n$	$\frac{k_p A_{p,c}}{\Delta x}$	$\frac{k_p A_{p,c}}{\Delta x}$	$\beta_{c,ref} + \beta_{c,cw} + \alpha + a_{p,i+1} + a_{p,i-1}$	$\alpha {T_{p,c_i}}^{t} + \beta_{c,ref} {T_{ref,i}}^{t+1} + \beta_{c,w} {T_{cw}}^{t}$
$i = n$	$\frac{k_p A_{p,c}}{\Delta x}$	0		
$\alpha = \frac{\rho_p \Delta V_p C_{p_p}}{\Delta t}$		$\beta_{c,ref} = H_{c,ref} A_{ref}$		$\beta_{c,cw} = H_{c,cw} A_{cw}$

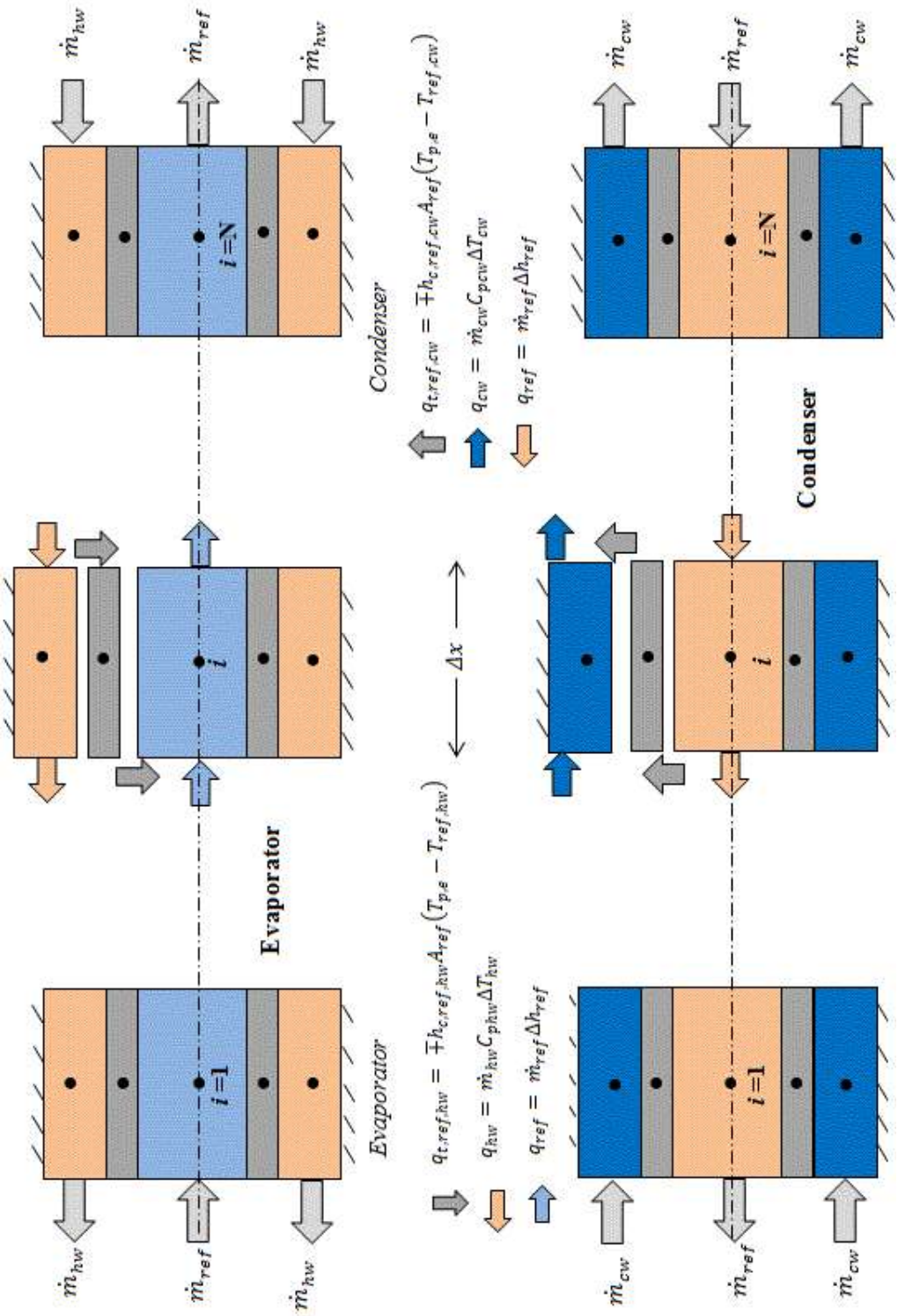

Figure 22: Numerical domain for evaporator and condenser

3.1.3.Numerical Algorithm for Evaporator and Condenser

In order to solve the above discretized equations for evaporator and condenser, following assumptions are made.

1. Uniform flow for all fluids while incompressible flow for hot and cold water.
2. Both evaporator and condenser are well insulated.
3. Material properties of evaporator/condenser tube are considered as constant for the working temperature range.

Similar to the PTC, the discretized equations for both evaporator and condenser are solved in a segregated manner. An initial constant enthalpy of the refrigerant is distributed along the domain of the internal tube for both heat exchangers. The enthalpy at new time (t+1) is calculated by marching in time as well as domain with the aid of old enthalpy and new enthalpy value of the previous node. The initial temperature distribution of the tube serves as the boundary condition. The heat transfer coefficient is calculated at each node of the computational domain using relevant coefficients (single or multi-phase).

The temperatures of the refrigerant at each node and time are evaluated at the working pressures and calculated enthalpies for both the heat exchangers. The new refrigerant temperature at the new time step and old water temperature along with the heat transfer coefficients are used for calculating the temperature distribution of the tubes in the heat exchangers. The tube's temperature distribution serves as the boundary condition to solve the discretized energy equation for the annulus flow of water in the counter flow direction. The rate of heat transfer from the refrigerant is calculated by the following equations for both the heat exchangers.

$$q_{evap} = \dot{m}_{hw}\rho_{hw}\Delta T_{hw}{}^{t+1} \tag{77}$$

$$q_{cond} = \dot{m}_{cw}\rho_{cw}\Delta T_{cw}{}^{t+1} \tag{78}$$

Transient models of evaporator and condenser are compared with the steady state results of [39]. The optimum conditions presented in [39] are taken as the design parameters to calculate the area of the heat exchangers to get the outlet temperatures. The summary of the design parameters are presented in Table 12.

Table 12: Summary of the design parameters for steady state analysis [39].

Evaporator	D_i = 10 mm	D_o = 16 mm
Condenser	D_i = 7 mm	D_o = 10 mm
Refrigerant		R245fa
Hot water inlet temperature ($T_{hw,i}$)		90 °C
Cooling water inlet temperature ($T_{cw,i}$)		20 °C
Pinch point temperature for both HXs (ΔT_p)		5 °C
Evaporator pressure		870 kPa
Condenser pressure		160 kPa
Hot water outlet temperature ($T_{hw,o}$)		88.5 °C
Cooling water outlet temperature ($T_{cw,o}$)		21.5 °C
Evaporator outlet quality (x_e)		1
Condenser inlet quality (x_c)		>0.97

The flow regime in the evaporator transits from single phase to multi-phase along the length and one can visualize the evaporator virtually divided into two heat exchangers. The length of each heat exchanger is evaluated by the application of LMTD and relevant heat transfer coefficients. It is assumed that the refrigerant leaves the condenser at saturated liquid state (x = 0) from the inlet quality of 0.99. Equations (72) and (75) are used to evaluate the heat transfer coefficients. Table 13 summarizes the outcome of steady state analysis. Figure 23 shows the pictorial representation of the design conditions for evaporator and condenser. The *x-axis* of the figure depicts the states at the inlet and exit of the 'virtual heat exchangers'. The *Left* figure represents the division of evaporator into two heat exchangers (single and multi-phase) whereas *Right* shows the single heat exchanger depiction of condenser with L as the total heat exchanger length.

Table 13: Steady state analysis for evaporator/condenser models.

mass flow rate of the hot water	1 kg/s
mass flow rate of the refrigerant	0.0301 kg/s
mass flow rate of the cooling water	0.89 kg/s

Length of the Evaporator	12 m
Length of the Condenser	74 m
Evaporator outlet quality (x_e)	1
Condenser outlet quality (x_c)	0
Hot water outlet temperature ($T_{hw,o}$)	88.5°C
Cooling water outlet temperature ($T_{cw,o}$)	21.5 °C

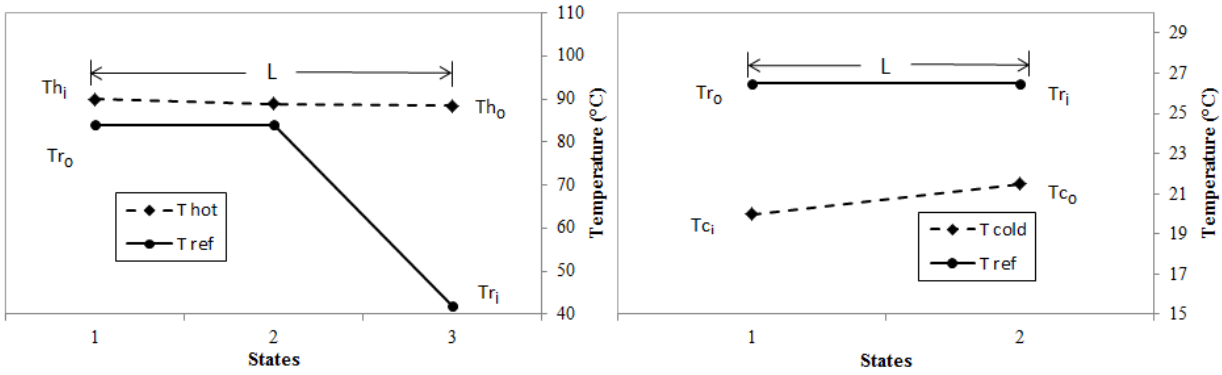

Figure 23: (Right) Condenser design conditions (Temperature), (Left) Evaporator design conditions (Temperature).

Evaporator and condenser models are simulated with the above mentioned details with adequate time to achieve steady state. Figure 24 shows the transients of refrigerant enthalpy and temperature in evaporator and condenser, which depicts steadiness of the system. Figure 25 shows the steadiness of the exit temperatures at the exit of evaporator and condenser during the simulation. The results of the numerical model at steady state show good comparison with the steady state results at design conditions, tabulated above. The outlet temperature of the hot water drops from 90 °C to 88.52 °C with the exit quality of the refrigerant equals to unity at the operating pressure of 870 kPa in the evaporator. In the condenser, the exit temperature of cooling water is found to be 21.14 °C which increased from 20 °C at the inlet. Moreover, the refrigerant exited with a quality of '0.2' from the inlet quality of '0.99' transferring 134.6 kJ/kg of energy to the cooling water. The viable reason of this difference of exit states between the steady state condenser and the numerical model is due to the calculation of the heat transfer coefficient for refrigerant in the condenser. In the steady state calculation, an average heat transfer coefficient for the refrigerant is calculated unlikely to the numerical model. The results

of the numerical model at steady state are graphically summarized in Figure 26 for evaporator and condenser.

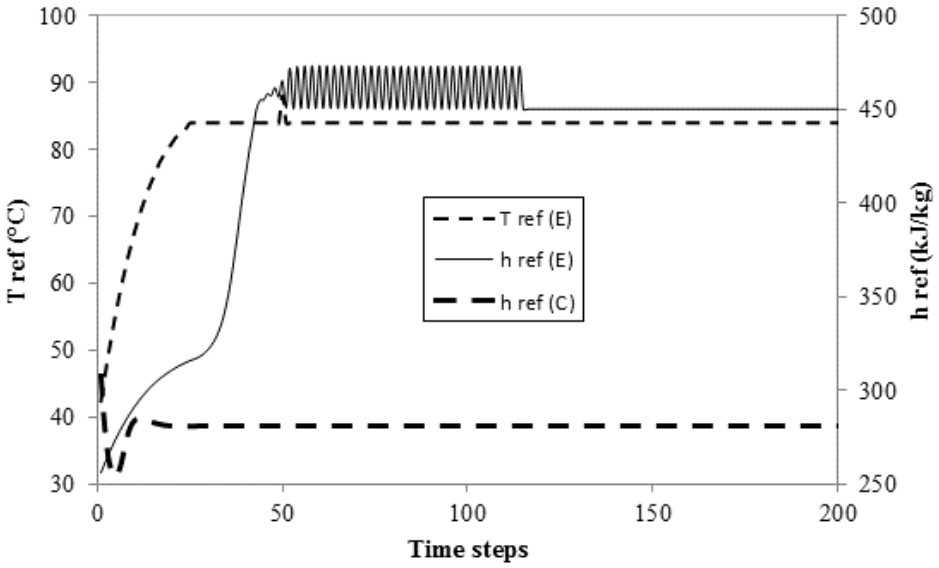

Figure 24: Transients of refrigerant temperature and enthalpies at the exit nodes (Evaporator (E)/Condenser(C))

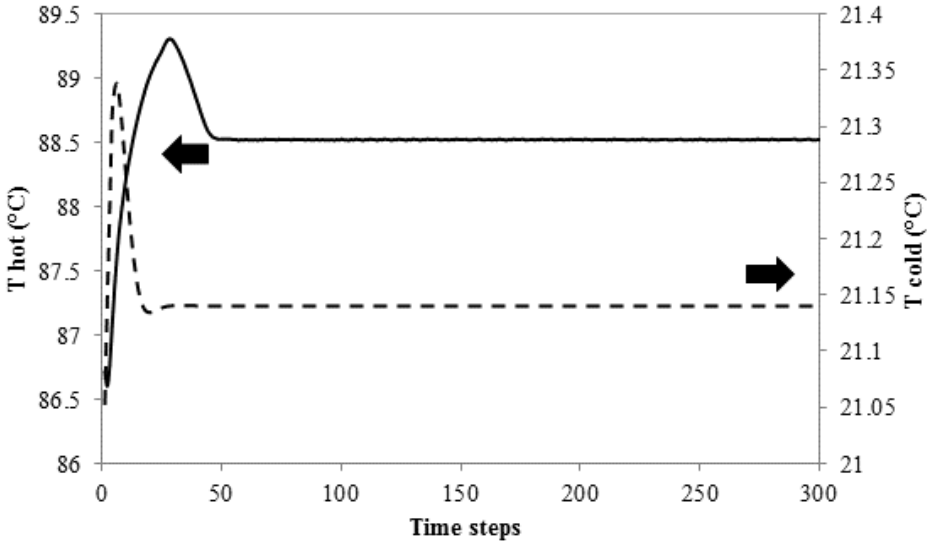

Figure 25: Transients of hot/cold water temperatures at the exit nodes

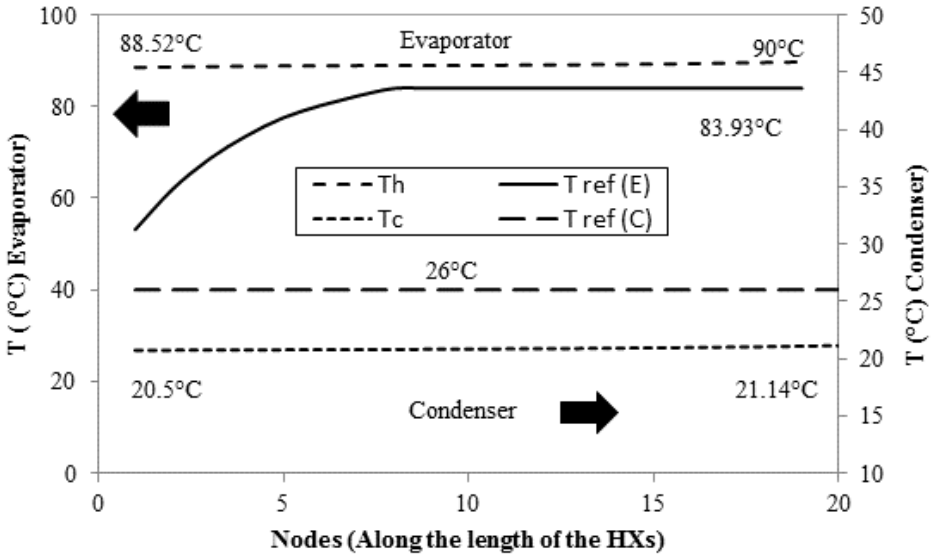

Figure 26: Graphical summary of the results at steady state (Evaporator (E)/Condenser(C))

3.1.4.Pump

The pump is modeled with steady state assumption with a black box approach. Figure 27 shows the input and the output parameters of the pump model.

Performance (head vs. flow rate) curves are used to derive a mathematical relation between the head rise in the pump and the flow rates. A second order polynomial of a characteristic curve is fitted to relate the pressure rise and mass flow rate of the system.

$$Head\ rise = c_1\dot{v}^2 + c_2\dot{v} + c_3 \tag{79}$$

Inlet temperature to the pump is used to calculate the inlet enthalpy and refrigerant density. With the aid of physical properties the above equation can be modified to relate the pressure rise and the system mass flow rate.

$$\Delta P = [c_1\dot{v}^2 + c_2\dot{v} + c_3]\rho_{ref}g \tag{80}$$

The hydraulic efficiency is determined from the following relation;

$$\eta_{pump} = a_1\dot{v}^2 + a_2\dot{v} + a_3 \tag{81}$$

And the power consumed by the pump is calculated from;

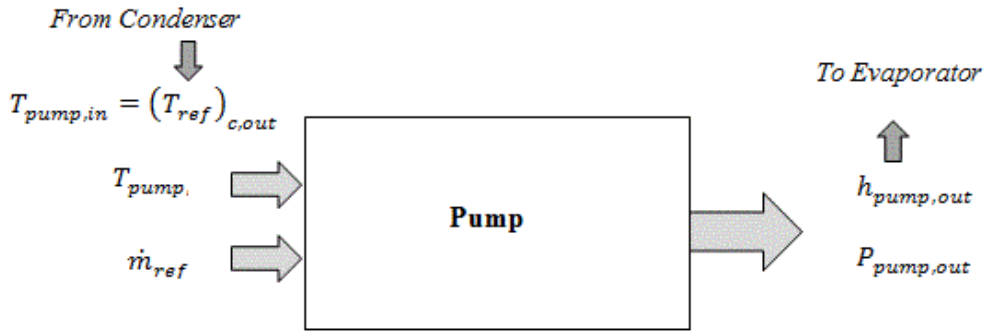

Figure 27: Black box representation of the pump.

$$Wpump = \frac{\dot{m}\Delta P}{\rho_{ref}\eta_{pump}} \tag{82}$$

The constants in the Equations (80) and (81) are presented in Table 14 where the volumetric flow rate ($\dot{v}$) is calculated in m^3/h.

Table 14: Regression constants for pump.

	a	c
1	-0.019274	-0.4664
2	0.2101	-1.1358
3	0.01927	54.8425

3.1.5.Expander

Similar to the pump model, expander is also modeled with steady state, isentropic assumption. The black box representation is presented in **Error! Reference source not found.**.

Curve is fitted to a series of pressure ratios ($r_p = {}^{P_{in}}/_{P_{out}}$) and expander efficiency to interpolate the desired efficiency. The detail of the pressure ratios and efficiency is supplied in the appendix. The power output of the expander is calculated by;

$$W_{turbine} = \eta_{expander}\left(h_{turbine,in} - h_s\right) \tag{83}$$

In the above equation the 'h_s' represents the enthalpy at the exit of the isentropic process.

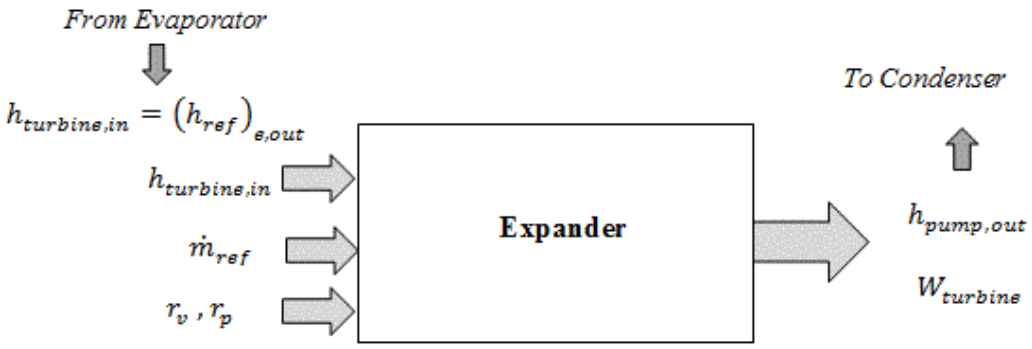

Figure 28: Black box representation of the expander.

3.2. Cooling Tower Model

Cooling tower is modeled considering constant cooling tower efficiency. The cooling tower efficiency is defined as the ratio of difference of inlet and outlet water temperature to the inlet and wet bulb temperature. Since the wet cooling tower utilizes evaporative cooling hence the performance is limited by the wet bulb temperature of the ambient air. As shown in Figure 29, the model uses inlet water temperature (from the exit of the condenser) and wet bulb temperature to produce the outlet temperature (to the condenser inlet). A nominal efficiency of 72% is selected for this study.

$$T_{ct,out} = T_{ct,in} - \eta_{CT}\left(T_{ct,in} - T_{wb}\right) \tag{84}$$

In Figure 29, $T_{ct,in}$ represents the inlet temperature to the cooling tower coming from condenser, and T_{wb}represent the wet bulb temperature.

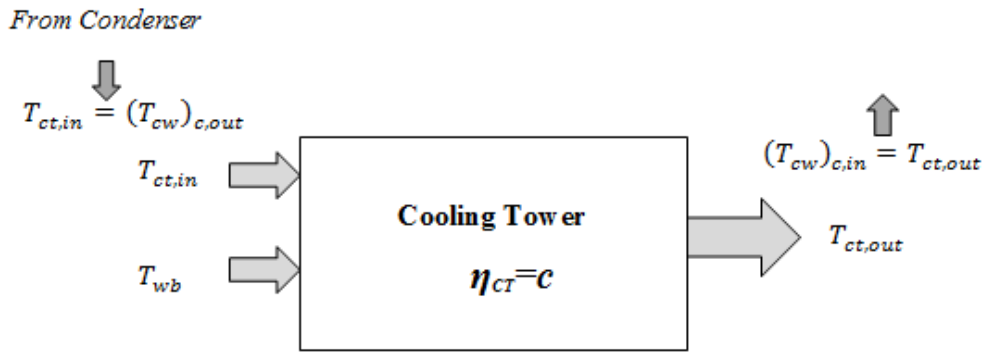

Figure 29: Black box representation of the wet cooling tower.

3.3. System Integration

The numerical models of solar resource, parabolic trough collector (PTC), organic Rankine cycle (ORC) and cooling tower are integrated together to run system level simulations. The solar resources are calculated for entire course of the day and served as the varying boundary conditions to the PTC model. The working fluid (water) in the PTC served as the heat source in the evaporator with refrigerant R245fa as the working fluid in the ORC loop. The condenser of the ORC is connected to a wet cooling tower where water is cooling the refrigerant expanded in the expander.

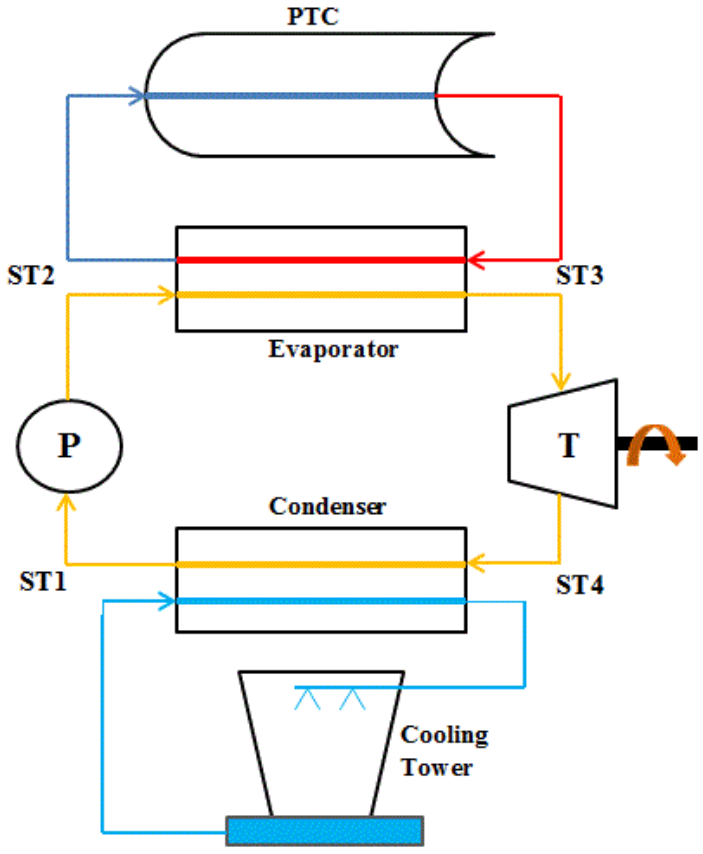

Figure 30: Schematic of integrated sub-systems (PTC, ORC and cooling tower)

Figure 30 shows the detail schematic of the integrated system with three different working loops of PTC-evaporator, ORC and condenser-cooling tower. In Figure 30, *ST* refers to the states at the inlet of different components of the system. Detail of each state is as follows:

ST1 refers to the inlet conditions to the pump and condenser. The cooled refrigerant enters the pump as the saturated liquid. The pressure of the condenser (P1) is regulated during the simulation in order to saturate the refrigerant in the condenser and complete the thermodynamic cycle, which refers to 'zero' quality at the inlet of the pump. The condenser is fed with the cooling water at the exit temperature of the cooling tower to cool down the refrigerant.

At **ST2** the refrigerant enters the evaporator at the exit enthalpy and pressure of pump (P2), whereas the hot water exits the evaporator and fed back to the PTC loop, where it again energizes to serve as the evaporator inlet at ST3.

At **ST3** the heated refrigerant exits the evaporator and enters the expander at P2 (neglecting pressure losses in the evaporator) and exit evaporator enthalpy, whereas the hot water enters the evaporator at the exit temperature of the PTC.

At **ST4** the expanded refrigerant enters the condenser after passing through the expander at P1. The expander exit refrigerant enthalpy serves at the boundary condition to the condenser. Whereas the cooling waters leaves the condenser and enters in the cooling tower to get cooled.

Chapter 4

RESULTS AND DISCUSSION

This chapter includes validation of the developed numerical models of PTC (single pass), ORC and cooling tower. The integrated model is used to investigate the performance of the overall system under various conditions.

4.1. ORC analysis

The developed components of the ORC (evaporator, condenser, pump and expander) are integrated without the heat source (PTC) and cooling tower. It is essential to validate the integrated ORC model with the steady state results. Design conditions of [40] are considered for validation. They used a typical case of heat recovery system in which the water is used as the heat source from a geothermal reservoir. Refrigerant R245fa is used as the working fluid in the ORC.

The hot water enters the ORC (evaporator) at 100°C from the heat source. The evaporator pinch point temperature is set as 5°C. They assumed a cooling tower which supplies cooling water at 21°C to the condenser and experienced a 9°C temperature rise. The condenser pinch point temperature is taken as 4°C. The pinch point temperature is defined as the minimum temperature difference between the two fluid streams incurring heat transfer. The design

Table 15: Design parameters for ORC [40].

Refrigerant	R245fa
Hot water inlet temperature ($T_{hw,i}$)	100 °C
Cooling water inlet temperature ($T_{cw,i}$)	21 °C
Pinch point temperature for both evaporator $(\Delta T_p)_e$	5 °C
Pinch point temperature for both condenser $(\Delta T_p)_c$	4 °C
Expander inlet quality (x_e)	0.8
Expander outlet quality (x_c)	0.9
Power output	25kW

conditions resulted in producing 25kW of power output when the refrigerant enters the expander with 80% quality at 75°C and leaves expander at 90% wet vapor at 34°C. Design parameters are tabulated in Table 15.

Mass flow rates and the areas of the evaporator and condenser are calculated with the help of design parameters and relevant heat transfer coefficients for condenser and evaporator. Table 16 summarizes the area and mass flow rates of the system.

The transient ORC model is considered with the above mentioned hot and cold inlet temperatures as the initial and boundary conditions. The ORC model is simulated for an adequate time to achieve steady state conditions. The thermodynamic cycle is controlled with a pseudo strategy at the low pressure side (condenser). The pressure of the condenser is modified and altered during the simulation in order to complete the thermodynamic cycle and saturates the refrigerant from the condenser ($x = 0$, here x is the outlet quality of the refrigerant).

Table 16: Areas and mass flow rates for design conditions.

Geometrical Specifications	
Length of evaporator (L_e)	30 m
Length of condenser (L_c)	38 m
Outside diameter (D_o)	10.2×10^{-3} m
Inside diameter (D_i)	9.8×10^{-3} m
Annulus diameter (D)	16×10^{-3} m
Mass flow rates	
Hot water mass flow rate ($\dot{m}_h$)	2.64 kg/s
Refrigerant mass flow rate	1.789 kg/s
Cold water mass flow rate ($\dot{m}_c$)	7.95 kg/s

Figure 31 shows the transient behavior of the water temperatures at the exit of the evaporator (Thout) and condenser (Tcout) for the simulation. It is evident from the figure that the temperatures reach steady state and stabilizes after 50 time steps ($\Delta t = 0.5$ seconds). The hot water outlet temperatures decreased to 70.6°C while the cold water increased to 30°C from 21°C. At the steady state the refrigerant enters the expander at 80% and leaves at 89.6% dry refrigerant respectively. The refrigerant enters the expander at 74.98°C and leaves it at 34°C producing a net power output of 23.92 kW with an efficiency of 7.3%.

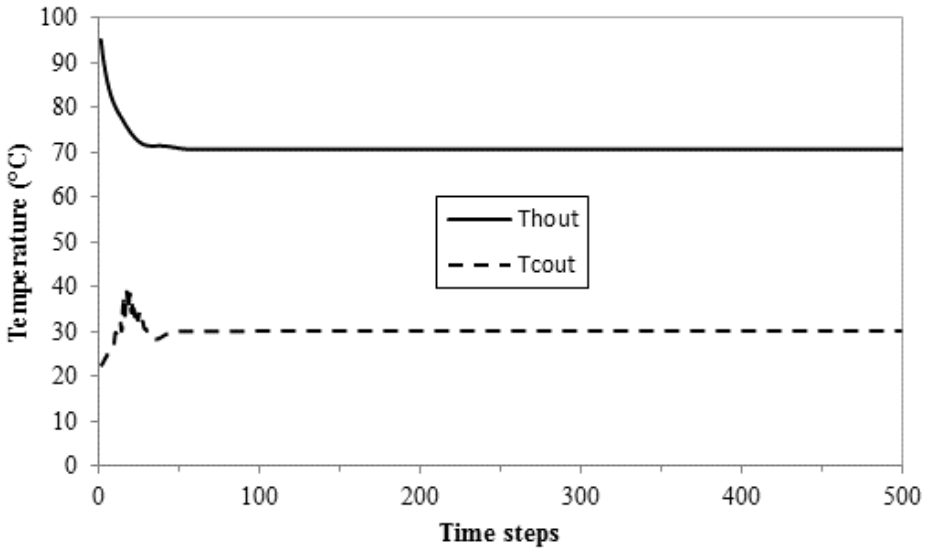

Figure 31: Transients of temperature of water at the outlet of evaporator and condenser.

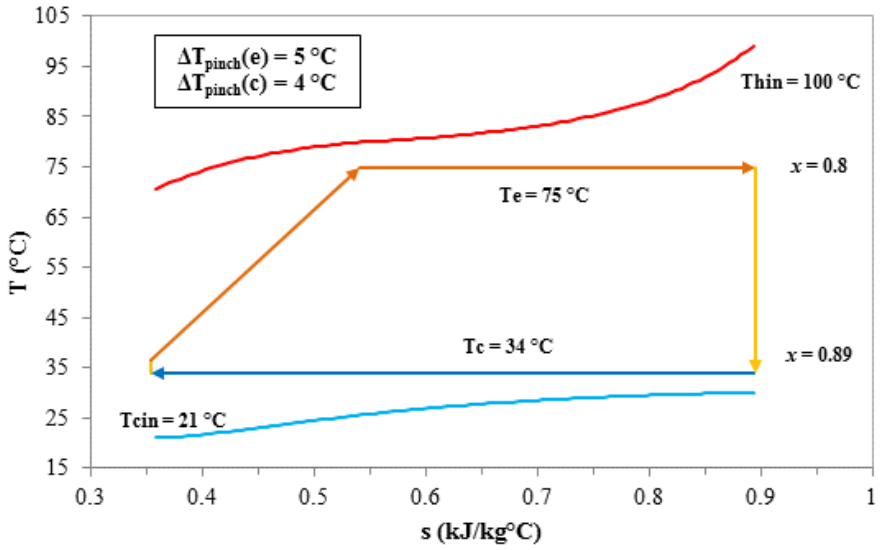

Figure 32: Temperature-entropy diagram of the ORC for the design case simulation at steady state.

Figure 32 summarizes the outcome of the simulations at steady state using a T-s (temperature-entropy) diagram for the validation case and shows good agreement with the design case result presented in the [40]. It can be deduced that the adopted approach for the integration of different ORC components and the pseudo control strategy can applied to different off design conditions with a level of confidence.

Secondly, various hot water inlet temperatures and refrigerant mass flow rates are investigated to characterize the selected ORC at steady state. The pseudo control strategy is again applied to control the condenser pressure to saturate the refrigerant at the exit of the condenser and complete the thermodynamic cycle.

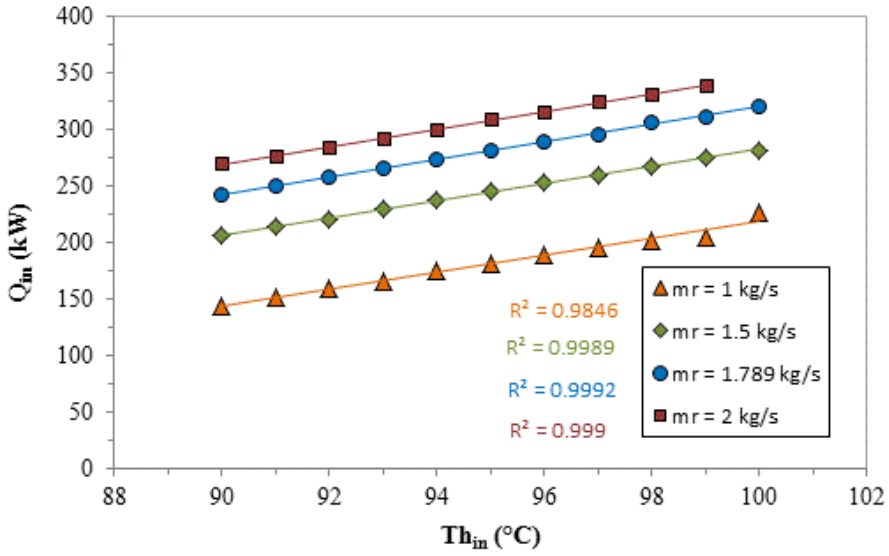

Figure 33: Trend of rate of thermal energy to the ORC with the hot water inlet temperatures and refrigerant mass flow rates.

Figure 33 shows the trend of rate of thermal energy into the evaporator with the incoming hot water temperatures at various refrigerant mass flow rates. It is clear from the figure that as the hot water inlet temperature increases the heat transfer between the refrigerant also increases. In addition to the hot water temperature, increasing the mass flow rate of the refrigerant an increase in the rate of thermal energy input into the system.

Figure 34 shows the net power output at various temperatures and refrigerant mass flow rates. Increasing trend of net power is steeper as compared to the thermal power input. The main reason of this trend change is due the expander model as it is highly dependent on the pressure difference between the evaporator (high pressure side) and the condenser (low pressures side). The imposed pressure control strategy causes the fluctuations in the net power output at different pairs of temperature and refrigerant. A more refined and sophisticated control strategy can be adapted to remove the irregularities. However, an increasing trend of the net power with

the hot water temperatures and refrigerant mass flow rates is qualitatively and quite reasonably quantitatively depicts the relationship between the plotted parameters.

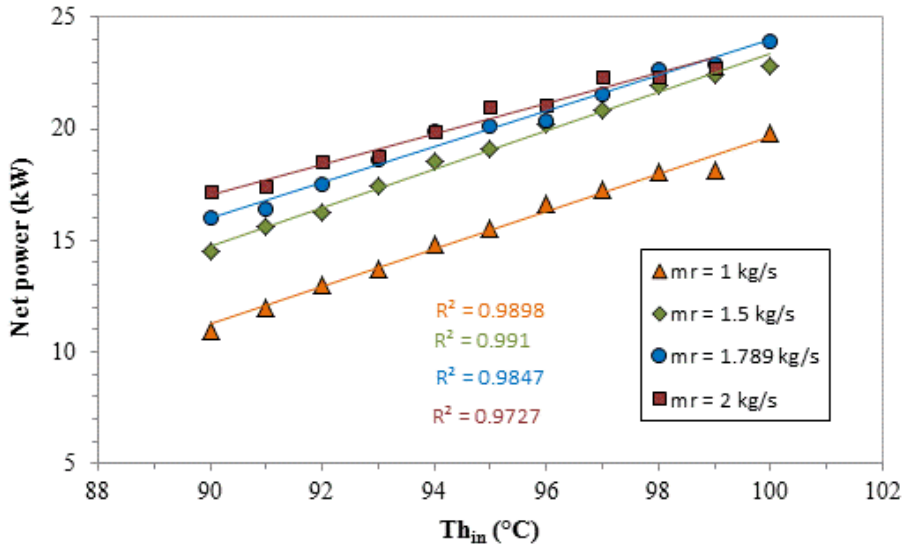

Figure 34: Trend of net power output from ORC with the hot water inlet temperatures and refrigerant mass flow rates.

Table 17: Net power output of ORC at various refrigerant mass flow rates and hot water inlet temperatures.

	Net power (kW)			
Th_{in}(°C)	**mr = 1.789 kg/s**	**mr = 1 kg/s**	**mr = 1.5 kg/s**	**mr = 2 kg/s**
90	15.97	10.93	14.48	17.18
91	16.38	11.97	15.63	17.39
92	17.51	13.04	16.25	18.51
93	18.66	13.74	17.41	18.76
94	19.87	14.84	18.56	19.86
95	20.14	15.50	19.12	21.01
96	20.36	16.62	20.22	21.09
97	21.55	17.26	20.81	22.36
98	22.65	18.04	21.90	22.31
99	22.90	18.12	22.39	22.77
100	23.92	19.77	22.82	

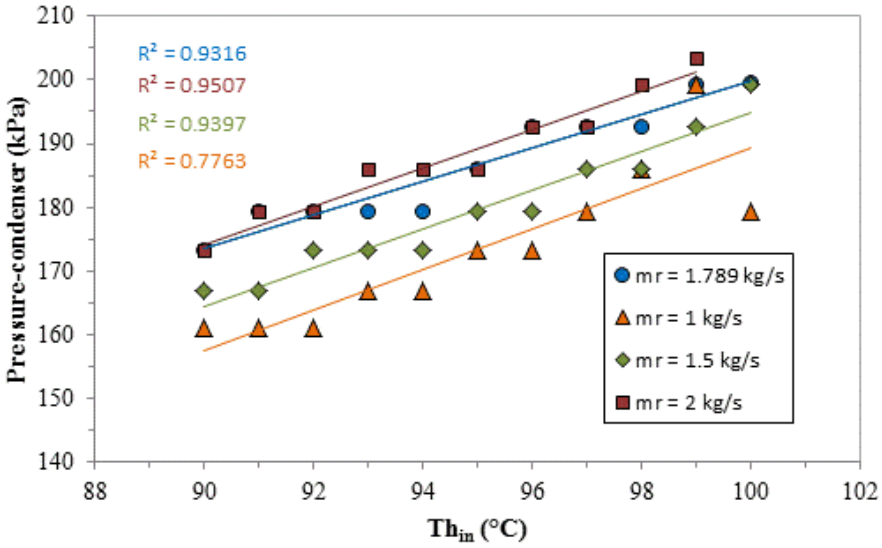

Figure 35: Variation of condenser pressure with hot water inlet temperatures and refrigerant mass flow rates.

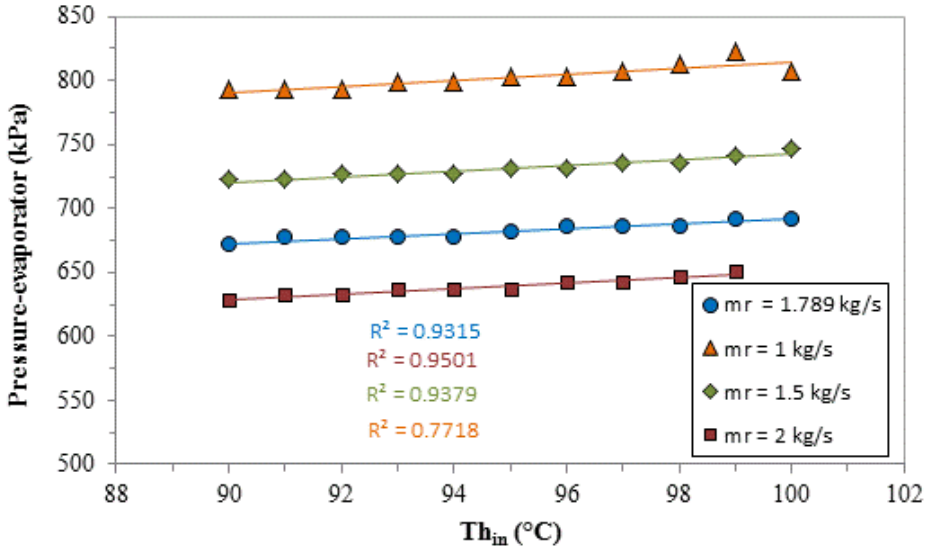

Figure 36: Variation of evaporator pressure with hot water inlet temperatures and refrigerant mass flow rates.

The variations of the condenser and evaporator pressures can be seen in the Figure 35 and Figure 36. It is evident from the figure that with higher mas flow rates and inlet temperature the condenser saturates the refrigerant at higher working pressures. The fluctuations in pressure for the sets of condition are due to the coarse shifting of pressure, pressure is modified with 1°C of

the saturation temperature at the condenser. In the evaporator, the pressure variations are insignificant for different hot water temperatures for a particular refrigerant mass flow rate. It is clear from the figure that as the mass flow rate increases the evaporator pressure also increases which directly depends upon the low pressure side of the ORC cycle.

4.2. PTC, ORC and cooling tower

Parabolic trough collectors are integrated with ORC and cooling tower. The areas calculated in the design case mentioned in the previous section are considered for evaporator and condenser. The PTC and ORC are fed with a profile of varying solar input and ambient temperature for a whole course of the day. Three representative days of the year are selected for the simulation.

4.2.1.Solar resources and area of the PTC

Solar resources are determined for the location of Larnaca (34°55′N 33°38′E) at sea level (altitude = 0 m) for some representative days of the year. The numerical detail of the calculations are discussed in the previous chapter. Figure 37 shows the daily solar irradiance (DNI) for 4 representative days of the year (equinoxes and summer-winter solistices) calcuated at an interval of 5 mins through out the course of the days.

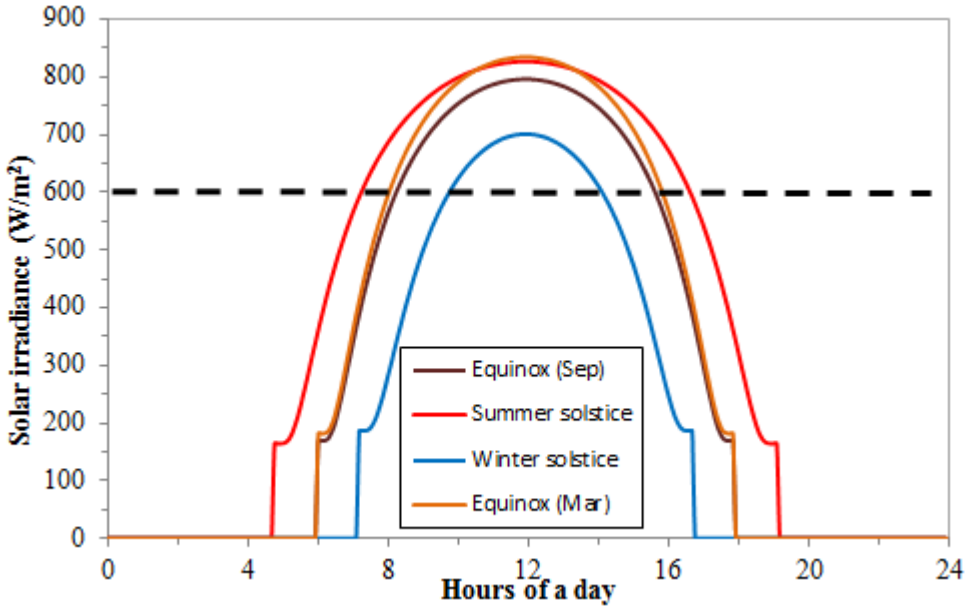

Figure 37: Daily solar irradiance for representative days of a year.

In the Figure 37, slight difference in the two equinoxes can be seen, this difference is due to the 'clear sky' model discussed previously. Although the length of these two days are similar in a year, but the seasonal consideration of the model incurred this slight difference in the peak values for these two representative days.

The sizing of the single pass PTC system is done on the basis of a single design value. The area of the PTC is calculated to produce 340 kW of power from a nominal solar irradiance of 600 W/m^2. Inorder to calculate the desired area of PTC (single pass), following specifications (Table 18) are considered as constant whereas length of the PTC is the only variable. From the design conditions, the area required is calculated from Equation (85).

$$A_{PTC} = \frac{Desired\ power}{Solar\ irradiance} \tag{85}$$

Which comes out to be ~ 566 m^2, with a total length of ~ 327.5 m ($L = \frac{A_{PTC}}{w - D_{ro}}$).

Table 18: PTC design parameters.

Geometrical Specifications	
Collector width (w)	1.8 m
Receiver internal diameter	0.066 m
Receiver outside diameter	0.070 m
Cover internal diameter ($\boldsymbol{D_{ci}}$)	0.109 m
Cover outside diameter ($\boldsymbol{D_{co}}$)	0.115 m
Optical Specifications	
Receiver absorptance ($\boldsymbol{\alpha}$)	0.906
Receiver emittance ($\boldsymbol{\varepsilon_r}$)	0.14
Glass cover transmittance ($\boldsymbol{\tau_c}$)	0.95
Surface reflectivity ($\boldsymbol{\rho_o}$)	0.93
Shape factor (γ)	0.92
Incident angle ($\boldsymbol{\theta}$)	0°
Incidence angle modifier ($\boldsymbol{I_{AM}}$)	1
Material Specifications	
Receiver material	Stainless steel
Glass cover material	Low iron glass
Design solar irradiance and power	
Solar irradiance	600W/m^2
Desired power	340 kW

Figure 38 presents a schematic of the PTCs configuration, where the 'left' shows the parallel configuration where the mass flow rate and total length is equally divided among the PTC rows. Whereas 'right' one shows series configuration with the calculated length and mass flow rate. In this analysis parallel configuration is used for the analysis.

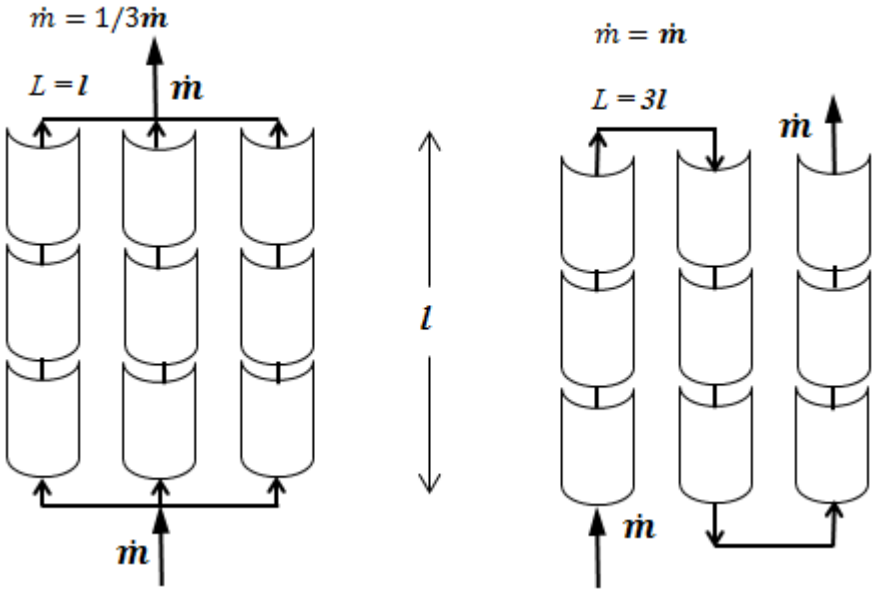

Figure 38: (Left) PTC single pass parallel configuration (Right) PTC single pass series configuration

4.2.2.Pressure drop

Pressure drop is calculated for the PTC with an assumption of internal flow in a straight pipe (neglecting joints and bends) to have an order of the magnitude idea of the power requirement in the PTC loop. Classical formulae are used to evaluate the pressure drop and power requirement along the PTC pipe system. Incompressible, fully developed turbulent and steady flow regime at a fixed temperature inside the pipe is considered. The Bernoulli's head loss and pressure drop can be written as the function of Fanning friction factor 'f '. Zigrang-Sylvester equation is used to evaluate the friction factor, where ε is the surface roughness of the pipe material.

$$\frac{1}{\sqrt{f}} = -4\,log_{10}\left[\frac{\varepsilon/D_{ri}}{3.7} - \frac{5.02}{Re}\,log_{10}\left(\frac{\varepsilon/D_{ri}}{3.7} + \frac{12}{Re}\right)\right] \tag{86}$$

$$\Delta P = 2f\left(\frac{L}{D_{ri}}\right)(\rho V^2) \tag{87}$$

$$Power = \Delta PQ \; [Q = \text{flow rate } (m^3/s)] \; (kW)$$

Figure 39 shows the trend of pressure loss across the PTC at different mass flow rates, which logical replicates the pressure drop relation, as the velocity increases so as the pressure drop.

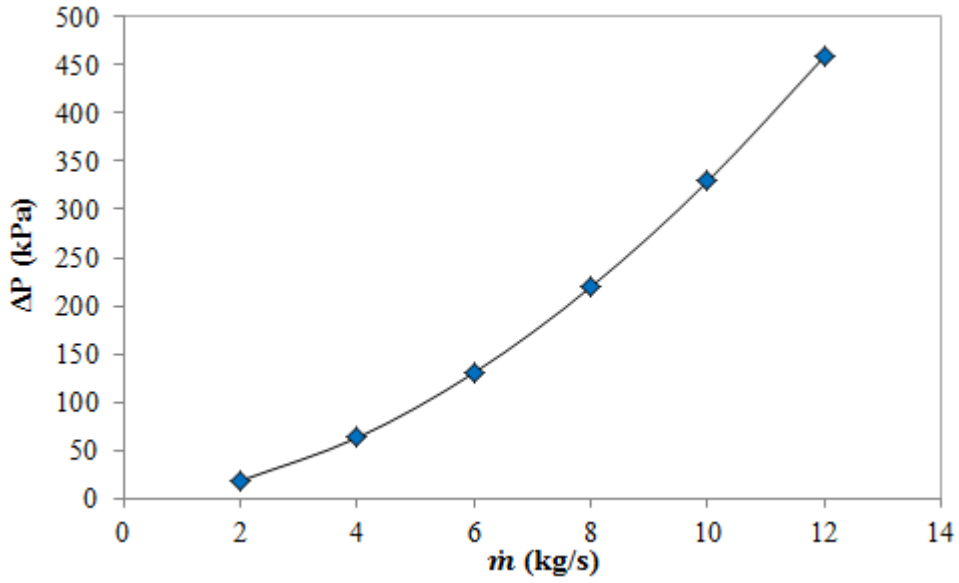

Figure 39: Pressure drop in single pass PTC at different mass flow rates.

4.2.3.PTC, ORC and cooling tower system analysis

The integrated system is simulated for off design conditions of varying solar input and ambient conditions.The daily solar irradiance (Figure 37) of the representative days of 'fall equinox' (Sep), 'summer solstice' and 'winter solstice' are fed as the varying solar input to the numerical model along with the varying wet bulb temperature. Inorder to simulate the dynamic behavior of the whole system, the solar irradiance is kept constant for every 5 minutes of a day. This assumption allows to observe the transient and dynamic behaviour of the system with varying energy input through the course of the day. The geometrical details of Table 16 and Table **18** are used for ORC and PTC respectively.

The TMY2 data is used for ambient conditions for wet bulb temperature. Figure 40 represents the trend of ambient temperature for the representative days for Larnaca, Cyprus. The simulations are run for the course of a whole day (24 hours).

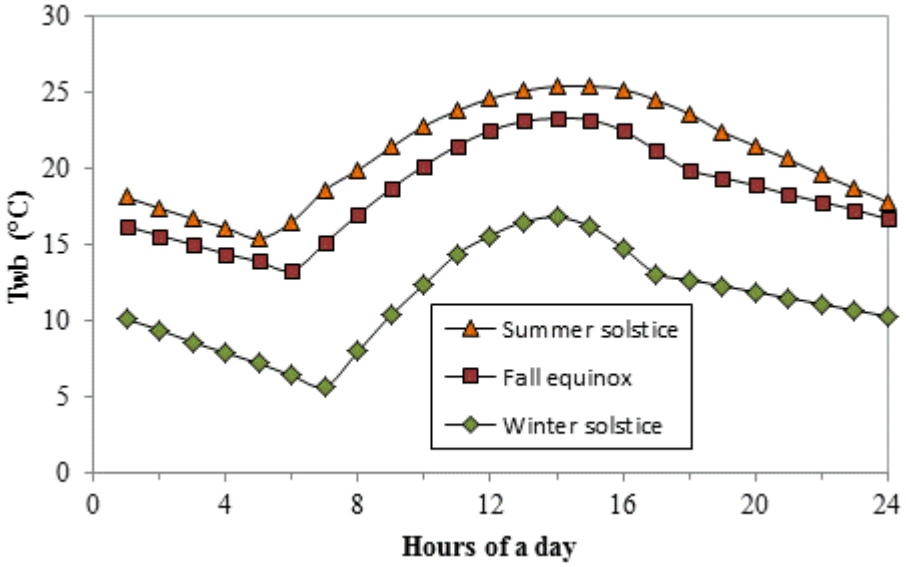

Figure 40: Ambient temperature profile at each hour of representative days of the year.

Figure 41, Figure 42 and Figure 43 represent the temperature profiles at the exit of the PTC, the evaporator, condenser and cooling tower of the ORC. Plots show the profile for a complete course of the representative days. For the initial hours of the day, the water in the PTC remains at a constant temperature due to off times for solar irradiation. The PTC starts as the sun rises and starts rising the water temperature. ORC is connected to the heat source and starts operating at a minimum operating temperature of 80°C. It is very crucial to control to the outlet temperature of the heating water from the PTC in order to avoid critical temperature limit of the working refrigerant. Since the PTC takes the outlet water from the evaporator as the inlet and transfers heat to increase the temperature, it is essential to control the inlet temperature of the PTC to avoid high temperature output at the exit. A pseudo control strategy is applied to control the inlet temperature of the PTC. A virtual sink is assumed at the exit of the evaporator to dump extra energy of the water before entering PTC.

Evidently summer solstice and fall equinox experience maximum solar irradiation in the middle of the day (at noon) on a normal surface. These high available solar resources cause higher useful heat transfer to the PTC which raises the water temperature. In the Figure 41 and Figure

42 wiggles at the middle of the days can be seen. These wiggles of PTC outlet temperature are due to the heat dumping control strategy due to high temperature. These wiggles are also translated to the evaporator outlet temperature. Whereas in the winter solstice (Figure 43) due to low solar resources and available energy the temperature profile is smooth in the middle of the day.

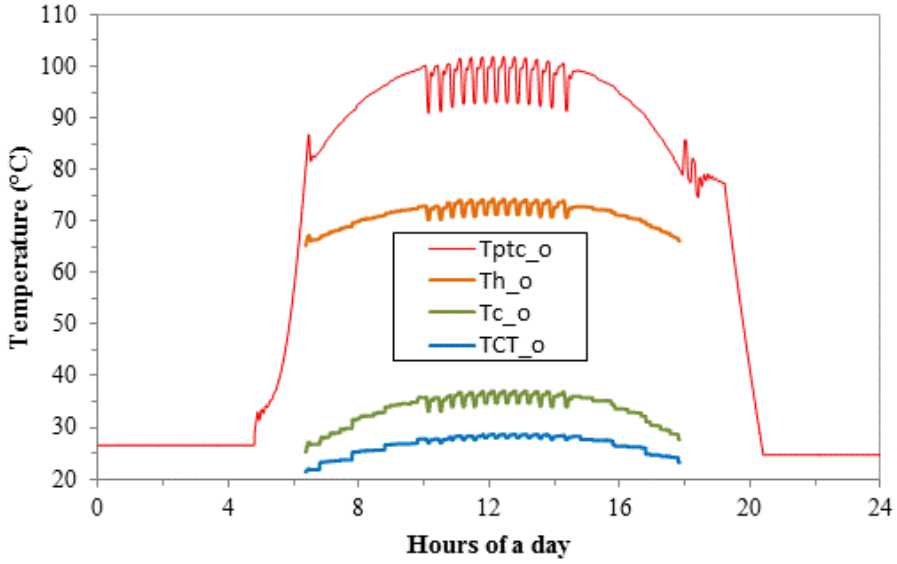

Figure 41: Temperature profile at the outlet of PTC, evaporator, condenser and cooling tower for summer solstice.

The maximum temperatures achieved at the exit of the PTC for summer solstice, fall equinox and winter solstice are 102°C, 100.7°C and 92°C respectively. Whereas, at the exit of the evaporator in operation the maximum temperatures are 74.2°C, 73°C and 67°C for summer solstice, fall equinox and winter solstice respectively. It can be deduced that there is no significant difference in the peak temperature for summer solstice and fall equinox. These two days differ with time of the operation due to seasonal day lengths. However a significant difference can be observed in the winter solstice peak PTC temperature, which is also depicted by a smooth temperature profile at the mid of the day. The outlet temperature of the PTC drops as sun sets and become constant for the rest of the day (night time).

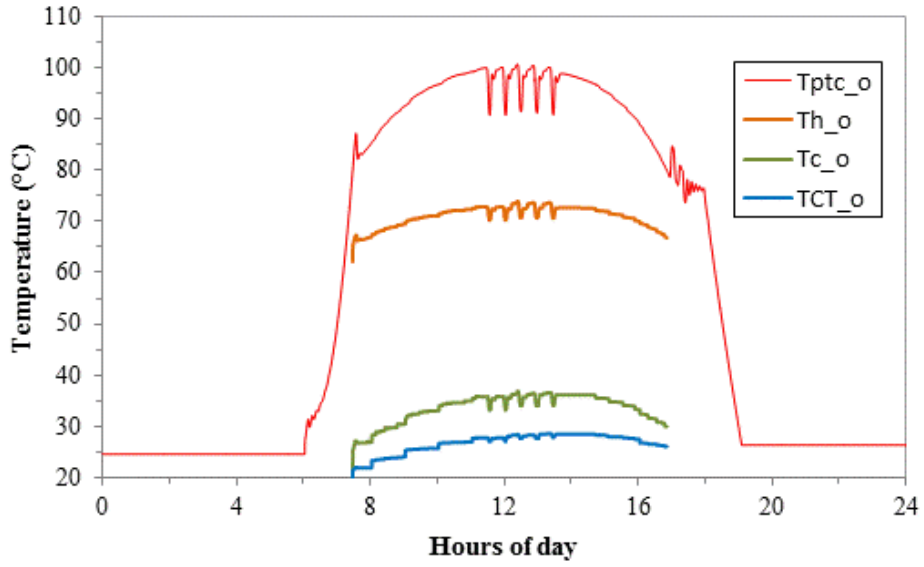

Figure 42: Temperature profile at the outlet of PTC, evaporator, condenser and cooling tower for equinox (Sep).

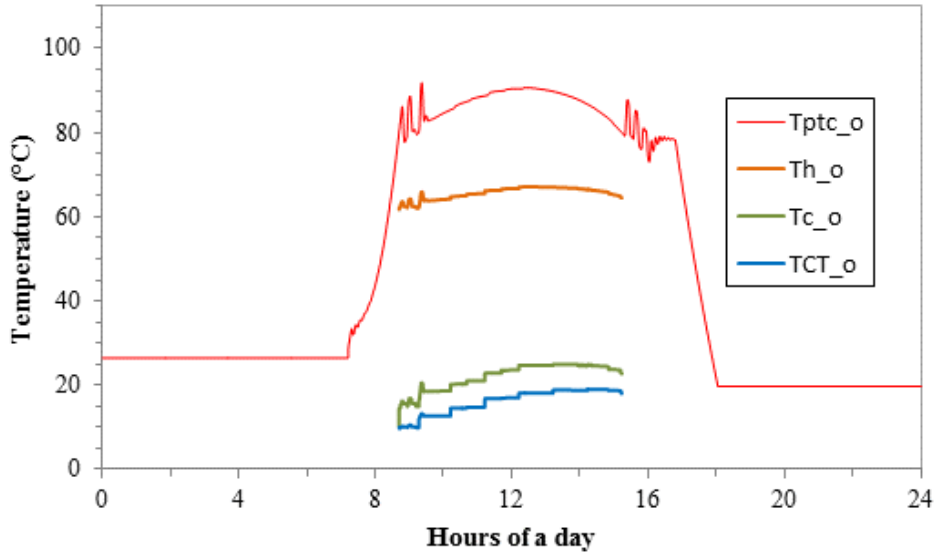

Figure 43: Temperature profile at the outlet of PTC, evaporator, condenser and cooling tower for winter solstice.

Figure 41, Figure 42 and Figure 43 also represent the temperature profiles at the exit of the cooling tower and condenser for representative days. The cooling of the condenser is controlled by varying the pressure. Fluctuations in the condenser outlet temperature can be observed for

the summer solstice and fall equinox. The viable reason of these fluctuations is due to the high wet bulb temperatures in these days, which alters the cooling performance of the cooling tower. Cooling water inlet temperature to the condenser is important in order to have enough heat transfer between the refrigerant and cooling water to complete the thermodynamic cycle. Whereas, the temperature profile for the winter solstice is quite smooth due to low wet bulb temperatures through the course of the day which improves the cooling performance.

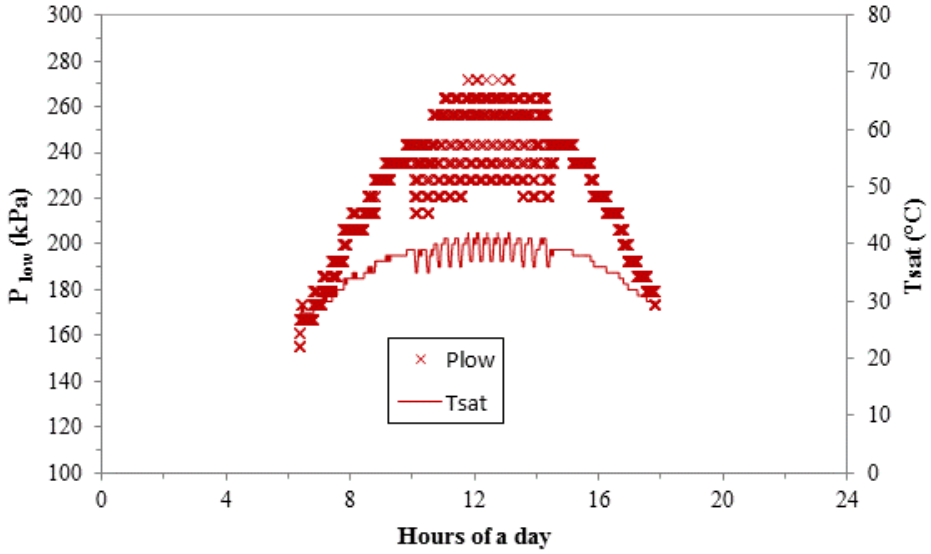

Figure 44: Pressure and saturation temperature variation at condenser for summer solstice.

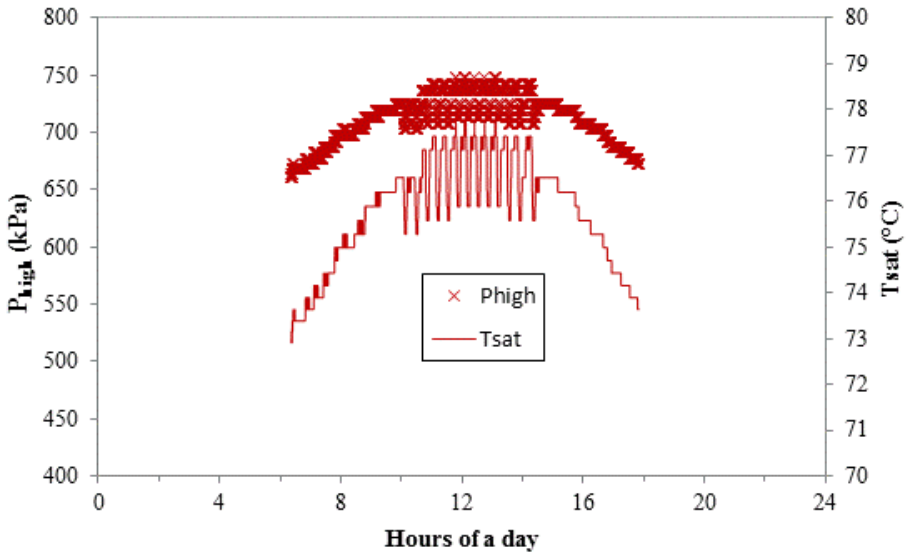

Figure 45: Pressure and saturation temperature variation at evaporator for summer solstice.

The pressure fluctuations for the ORC operational time are depicted in Figure 44 and Figure 45 for summer solstice. The condenser pressure variation causes the variation in the high pressure as well. The midday variations are due to the same reason discussed above.

Figure 46, Figure 47 and Figure 48 represent the available solar power and the useful rate of heat transfer to the PTC water. The maximum available solar power and useful heat transfer to the PTC do not vary for the summer solstice and fall equinox. The peak instantaneous values for useful and available thermal power for summer solstice are 325.6 kW and 468.3 kW and for fall equinox are 313.1 kW and 451 kW. Whereas winter solstice experiences 268.2 kW as the useful thermal power to the PTC from an available solar power of 397.2 kW, least among the three representative days and for the shortest time of the day.

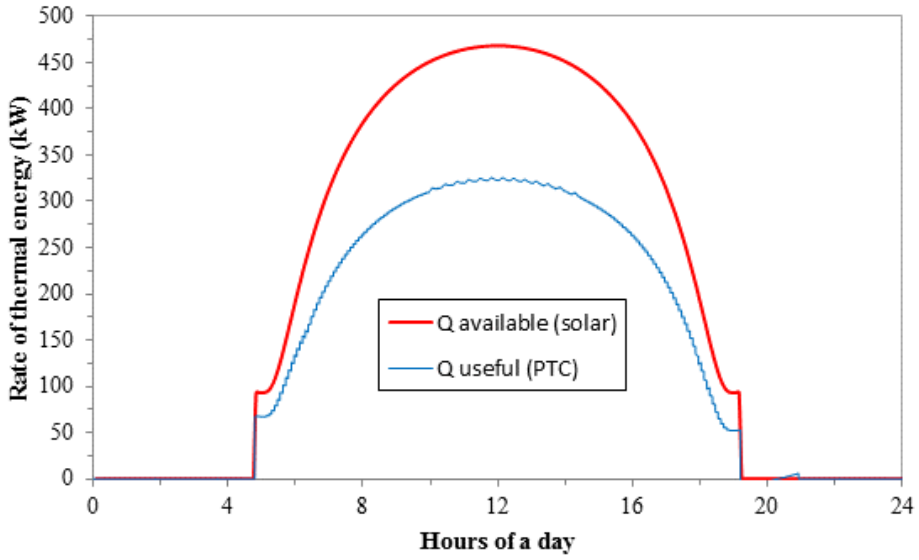

Figure 46: Available solar power and useful power to the PTC for summer solstice.

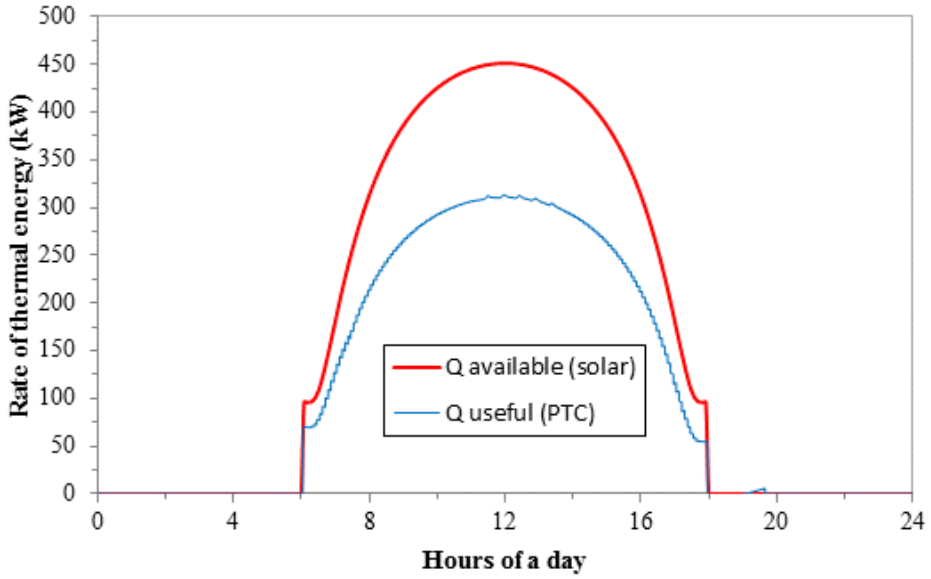

Figure 47: Available solar power and useful power to the PTC for equinox (Sep).

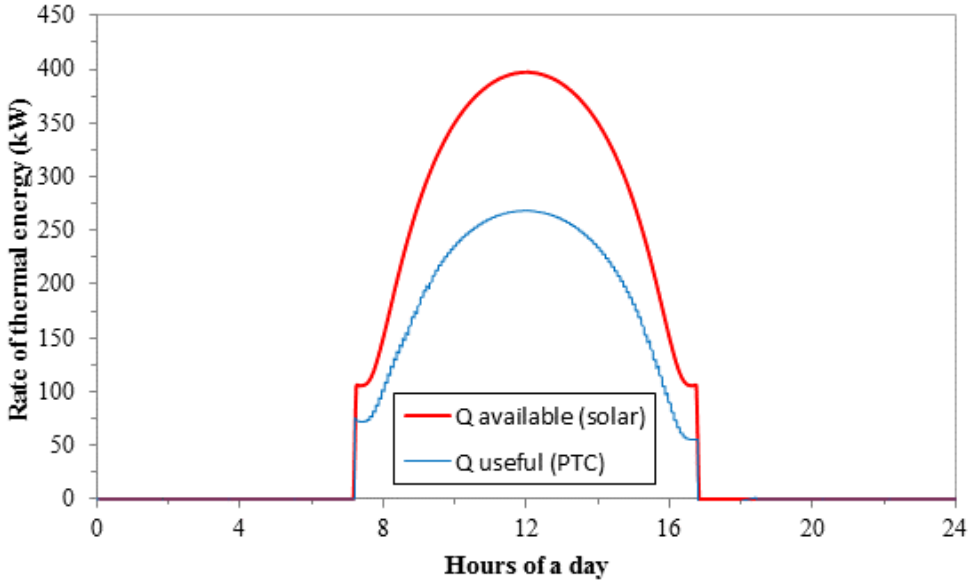

Figure 48: Available solar power and useful power to the PTC for winter solstice.

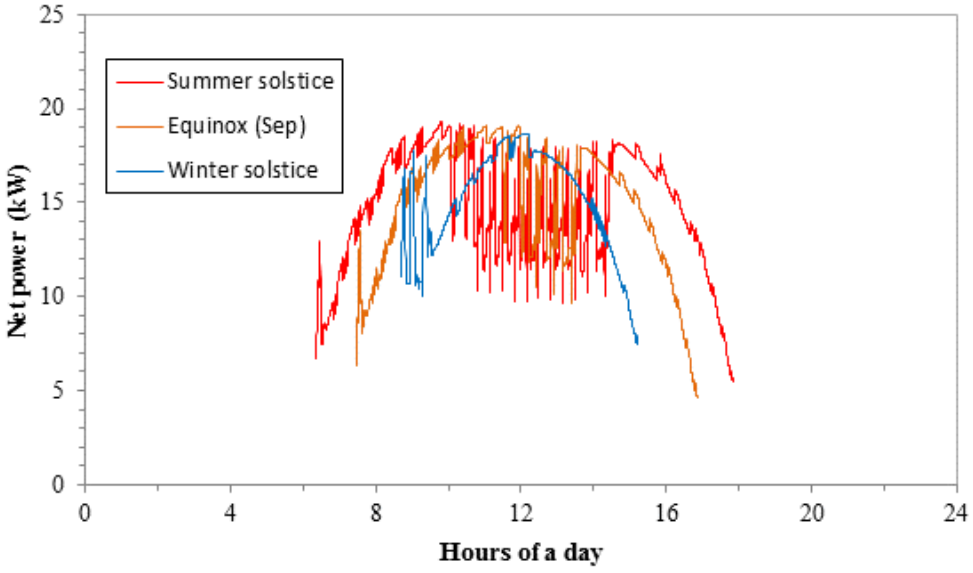

Figure 49: Net power output through the course of representative days.

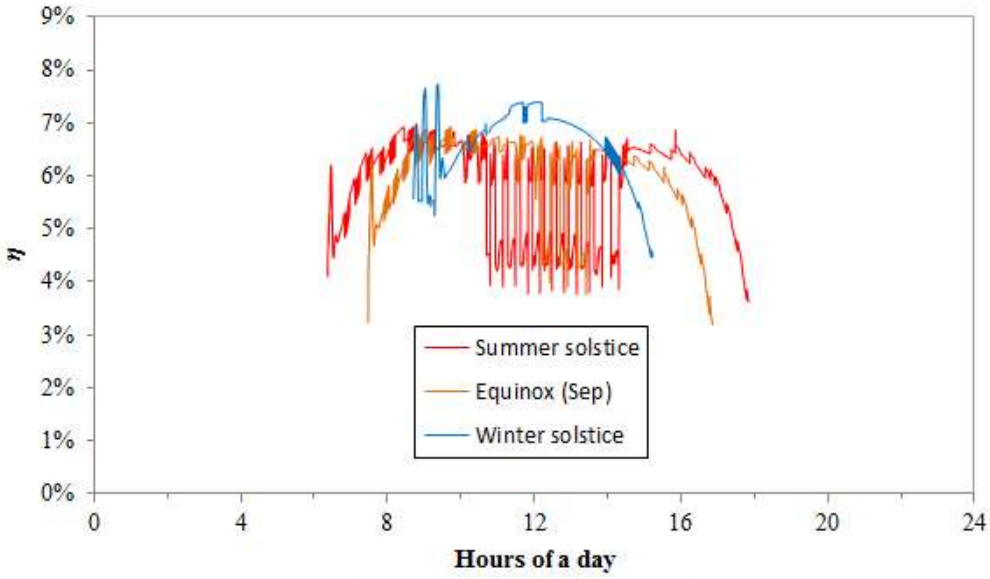

Figure 50: ORC efficiency through the course of representative days.

Figure 49 and Figure 50 show the net power output from the ORC and system efficiency through the course of the day for the representative days of the year. It can be seen from the figure that there are fluctuations in the mid of the ORC operation. These fluctuations are due to the control strategies for PTC outlet temperature and condenser pressure. As it can be seen that

these quantities vary for the summer solstice and fall equinox due to higher available heat input and higher wet bulb temperature. Whereas in winter solstice, the net power and efficiency of the system show quite smooth trend during the operational time.

The maximum instantaneous power output for summer solstice, fall equinox and winter solstice are 19.2 kW, 19 kW and 21.1 kW respectively. Evidently the operational time of summer solstice is maximum as compare to the other two days. The maximum system efficiencies achieved are 7.7% for winter solstice and 6.9% for the other two days. The average power across the days is found to be 14.5 kW, 14.88 kW and 15.16 kW for summer solstice, fall equinox and winter solstice respectively.

Chapter 5

CONCLUSION

This work addressed the system level performance of a solar driven Organic Rankine Cycle power plant which comprises of three main sub systems; Parabolic Trough Collectors as the heat source for ORC, the ORC unit which comprised of 'evaporator', 'condenser', 'pump' and 'turbine', and the wet cooling tower. All the sub-systems are integrated with each other to simulate the overall performance under constant and variable conditions.

A detailed numerical modeling of Parabolic Trough Collectors by taking into account the inherent transient nature is carried out, which helped in coping up with the variable solar input. The useful energy absorbed by the PTCs through the course of the day highly depends upon several factors such as temperature across the PTC pipes, ambient temperature, mass flow rates and solar radiation. The solar radiation varies significantly through the course of the day which demands a dynamic model to physically replicate the phenomenon. Solar resources (Direct normal irradiance) for a particular location, being one of the important design and input parameter for the simulations, are evaluated for a particular location. Reasonable assumptions are made to calculate the solar resources through the course a complete day.

The developed numerical model for PTC is validated with the experimental and numerical results from the available literature. The results from the developed PTC model and available data show close agreement. The validated PTC model is extended to analyze the concept of 'Double pass counter flow' in PTC in which the fluid inside the receiver (tube) of the PTC is recycled to pre-mix with the incoming cold water. To check the effect of double pass pre-mixing several cases are simulated with different conditions of mass flow rates and fractions of recycle. It is observed that there is not much difference between the efficiencies of PTC single pass (conventional PTC configuration) and the simulated cases of double pass under similar conditions of solar irradiance and inlet water temperature. Whereas the outlet temperature of the water with similar conditions is higher in the case of double pass as compared to that of single pass at steady state conditions.

The developed numerical model of single pass PTC is coupled with a transient ORC model with refrigerant R245fa as the working fluid. The evaporator and condenser are modeled with transient assumptions since the response time due to the thermal inertia of the working fluid poses physical limitations. While the pump and turbines (expander) are modeled with steady state assumptions due to their rapid response time in the ORC. The results of the dynamic models of evaporator and condenser at steady state are matched with the steady state results found in the literatures under similar conditions. In addition to the component level verification of evaporator and condenser from the literature, the integrated ORC is also verified with the design conditions available in the literature. A simplistic model of wet cooling tower is developed with constant cooling tower efficiency. Wet cooling tower model is based on steady state assumptions and works with condenser outlet temperature and wet bulb temperature.

Several different cases are simulated on the integrated system with different physical conditions. The summary of the cases are as follows:

1. ORC: The verified design conditions are fed with a range of hot water inlet temperature and refrigerant mass flow rate. A pseudo control strategy is applied to the low pressure side of the thermodynamic cycle in order to control the pressure. It is observed that the net power increases with the increase of hot water inlet temperature as well as the refrigerant mass flow rates.
2. PTC, ORC and cooling tower integration: All the sub systems are integrated with variable solar and ambient condition (wet bulb temperature) through the course of three representative days of the year. A control strategy is applied to control the PTC outlet temperature to avoid the critical temperature of the refrigerant. It is found that during the summer solstice and fall equinox, the temperatures as well as the condenser pressure vary due to high availability of thermal power which causes fluctuations in the net power output. Whereas for the winter solstice, due to low available thermal power and low ambient temperature the power output during the operational time is smoother as compared to the other two days.

For the continuation and future work, the developed models can be used to devise a control strategy in order to run the system at steady conditions. Several physical parameters such as mass flow rates in different loops of the system can be manipulated in addition to that outlet temperature at the exit of the evaporator and PTC can also be controlled with thermal storage.

Pressure of the condenser can be modified in a more sophisticated manner to optimize the overall performance of the system. Furthermore, beside the above mentioned one of the potential areas is the detail modeling of expanders for these types of systems.

REFERENCES

[1] (IEA) International Energy Agency, "Key World Energy Statistics," 2009.

[2] Energy Information Administration, "International Energy Outlook 2011.U.S," 2011.

[3] "Skeptic's Corner: Did You Know?" [Online]. Available: http://jer-skepticscorner.blogspot.com/2009/07/did-you-know.html. [Accessed: 21-Mar-2013].

[4] P. Moriarty and D. Honnery, "What is the global potential for renewable energy?," *Renewable and Sustainable Energy Reviews*, vol. 16, no. 1, pp. 244–252, Jan. 2012.

[5] REN21, "Renewables 2011 Global Status Report."

[6] T. B. Johansson and L. Burnham, *Renewable Energy: Sources for Fuels and Electricity*. Island Press, 1993.

[7] Smil.V, "Energy at the crossroads," presented at the OECD Global Science Forum, Paris, 2006.

[8] Worldwatch Institute, "State of the World 2009," 2009.

[9] T. Faraz, "Benefits of Concentrating Solar Power over Solar Photovoltaic for power generation in Bangladesh," in *Developments in Renewable Energy Technology (ICDRET), 2012 2nd International Conference on the*, 2012, pp. 1–5.

[10] IRENA, "Concentrating Solar Power Technology Brief," Jan. 2013.

[11] Global Energy Network Institute, "Review and Comparison of Different Solar Energy Technologies," Aug. 2011.

[12] A. A. E. Ibrahim, M. R. I. Ramadan, A. A. ElSebaii, and S. M. ElBroullosey, "Estimation of Solar Irradiance on Inclined Surfaces Facing South in Tanta, Egypt," *International Journal of Renewable Energy Research (IJRER)*, vol. 1, no. 1, pp. 18–25, Aug. 2011.

[13] L. P. Naing and D. Srinivasan, "Estimation of solar power generating capacity," in *2010 IEEE 11th International Conference on Probabilistic Methods Applied to Power Systems (PMAPS)*, June, pp. 95–100.

[14] Qu. M, Archer. D.H, Masson. S. V, "A Linear Parabolic Trough Solar Collector Performance Model," presented at the Proceedings of the Sixth International Conference for Enhanced Building Operations, Shenzhen, China, 2006.

[15] S. D. Odeh, G. L. Morrison, and M. Behnia, "Modelling of parabolic trough direct steam generation solar collectors," *Solar Energy*, vol. 62, no. 6, pp. 395–406, Jun. 1998.

[16] S. D. Odeh and G. L. Morrison, "Optimization of parabolic trough solar collector system," *International Journal of Energy Research*, vol. 30, no. 4, pp. 259–271, Mar. 2006.

[17] Azizian. K, Yaghoubi. M, Hesami. R, Kanan. P, "Design analysis for expansion of Shiraz solar power plant to 500 kW power generation capacity," presented at the World Renewable Energy Congress-2011, Sweden, 2011.

[18] R. W. Bialobrzeski, “Optimization of a SEGS solar field for cost effective power output,” 10-Jul-2007. [Online]. Available: https://smartech.gatech.edu/handle/1853/24631. [Accessed: 21-Mar-2013].
[19] O. García-Valladares and N. Velázquez, “Numerical simulation of parabolic trough solar collector: Improvement using counter flow concentric circular heat exchangers,” *International Journal of Heat and Mass Transfer*, vol. 52, no. 3–4, pp. 597–609, Jan. 2009.
[20] F. Vélez, J. J. Segovia, M. C. Martín, G. Antolín, F. Chejne, and A. Quijano, “A technical, economical and market review of organic Rankine cycles for the conversion of low-grade heat for power generation,” *Renewable and Sustainable Energy Reviews*, vol. 16, no. 6, pp. 4175–4189, Aug. 2012.
[21] B. F. Tchanche, G. Lambrinos, A. Frangoudakis, and G. Papadakis, “Low-grade heat conversion into power using organic Rankine cycles – A review of various applications,” *Renewable and Sustainable Energy Reviews*, vol. 15, no. 8, pp. 3963–3979, Oct. 2011.
[22] Y. Dai, J. Wang, and L. Gao, “Parametric optimization and comparative study of organic Rankine cycle (ORC) for low grade waste heat recovery,” *Energy Conversion and Management*, vol. 50, no. 3, pp. 576–582, Mar. 2009.
[23] B. Saleh, G. Koglbauer, M. Wendland, and J. Fischer, “Working fluids for low-temperature organic Rankine cycles,” *Energy*, vol. 32, no. 7, pp. 1210–1221, Jul. 2007.
[24] Bamgbopa. M. O, Uzgoren. E., “Transient Modeling of an Organic Rankine Cycle (ORC) Unit with R245fa as the Working Fluid.,” presented at the NuRER 2012 – III. International Conference on Nuclear & Renewable Energy Resources, Istanbul, 2012.
[25] D. Wei, X. Lu, Z. Lu, and J. Gu, “Dynamic modeling and simulation of an Organic Rankine Cycle (ORC) system for waste heat recovery,” *Applied Thermal Engineering*, vol. 28, no. 10, pp. 1216–1224, Jul. 2008.
[26] T. Guo, H. X. Wang, and S. J. Zhang, “Fluids and parameters optimization for a novel cogeneration system driven by low-temperature geothermal sources,” *Energy*, vol. 36, no. 5, pp. 2639–2649, May 2011.
[27] N. Lior and K. Koai, “Solar-powered/fuel-assisted rankine cycle power and cooling system: sensitivity analysis,” J Journal Name: J. Sol. Energy Eng.; (United States); Journal Volume: 106 1984.
[28] M. Kane, “Small hybrid solar power system,” *Energy*, vol. 28, no. 14, pp. 1427–1443, Nov. 2003.
[29] A. M. Patnode, “Simulation and Performance Evaluation of Parabolic Trough Solar Power Plants,” 2006. [Online]. Available: http://digital.library.wisc.edu/1793/7590.
[30] M. Wang, J. Wang, Y. Zhao, P. Zhao, and Y. Dai, “Thermodynamic analysis and optimization of a solar-driven regenerative organic Rankine cycle (ORC) based on flat-plate solar collectors,” *Applied Thermal Engineering*, vol. 50, no. 1, pp. 816–825, Jan. 2013.

[31] "Current Status of Concentrated Solar Power in the world | REVE." [Online]. Available: http://www.evwind.es/2013/06/15/current-status-of-concentrated-solar-power-in-the-world/33675. [Accessed: 24-Jul-2013].
[32] "Parabolic trough - Wikipedia, the free encyclopedia." [Online]. Available: http://en.wikipedia.org/wiki/Parabolic_trough. [Accessed: 10-Oct-2013].
[33] in *Solar Engineering of Thermal Processes*, Hoboken, NJ, USA: John Wiley & Sons, Inc., 2013, pp. 422–446.
[34] *Fundamentals of heat and mass transfer*, 6th ed. Hoboken, NJ: John Wiley, 2007.
[35] "SYLTHERM | Heat Transfer Fluids | The Dow Chemical Company." [Online]. Available: http://www.dow.com/heattrans/products/synthetic/syltherm.htm. [Accessed: 22-Jul-2013].
[36] H. Wang and S. Touber, "Distributed and non-steady-state modelling of an air cooler," *International Journal of Refrigeration*, vol. 14, no. 2, pp. 98–111, Mar. 1991.
[37] *Boilers, evaporators, and condensers*. New York: Wiley, 1991.
[38] L. D. Boyko and G. N. Kruzhilin, "Heat transfer and hydraulic resistance during condensation of steam in a horizontal tube and in a bundle of tubes," *International Journal of Heat and Mass Transfer*, vol. 10, no. 3, pp. 361–373, Mar. 1967.
[39] Z. Shengjun, W. Huaixin, and G. Tao, "Performance comparison and parametric optimization of subcritical Organic Rankine Cycle (ORC) and transcritical power cycle system for low-temperature geothermal power generation," *Applied Energy*, vol. 88, no. 8, pp. 2740–2754, Aug. 2011.
[40] I. K. Smith, N Stosic, A. Kovacevic, and R Langson, "Cost effective small scale ORC systems for power recovery from low enthalpy geothermal sources."

APPENDICES

MATERIAL PROPERTIES

Properties of the water

Specific heat (*Cp*) = 4.2174356 - 0.0056181625 T + 0.0012992528 $T^{1.5}$ - 0.00011535353 T^{2} + 4.14964e-6 $T^{2.5}$ (kJ/kgK)

Viscosity (μ) = 1.0/ (557.82468 + 19.408782 T + 0.1360459 T^{2} -3.1160832e-4 T^{3}) (Pa sec)

Thermal conductivity (*k*) = 0.5650285 + 0.0026363895 T - 0.00012516934 $T^{1.5}$ - 1.5154918e-6 T^{2} - 0.0009412945 $T^{0.5}$ (W/mK)

Density (ρ) = 999.79684 + 0.068317355 T - 0.010740248 T^{2} + 0.00082140905 $T^{2.5}$ - 2.3030988e-5 T^{3} (kg/m^3)

Properties of the oil (syltherm800 oil)

Temperature (°C)	Specific Heat (J/kg)	Density (kg/m3)	Thermal Conductivity (W/mK)	Viscosity (mPa-s)	Viscosity (Pa-sec)	Vapor Pressure (kPa)
-40	1506	990.61	0.1463	51.05	0.05105	0
0	1574	953.16	0.1388	15.33	0.01533	0
40	1643	917.07	0.1312	7	0.007	0.1
80	1711	881.68	0.1237	3.86	0.00386	1.46
120	1779	846.35	0.1162	2.36	0.00236	9.3
160	1847	810.45	0.1087	1.54	0.00154	35
200	1916	773.33	0.1012	1.05	0.00105	94.6
240	1984	734.35	0.0936	0.74	0.00074	204.8
280	2052	692.87	0.0861	0.54	0.00054	380.2
320	2121	648.24	0.0786	0.41	0.00041	630.5
360	2189	599.83	0.0711	0.31	0.00031	961.2
400	2257	547	0.0635	0.25	0.00025	1373

Specific heat (*Cp*) = 1.7073 T + 1574.3 (J/kgK)

Viscosity (μ) = 0.0132 exp (-0.011 T) (Pa sec)

Thermal conductivity (*k*) = -0.0002 T + 0.1388 (W/mK)

Density (ρ) = -0.9841 T + 960.06 (kg/m^3)

Properties of the receiver/internal tube (Stainless steel cermet coated)

Specific heat (*Cp*) = 435 (J/kgK)

Thermal conductivity (*k*) = 54 (W/mK)

Density (ρ) = 8073 (kg/m^3)

Emittance (ε) = 0.14

Properties of the glass cover (Low iron glass)

Specific heat (*Cp*) = 500 (J/kgK)

Thermal conductivity (*k*) = 1.05 (W/mK)

Density (ρ) = 2000 (kg/m^3)

Emittance (ε) = 0.4

Properties of the air (at 20 °c)

Specific heat (*Cp*) = 1005 (J/kgK)

Density (ρ) = 1.205 (kg/m^3)

Viscosity (μ) = 18.207e-6 (Pa sec)

Thermal conductivity (*k*) = 0.0257 (W/mK)

Thermal diffusivity (α) = 2.12e-5 (m^2/s)

DISCRETIZED NUMERICAL DOMAIN FOR PARABOLIC TROUGH COLLECTOR

Computational domain for the fluid flow inside the receiver of PTC

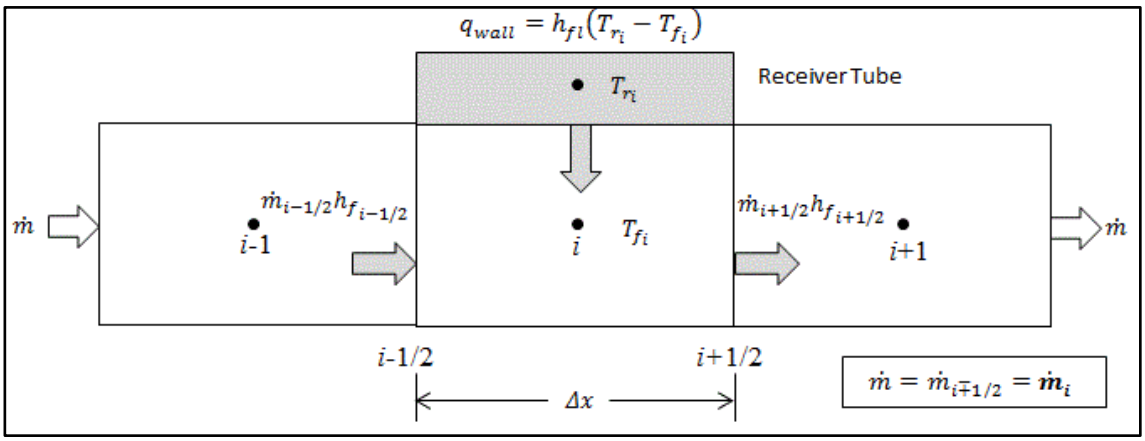

$$\frac{dE_i}{dt} = q_{wall} + \dot{m}_{i-1/2}h_{f\,i-1/2} - \dot{m}_{i+1/2}h_{f\,i+1/2}$$

$$\rho_f \Delta V_f \frac{{h_{f_i}}^{t+1} - {h_{f_i}}^{t}}{\Delta t} = q_{wall} + \dot{m}_i \left({h_{f_{i-1}}}^{t+1} - {h_{f_i}}^{t+1}\right) + \Delta V_f \frac{{P_i}^{t+1} - {P_i}^{t}}{\Delta t}$$

$$\rho_f \Delta V_f \frac{{h_{f_i}}^{t+1} - {h_{f_i}}^{t}}{\Delta t} = q_{wall} + \dot{m}_i \left({h_{f_{i-1}}}^{t+1} - {h_{f_i}}^{t+1}\right) + \Delta V_f \frac{{P_i}^{t+1} - {P_i}^{t}}{\Delta t}$$

$${c_{p_f}T_{f_i}}^{t+1} = {c_{p_f}T_{f_i}}^{t} + \frac{\Delta t}{\rho_f \Delta V_f}\left[h_{fl}A_{fl}\left({T_{r_i}}^{t} - {T_{f_i}}^{t}\right) + \dot{m}_i\left({c_{p_f}T_{f_{i-1}}}^{t+1} - {c_{p_f}T_{f_i}}^{t+1}\right)\right]$$

$${T_{f_i}}^{t+1} = \frac{(a){T_{f_{i-1}}}^{t+1} + {c_{p_f}T_{f_i}}^{t} + (b){T_{r_i}}^{t} - (b){T_{f_i}}^{t}}{c_{p_f} + a}$$

$$a = \frac{\dot{m}_i c_{p_f} \Delta t}{\rho_f \Delta V_f}, b = \frac{A_{fl}h_{fl}\Delta t}{\rho_f \Delta V_f}$$

Computational domain (1st node) for receiver tube analysis with energy transfers across the boundaries.

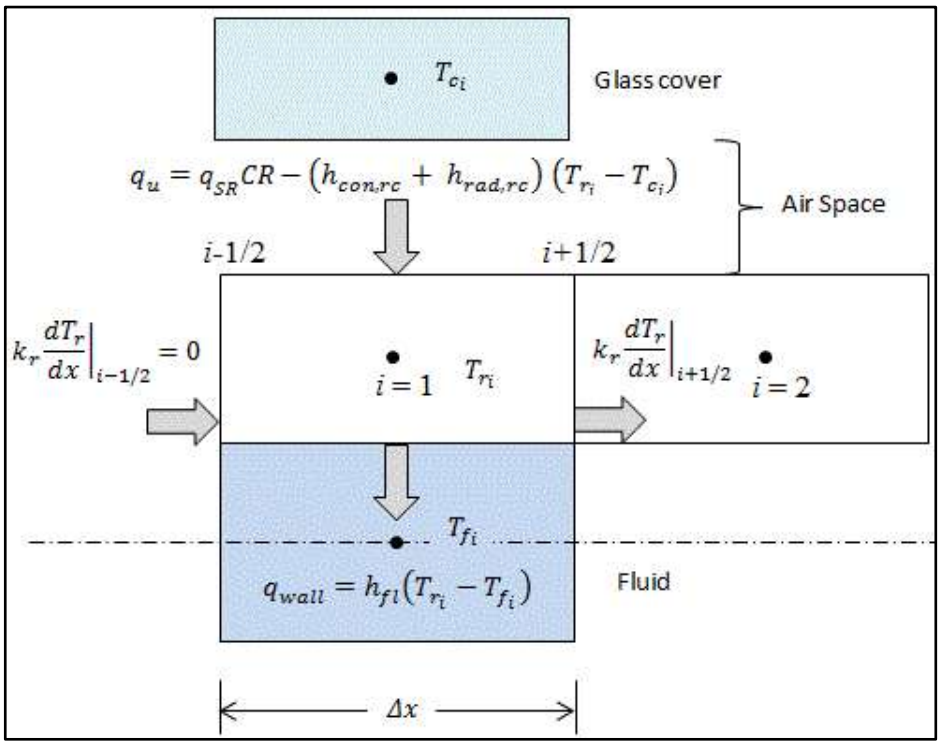

$$(q_u \pi D_{ro} - q_{wall} \pi D_{ri})dx + (\dot{q}_e - \dot{q}_w)A_{cr} = m_r \frac{dh_r}{dt}$$

$$(q_u \pi D_{ro} - q_{wall} \pi D_{ri})dx + \left(k_r \frac{dT_r}{dx}\Big|_{i+1/2} - k_r \frac{dT_r}{dx}\Big|_{i-1/2}\right)A_{cr} = m_r \frac{dh_r}{dt}$$

$$k_r \frac{dT_r}{dx}\Big|_{i-\frac{1}{2}} = 0$$

$$\{q_u \pi D_{ro} - h_{fl}({T_{r_i}}^{t+1} - {T_{f_i}}^{t+1})\pi D_{ri}\}\Delta x + \left[k_r \left(\frac{{T_{r_{i+1}}}^{t+1} - {T_{r_i}}^{t+1}}{\Delta x}\right)\right]A_{cr}$$

$$= \rho_r \Delta V_r c_{p_r} \frac{{T_{r_i}}^{t+1} - {T_{r_i}}^{t}}{\Delta t}$$

Computational domain (Middle nodes) for receiver tube analysis with energy transfers across the boundaries

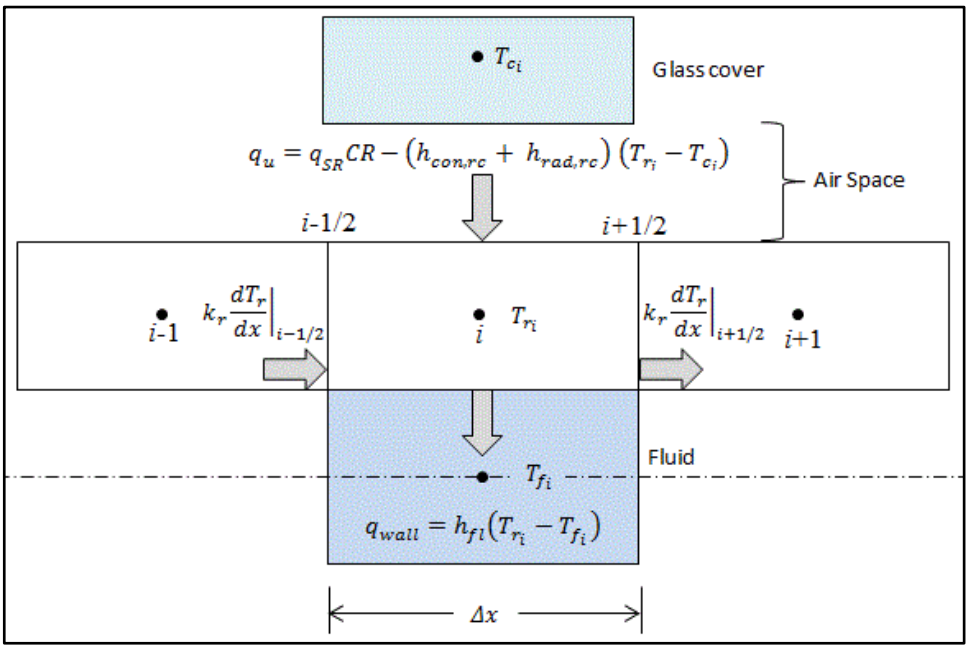

$$(q_u \pi D_{ro} - q_{wall} \pi D_{ri})dx + (\dot{q}_e - \dot{q}_w)A_{cr} = m_r \frac{dh_r}{dt}$$

$$(q_u \pi D_{ro} - q_{wall} \pi D_{ri})dx + \left(k_r \frac{dT_r}{dx}\Big|_{i+1/2} - k_r \frac{dT_r}{dx}\Big|_{i-1/2}\right)A_{cr} = m_r \frac{dh_r}{dt}$$

$$\{q_u \pi D_{ro} - h_{fl}({T_{f_i}}^{t+1} - {T_{r_i}}^{t+1})\pi D_{ri}\}\Delta x + \left[k_r\left(\frac{{T_{r_{i+1}}}^{t+1} - {T_{r_i}}^{t+1}}{\Delta x}\right) - k_r\left(\frac{{T_{r_i}}^{t+1} - {T_{r_{i-1}}}^{t+1}}{\Delta x}\right)\right]A_{cr} = \rho_r \Delta V_r \frac{{h_{r_i}}^{t+1} - {h_{r_i}}^{t}}{\Delta t}$$

$$\{q_u \pi D_{ro} - h_{fl}({T_{r_i}}^{t+1} - {T_{f_i}}^{t+1})\pi D_{ri}\}\Delta x + \left[k_r\left(\frac{{T_{r_{i+1}}}^{t+1} - {T_{r_i}}^{t+1}}{\Delta x}\right) - k_r\left(\frac{{T_{r_i}}^{t+1} - {T_{r_{i-1}}}^{t+1}}{\Delta x}\right)\right]A_{cr} = \rho_r \Delta V_r c_{p_r} \frac{{T_{r_i}}^{t+1} - {T_{r_i}}^{t}}{\Delta t}$$

Computational domain (nth node) for receiver tube analysis with energy transfers across the boundaries

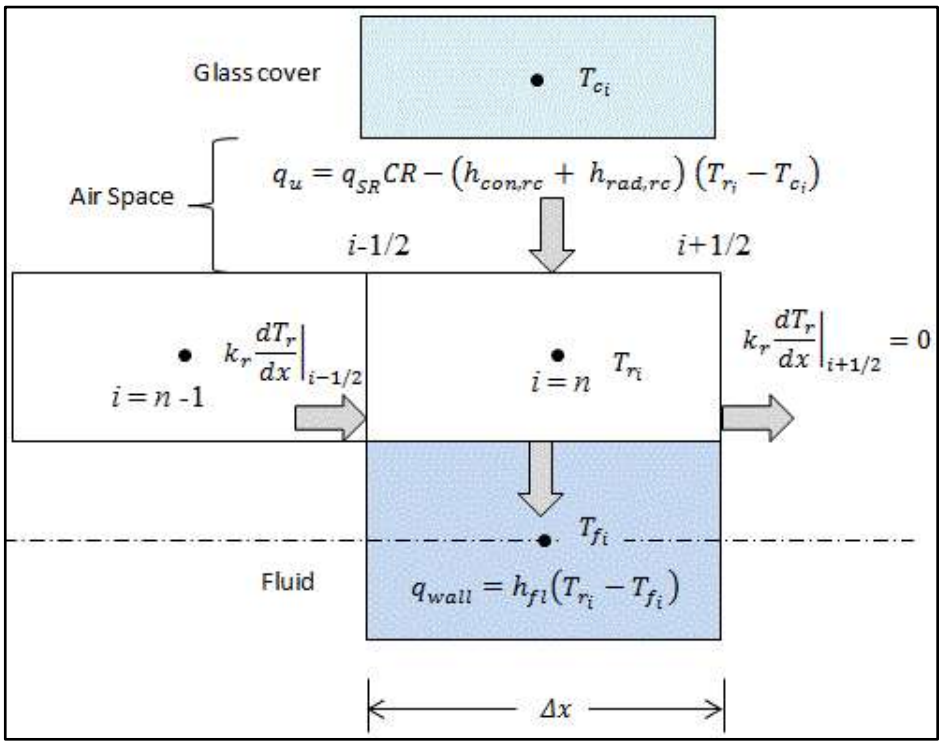

$$(q_u \pi D_{ro} - q_{wall} \pi D_{ri})dx + (\dot{q}_e - \dot{q}_w)A_{cr} = m_r \frac{dh_r}{dt}$$

$$(q_u \pi D_{ro} - q_{wall} \pi D_{ri})dx + \left(k_r \frac{dT_r}{dx}\Big|_{i+1/2} - k_r \frac{dT_r}{dx}\Big|_{i-1/2}\right)A_{cr} = m_r \frac{dh_r}{dt}$$

$$k_r \frac{dT_r}{dx}\Big|_{i+1/2} = 0$$

$$\{q_u \pi D_{ro} - h_{fl}({T_{r_i}}^{t+1} - {T_{f_i}}^{t+1})\pi D_{ri}\}\Delta x + \left[-k_r \left(\frac{{T_{r_i}}^{t+1} - {T_{r_{i-1}}}^{t+1}}{\Delta x}\right)\right]A_{cr} = \rho_r \Delta V_r c_{p_r} \frac{{T_{r_i}}^{t+1} - {T_{r_i}}^{t}}{\Delta t}$$

Computational domain (1st node) for cover analysis with energy transfers across the boundaries.

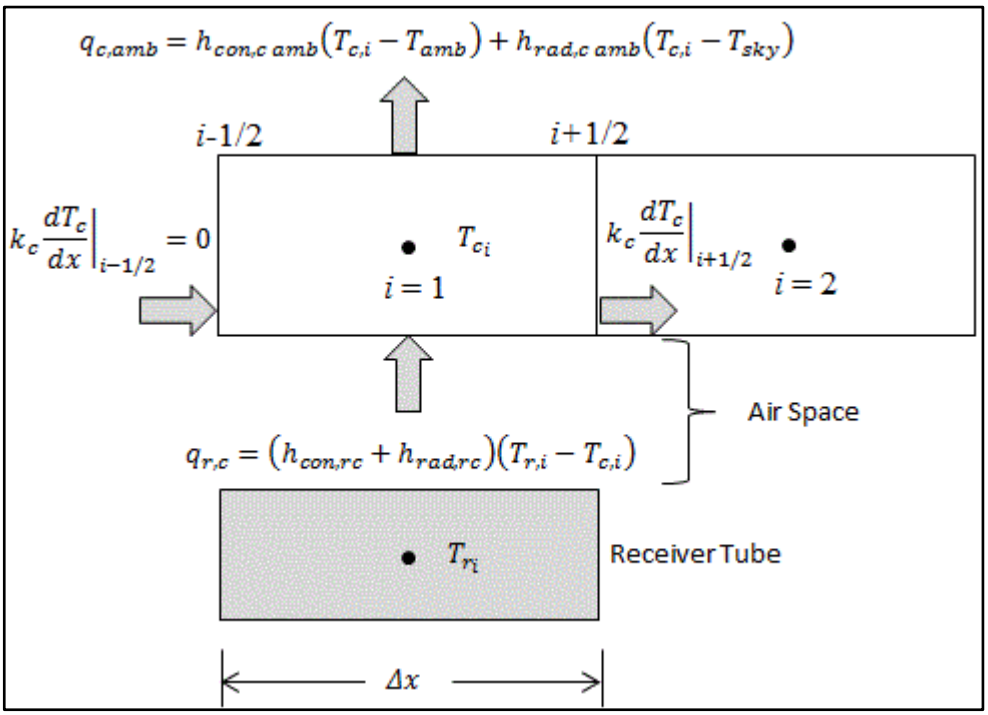

$$(q_{r,c}\pi D_{ro} - q_{c,amb}\pi D_{co})dx + (\dot{q}_e - \dot{q}_w)A_{cc} = m\frac{dh_c}{dt}$$

$$\begin{aligned}&\left[(h_{con,rc} + h_{rad,rc})(T_{r,i} - T_{c,i})\,\pi D_{ro}\right.\\&\quad\left. - \{h_{con,c\,amb}(T_{c,i} - T_{amb}) + h_{rad,c\,amb}(T_{c,i} - T_{sky})\}\,\pi D_{co}\right]\Delta x\\&\quad + \left(k_c\frac{dT_c}{dx}\Big|_{i+1/2} - k_c\frac{dT_c}{dx}\Big|_{i-1/2}\right)A_{cc} = \rho_c\Delta V_c\frac{{h_{c_i}}^{t+1} - {h_{c_i}}^{t}}{\Delta t}\end{aligned}$$

$$k_c\frac{dT_c}{dx}\Big|_{i-1/2} = 0$$

$$\begin{aligned}&\left[(h_{con,rc} + h_{rad,rc})({T_{r,i}}^{t+1} - {T_{c,i}}^{t+1})\,\pi D_{ro}\right.\\&\quad\left. - \{h_{con,c\,amb}({T_{c,i}}^{t+1} - T_{amb}) + h_{rad,c\,amb}({T_{c,i}}^{t+1} - T_{sky})\}\,\pi D_{co}\right]\Delta x\\&\quad + \left[k_c\left(\frac{{T_{c_{i+1}}}^{t+1} - {T_{c_i}}^{t+1}}{\Delta x}\right)\right]A_{cc} = \rho_c\Delta V_c c_{p_c}\frac{{T_{c_i}}^{t+1} - {T_{c_i}}^{t}}{\Delta t}\end{aligned}$$

Computational domain (Middle nodes) for cover analysis with energy transfers across the boundaries.

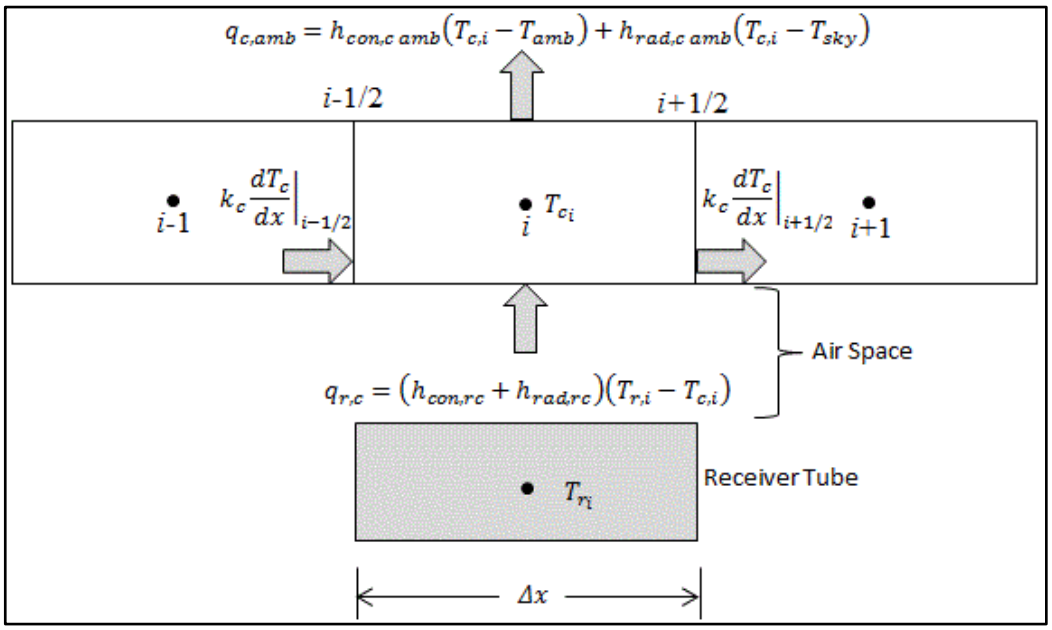

$$(q_{r,c}\pi D_{ro} - q_{c,amb}\pi D_{co})dx + (\dot{q}_e - \dot{q}_w)A_{cc} = m\frac{dh_c}{dt}$$

$$\begin{aligned}&\left[(h_{con,rc} + h_{rad,rc})(T_{r,i} - T_{c,i})\,\pi D_{ro}\right.\\&\quad\left. - \{h_{con,c\,amb}(T_{c,i} - T_{amb}) + h_{rad,c\,amb}(T_{c,i} - T_{sky})\}\,\pi D_{co}\right]\Delta x\\&\quad + \left(k_c\frac{dT_c}{dx}\Big|_{i+1/2} - k_c\frac{dT_c}{dx}\Big|_{i-1/2}\right)A_{cc} = \rho_c \Delta V_c \frac{{h_{c_i}}^{t+1} - {h_{c_i}}^{t}}{\Delta t}\end{aligned}$$

$$\begin{aligned}&\left[(h_{con,rc} + h_{rad,rc})({T_{r,i}}^{t+1} - {T_{c,i}}^{t+1})\,\pi D_{ro}\right.\\&\quad\left. - \{h_{con,c\,amb}({T_{c,i}}^{t+1} - T_{amb}) + h_{rad,c\,amb}({T_{c,i}}^{t+1} - T_{sky})\}\,\pi D_{co}\right]\Delta x\\&\quad + \left[k_c\left(\frac{{T_{c_{i+1}}}^{t+1} - {T_{c_i}}^{t+1}}{\Delta x}\right) - k_c\left(\frac{{T_{c_i}}^{t+1} - {T_{c_{i-1}}}^{t+1}}{\Delta x}\right)\right]A_{cc}\\&\quad = \rho_c \Delta V_c c_{p_c}\frac{{T_{c_i}}^{t+1} - {T_{c_i}}^{t}}{\Delta t}\end{aligned}$$

Computational domain (nth node) for cover analysis with energy transfers across the boundaries

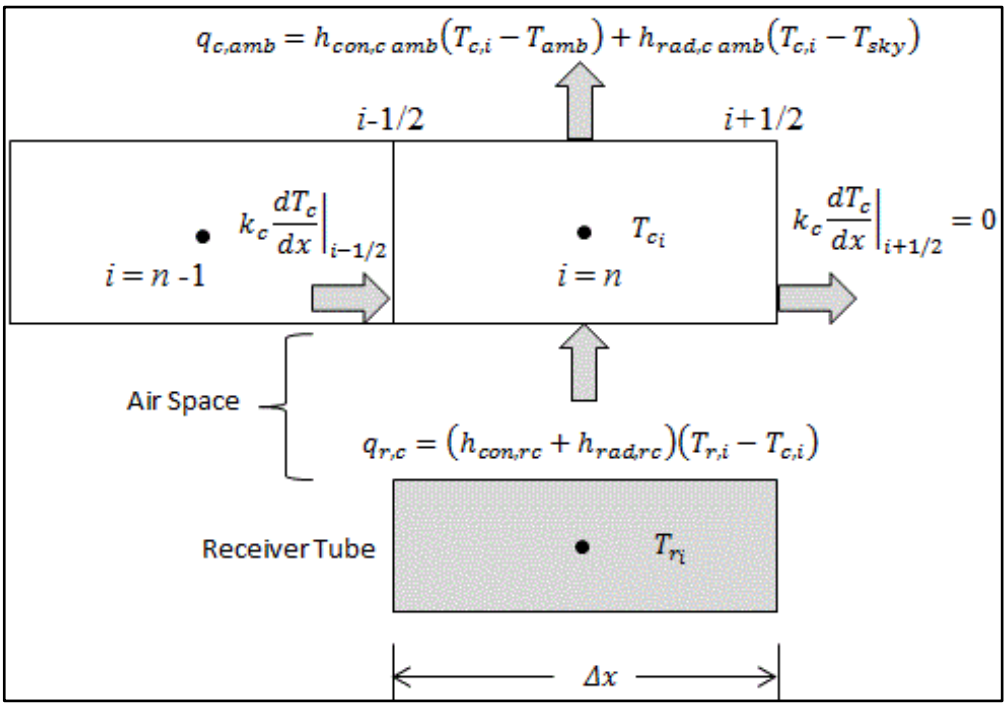

$$(q_{r,c}\pi D_{ro} - q_{c,amb}\pi D_{co})dx + (\dot{q}_e - \dot{q}_w)A_{cc} = m\frac{dh_c}{dt}$$

$$\begin{aligned}&\left[(h_{con,rc} + h_{rad,rc})(T_{r,i} - T_{c,i})\,\pi D_{ro}\right.\\&\quad\left. - \{h_{con,c\ amb}(T_{c,i} - T_{amb}) + h_{rad,c\ amb}(T_{c,i} - T_{sky})\}\,\pi D_{co}\right]\Delta x\\&\quad + \left(k_c\frac{dT_c}{dx}\Big|_{i+1/2} - k_c\frac{dT_c}{dx}\Big|_{i-1/2}\right)A_{cc} = \rho_c \Delta V_c \frac{{h_{c_i}}^{t+1} - {h_{c_i}}^{t}}{\Delta t}\end{aligned}$$

$$k_c\frac{dT_c}{dx}\Big|_{i+1/2} = 0$$

$$\begin{aligned}&\left[(h_{con,rc} + h_{rad,rc})({T_{r,i}}^{t+1} - {T_{c,i}}^{t+1})\,\pi D_{ro}\right.\\&\quad\left. - \{h_{con,c\ amb}({T_{c,i}}^{t+1} - T_{amb}) + h_{rad,c\ amb}({T_{c,i}}^{t+1} - T_{sky})\}\,\pi D_{co}\right]\Delta x\\&\quad + \left[-k_c\left(\frac{{T_{c_i}}^{t+1} - {T_{c_{i-1}}}^{t+1}}{\Delta x}\right)\right]A_{cc} = \rho_c \Delta V_c C_{p_c}\frac{{T_{c_i}}^{t+1} - {T_{c_i}}^{t}}{\Delta t}\end{aligned}$$

PRESSURE RATIO AND EFFICIENCY FOR EXPANDER

$r_p = P2/P1$	$\eta_{expander}$ (%)
2.846967	80.90992
3.4	81.718
4.054733	80.5984
4.269187	79.33614
4.699675	77.18205
5.132689	75.62068
5.5098	73.83773
5.94471	72.72089
6.378672	71.38178
6.977185	69.96651
7.521691	68.77421
8.12052	67.43303
8.774621	66.16525
9.48431	65.04496
10.08409	63.92605
10.7385	62.73237
11.5581	61.6107
12.54099	60.11652
13.57852	58.54757
14.67227	57.27428
15.5462	56.00374
16.14787	55.32936

Where P1 and P2 are the low and high pressures of the system respectively.

PRESSURE AND SATURATION TEMPERATURE VARIATION

Condenser pressure and saturation temperature variation for fall equinox

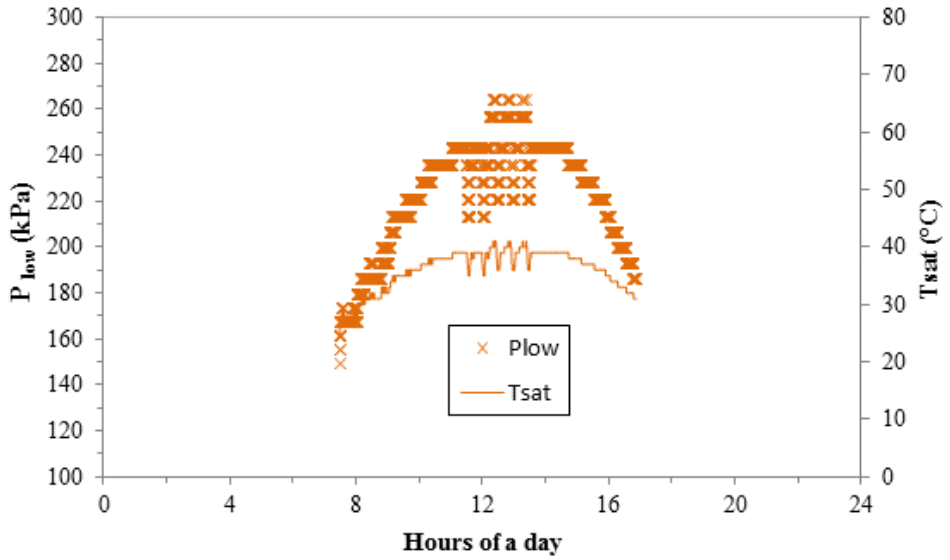

Evaporator pressure and saturation temperature variation for fall equinox

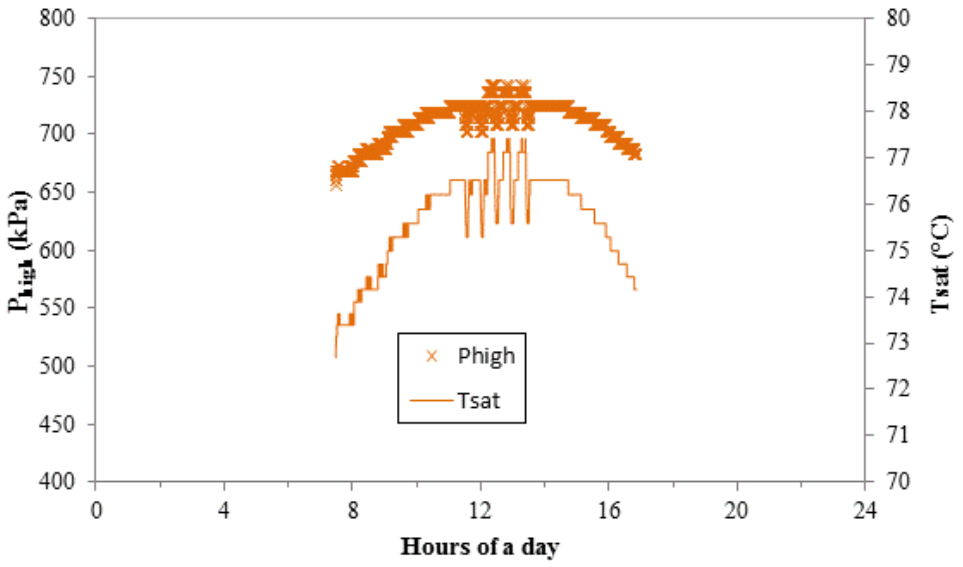

Condenser pressure and saturation temperature variation for winter solstice

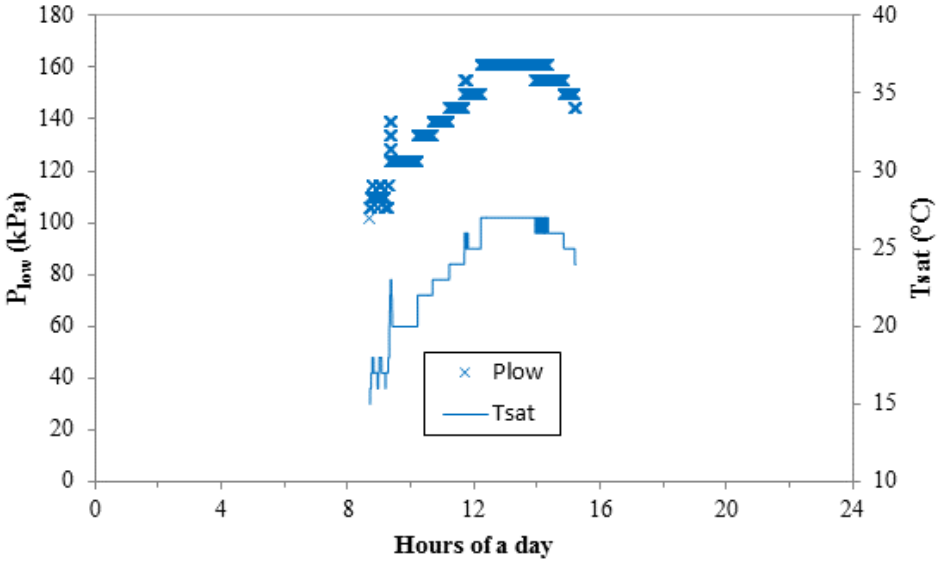

Evaporator pressure and saturation temperature variation for winter solstice